

UCLA

UCLA Electronic Theses and Dissertations

Title

Nanoparticles for therapeutic and diagnostic applications

Permalink

<https://escholarship.org/uc/item/5d2724fw>

Author

Chiu, Yin To

Publication Date

2014

Peer reviewed|Thesis/dissertation

UNIVERSITY OF CALIFORNIA

Los Angeles

Nanoparticles for therapeutic and diagnostic applications

A dissertation submitted in partial satisfaction of the

requirements for the degree of Doctor of Philosophy

in Bioengineering

by

Yin To Chiu

2014

ABSTRACT OF THE DISSERTATION

Nanoparticles for therapeutic and diagnostic applications

by

Yin To Chiu

Doctor of Philosophy in Bioengineering

University of California, Los Angeles, 2014

Professor Daniel T. Kamei, Chair

Nanomedicine focuses on the development and engineering of novel and unique therapeutic and diagnostic agents that can overcome the challenges associated with using traditional modalities. Nanoparticles (NPs) in the size range between 1 and 1000 nm have many advantages for use in these applications, such as, low polydispersity, established characterization methodologies, and the ability to be loaded with therapeutics for diseases, conjugated to targeting ligands to enhance specificity, and coated with polymers to improve stability and half-lives.

This thesis focused on developing nanotechnology to address *both* therapeutic and diagnostic applications due to the universal need to understand and maintain colloidal stability. Maintaining colloidal stability is crucial in therapeutic applications since aggregated NPs will have a reduction in the number of targeting ligands available for interacting with cell-surface receptors by reduction of the surface area to mass (or volume) ratio. The drug release from the NPs can also be significantly altered, and the aggregate sizes may no longer be appropriate for targeting tumors passively and for being actively internalized into cancer cells. The aggregation also has the possibility of severely reducing the shelf-life of the drug carriers. In the case of diagnostics, in addition to reducing the number of targeting ligands and shelf-life, aggregation can change the optical properties of NPs. Moreover, aggregated NPs in the well-established lateral-flow immunoassay (LFA) can experience difficulty flowing through the test strip and may give rise to invalid results. Accordingly, irrespective of the application, the studies in this thesis required an understanding and tuning of the electrostatic and steric, excluded-volume stabilizing interactions when designing the NPs.

With regard to cancer therapy, this thesis focused on further testing the limits of a transferrin (Tf) variant that was previously engineered by our laboratory for improving the delivery of cytotoxins in a Tf-cytotoxin molecular conjugate format. Specifically, our previously derived mathematical model was first extended to theoretically determine if conjugating a Tf variant to a NP would increase its association with a cancer cell, thereby increasing the probability of delivering a toxic payload to a cancer cell. Upon finding that the theoretical predictions supported such a construct, the Tf variant was conjugated to the NPs and then radiolabeled with iodine-125, and these NPs were found to associate with prostate cancer cells for a greater period of time relative to the native Tf counterpart, as predicted by our extended

mathematical model. Subsequently, poly(lactide-co-glycolide) (PLGA) NPs encapsulating the chemotherapeutic doxorubicin (DOX) was conjugated to a Tf variant and was shown to have improved drug carrier efficacy both *in vitro* and *in vivo* relative to the native Tf counterpart. The *in vivo* results were especially exciting as a single intravenous injection was found to dramatically inhibit tumor growth in a mouse model for prostate cancer. This work corresponded to the first ever investigation of the drug carrier properties of NPs conjugated to a Tf variant. In contrast to our laboratory's previous studies with molecular drug conjugates, which are very promising for cancers treated locally, these Tf variant-conjugated NPs administered intravenously have potential for treating most types of cancers.

With regard to diagnostic applications, this thesis focused on revolutionizing LFA. One of the most common applications of LFA is the pregnancy test, where gold NPs are used as the colorimetric indicator. The small sizes of the gold NPs also allow the use of low sample volumes, and their large surface area to mass ratio enables efficient capture of target molecules. Their optical properties can also be exploited to directly visualize a result. Although LFA has many features that make it attractive for use as a point-of-care diagnostic, the use of LFA for detecting biomarkers at low concentrations is severely limited due to its low sensitivity. To increase LFA sensitivity, our laboratory is the only one to have used aqueous two-phase complex fluid systems for concentrating biomarkers prior to their detection. This pioneering work is described in the thesis, where we began by using an aqueous two-phase Triton X-114 micellar system to pre-concentrate the model virus M13 prior to its detection with LFA.

This first combination of an aqueous two-phase system (ATPS) and LFA improved the detection limit of LFA for M13 by 10-fold, and has led to many new exciting avenues of

research. Subsequently, an aqueous two-phase polyethylene glycol (PEG)-salt system was investigated to concentrate the same virus but in a much shorter time period. The same PEG-salt system was then examined for its ability to concentrate the model protein Tf. In this case, due to Tf being significantly smaller than M13, gold NPs were used to bind and transport Tf into one of the two phases of the aqueous two-phase PEG-salt system. However, due to the high concentrations of salt present in one of the phases, the gold NPs were manipulated to ensure colloidal stability through the entire process from concentration to detection. These gold NPs were also manipulated to drive the gold NPs to the interface instead of one of the two bulk phases with the idea of further concentrating the target biomolecules, as the interface corresponds to a three-dimensional region that is only a few molecular diameters thick. Moreover, this thesis discusses the discovery of a very exciting phenomenon where the paper membranes used in LFA can enhance the phase separation process of an ATPS, which enables the concentration of the target molecules as they flow directly on the test strip. This ability to simultaneously concentrate and detect biomarkers directly on paper removes the need to extract a phase from a test tube and also reduces the time to result. Lastly, the combination of an ATPS and LFA was further extended to include magnetic fields and a new solid-liquid interface to enhance extraction. All of these technologies have the potential to dramatically improve the state of health care in resource-poor settings by providing rapid, accurate, and inexpensive diagnostics, leading to improved patient management, treatment, and outbreak prevention.

The dissertation of Yin To Chiu is approved.

Amander T. Clark

Richard Finn

Hsian-Rong Tseng

Lily Wu

Daniel T. Kamei, Committee Chair

University of California, Los Angeles

2014

This work is dedicated to my family, who always believes in me
and supports all my decisions.

TABLE OF CONTENTS

Chapter 1: Motivation and background	1
1.1 Nanoparticles for drug delivery applications	1
1.1.1 PLGA	4
1.1.1.1 Drug encapsulation and nanoparticle preparation	6
1.1.1.2 PLGA NP degradation and the drug release mechanism	7
1.1.1.3 Bioconjugation of PLGA NP.....	8
1.2 Nanoscale sensor system.....	9
1.2.1 Gold nanoparticles	10
1.2.1.1 Preparation and characterization of gold NPs	10
1.2.1.2 Surface plasmon resonance of gold NPs	11
1.2.1.3 Colloidal stability	12
1.2.1.4 Bioconjugation of gold nanoparticles.....	15
1.2.2 Lateral-flow immunoassay.....	15
1.2.2.1 LFA mechanism	18
Chapter 2: Improving the systemic drug delivery efficacy of nanoparticles using a transferrin variant for targeting	21
2.1 Motivation and background	21
2.2 Materials and Methods	24
2.2.1 Mathematical model of Tf-NP/TfR trafficking pathway	24
2.2.2 Cell culture.....	25
2.2.3 Conjugation of Tf to PNP	26
2.2.4 Iron loading of Tf and generation of oxalate Tf	26
2.2.5 Characterization of Tf-PNP samples	27
2.2.6 Radiolabeling Tf and Tf-PNP samples	27
2.2.7 Intracellular trafficking of Tf and Tf-PNP samples.....	28
2.2.8 Preparation of DP.....	29
2.2.9 Conjugation of PEG and Tf to DP	29
2.2.10 Characterization of DP and TPDP	31
2.2.11 In vitro cytotoxicity studies	32

2.2.12	Cytotoxicity studies in mouse PC3 xenograft models	32
2.2.13	Data analysis	33
2.3	Results	34
2.3.1	Mathematical model confirms that Tf iron release is still a governing factor for cellular association of Tf-NP	34
2.3.2	Characterization of Tf-PNP	36
2.3.3	Intracellular trafficking of Tf and Tf-PNP samples	38
2.3.4	Characterization of DP and TPDP	40
2.3.5	In vitro cytotoxicity of TPDPs	41
2.3.6	<i>In vivo</i> efficacy of TPDP delivered systemically to mice	42
2.4	Discussion	44
2.5	Conclusion.....	46

Chapter 3: Mathematical model for nanoparticles conjugated with a transferrin variant and *in vitro* studies with non-cancerous cells.....48

3.1	Mathematical model for Tf-NP cellular trafficking pathway.....	48
3.2	Estimation of the equilibrium dissociation constant of Tf-NP.....	56
3.3	<i>In vitro</i> cytotoxicity studies with a normal cell line.....	59

Chapter 4: Enhancing the lateral-flow immunoassay for viral detection using an aqueous two-phase micellar system.....61

4.1	Motivation and background	61
4.2	Materials and Methods.....	63
4.2.1	Culturing and Quantifying M13.....	63
4.2.2	Partitioning and Concentrating M13.....	64
4.2.3	Preparing Colloidal Gold Probes	64
4.2.4	Preparing LFA Test Strips	65
4.2.5	Performing LFA on M13	66
4.2.6	Combining ATPMS with LFA.....	67
4.3	Results and Discussion.....	67
4.3.1	Partitioning M13 in ATPMS.....	67

4.3.2	Concentrating M13 by Manipulating the Volume Ratio	70
4.3.3	Detecting M13 via LFA	72
4.3.4	Concentrating M13 Prior to LFA.....	72
4.4	Conclusions	74

Chapter 5: Using an aqueous two-phase polymer-salt system to rapidly concentrate viruses for improving the detection limit of the lateral-flow immunoassay76

5.1	Motivation and background	76
5.2	Materials and Methods	78
5.2.1	Culturing Bacteriophage M13.....	78
5.2.2	Finding Volume Ratios for the PEG-Salt System.....	79
5.2.3	Partitioning and Concentrating M13.....	80
5.2.4	Preparing Gold Nanoprobes.....	81
5.2.5	Combining ATPS with LFA	82
5.2.6	Analyzing LFA Quantitatively	82
5.3	Results and Discussion.....	83
5.3.1	Biomolecule Partitioning	83
5.3.2	Partitioning M13 in ATPS	87
5.3.3	Detecting M13 via LFA	89
5.3.4	Concentrating M13 prior to LFA	90
5.4	Conclusions	92

Chapter 6: Dextran-coated gold nanoprobe for the concentration and detection of protein biomarkers.....94

6.1	Motivation and background	94
6.2	Materials and Methods	97
6.2.1	Preparing Citrate-Capped Gold Nanoparticles	97
6.2.2	Preparing Polyethylene Glycol-Coated Gold Nanoparticles	98
6.2.3	Preparing Dextran-Coated Gold Nanoparticles	99
6.2.4	Determining the Critical Coagulation Concentration of Gold Nanoparticles.....	99

6.2.5	Preparing Polyethylene Glycol-Potassium Phosphate Aqueous Two-Phase Systems	100
6.2.6	Radiolabeling Anti-Tf Antibody.....	100
6.2.7	Preparation of Dextran-Coated Gold Nanoprobe.....	100
6.2.8	Partitioning Dextran-Coated Gold Nanoprobe.....	101
6.2.9	Preparing LFA Test Strips	102
6.2.10	Detecting Tf Using LFA	102
6.2.11	Combining Dextran-Coated Gold Nanoprobe, ATPS, and LFA to Detect Tf	103
6.2.12	LFA Quantification.....	103
6.3	Results	104
6.3.1	Determining the Critical Coagulation Concentration of Gold Nanoparticles.....	104
6.3.2	Partitioning Behavior of Dextran-Coated Nanoprobe.....	106
6.3.3	Pre-Equilibrium Extraction of Dextran-Coated Nanoprobe.....	107
6.3.4	Detecting Tf with LFA.....	109
6.3.5	Combining Dextran-Coated Gold Nanoprobe, ATPS, and LFA to Detect Tf	110
6.3.6	Quantifying LFA Test Line Intensities	111
6.4	Discussion	112
6.5	Conclusions	116

Chapter 7: A rapid and sensitive paper-based immunoassay for protein detection using interface extraction of an aqueous two-phase system.....118

7.1	Motivation and background	118
7.2	Materials and Methods	122
7.2.1	Radiolabeling the anti-Tf antibody	122
7.2.2	Preparing GNPs	123
7.2.3	Partitioning GNPs	123
7.2.4	Preparing the LFA test strip.....	124
7.2.5	Performing LFA with Tf but without pre-concentration	126
7.2.6	Combining the ATPS interface extraction with LFA for Tf.....	126
7.3	Results and discussions	127
7.4	Conclusions	133

Chapter 8: Simultaneous concentration and detection of biomarkers on paper135

8.1	Motivation and background	135
8.2	Materials and Methods	137
8.2.1	Determining the Polymer-Salt ATPS Solution Volume Ratios	137
8.2.2	Preparation of antibody-decorated dextran-coated gold nanoprobe (DGNPs) ...	137
8.2.3	Visualization of ATPS	138
8.2.5	Detection of Tf	139
8.2.5.1	LFA tests for detection of Tf	139
8.2.5.2	Detection of Tf with the 3-D paper well	140
8.3	Results and Discussion	141
8.3.1	Visualization of ATPS	141
8.3.2	Visualization of ATPS in Paper	143
8.3.3	Visualization of ATPS in the 3-D Paper Well Device	144
8.3.4	Detection of Tf using the 3-D Paper Well Device	145
8.4	Conclusion	149

Chapter 9: Other approaches to integrating the aqueous two-phase concentration system with the lateral-flow detection assay151

9.1	Overview	151
9.2	Motivation and background	151
9.2.1	Magnetic nanoparticles with ATPS and LFA	151
9.2.2	Solid-Liquid Interface Extraction	153
9.3	Materials and Methods	155
9.3.1	Preparing LFA test strips	155
9.3.2	Preparing GMPs	155
9.3.3	Developing the magnetic collection device	156
9.3.4	Partitioning GMPs in ATPS	156
9.3.5	Combining the GMPs, magnetic collection device, ATPS, and LFA	157
9.3.6	Preparing PGNPs	157
9.3.7	Combining the PGNPs, PP straw, ATPS, and LFA	158
9.4	Results and Discussion	158
9.4.1	Magnetic nanoparticles with ATPS and LFA	159

9.4.2	Solid-Liquid Interface Extraction	162
9.5	Conclusions	165
References	167

ACKNOWLEDGMENTS

The past 6 years of graduate school life was an amazing journey. I still remember the day when Dan gave me a lab tour and brought me to the student office. Immediately, I was surrounded by a friendly crowd of Kamei lab members. When Dan introduced me to the lab and mentioned, "Ricky already has some cool ideas about the Tf project...", I saw Foad look at me with a warm and courageous smile, and I immediately felt welcomed by the entire group. Shortly after that, I was preparing for the preliminary exams and the whole Kamei lab gathered and held practice sessions with me. That experience allowed me to get through the exams relatively easily. At the same time, I received a generous offer from a diagnostic company that wanted to hire me as a consultant. While very tempting, I quickly rejected the offer as I believed I had a much better opportunity working with Dan. That decision was one of the best decisions I have made thus far.

Dan and I decided to schedule my qualifying exam in summer 2009, which was only 5 months after I passed the preliminary exams. The qualifying exam is the defense of the proposal for the entire thesis, which normally is held in year 2 or 3, when the candidate has established a good understanding of the field and has collected a significant amount of data. That summer therefore became a very challenging yet exciting time for me. Victor spent many hours with me working with confocal microscopy and had patiently trained me with all the related techniques. Felix and I spent many late nights running cation-exchange columns, and we had fun having mini-competitions of seeding cells or predicting cell numbers when using the Coulter counter. Dennis trained me with the radiolabeling and trafficking experiments, and his focus and intensity

when performing his tasks has always inspired me. Byron helped me identify lung and breast cancers as potential cancers to be explored in my proposal; until my entry into the lab, the lab had focused primarily on gliomas. Byron also gave me the "Ricky Tan" nickname which still occasionally surfaces from time to time. My biggest thanks during that period, however, still goes to Dan, who spent endless hours with me discussing my potential experiments and projects. From him, I have learned that the journey is more important than the outcome; understanding the fundamental science and making the best educated decision is better than a trial and error approach; and presenting our work humbly can be more impactful than overselling the results. The oral exam went well, and we decided that the nanoparticle would be the focus of my thesis.

Tracy, Devin, and I worked on the Tf-PEI project. They both worked very hard in pushing the project forward, and we explored many techniques that were new to us at that time, such as dynamic light scattering, fluorescence microscopy, and FACS. I still remember Tracy's smile when she did something stupid and Devin's when he thought he said something funny. Gretchen and I worked on making spheroids using glioma cells, and we obtained some nice 3-D confocal images. She liked my joke that the "real" cause of her appendicitis was eating Foad's mysterious food that he brought back from his trip.

Takuma and I spent a whole year very closely working together on the Tf-nanoparticle project. We teamed up seamlessly when performing radiolabeling and trafficking experiments, and our results validated our hypothesis which led to many new projects. I still remember the night I introduced Takuma to blackjack in Vegas since he ended up not sleeping and coming back the next morning to the hotel room with a sad face and empty pockets.

Christina was a nice and curious girl; she asked me at least 100 questions a day during the summer of 2011. She identified the method to quantify gold nanoparticle concentration which is still currently used by the lab. Johnny and I spent endless hours performing cytotoxicity studies in the lab which may or may not have caused his arm RSI problems. He also helped pushed the SLIC project forward while I was busy preparing my thesis. Kristine, Bob and I worked together throughout the summer of 2011 to optimize our drug-loaded nanoparticle. We achieved the infamous "4D8P" which is the same formulation that we used for the subsequent *in vivo* studies. Kristine is my biggest supporter in the lab, and is also my mentee, and I am glad that she took my advice very seriously over these years. Her cheerleader personality has always lightened the spirits of those around her.

We had never performed *in vivo* experiments before the summer of 2012. Mike and I therefore spent a lot of time together to learn all the necessary techniques, purchase appropriate equipment, and establish protocols for the studies. We had a lot of fun helping each other in refining our skills, most of the time which involved me making fun of Mike and his poor mice. Without Mike, it would have not been possible to obtain good *in vivo* data in our first attempt.

Stephanie helped with deriving the new math model by extending the old one developed by Bert, who supported the lab by purchasing software for the lab and didn't even want Dan to know about it (I guess he knows now 😊). Stephanie and I have also spent a lot of time performing cytotoxicity studies which did not lead to any arm problems. Katie worked with me on extending our drug-loaded nanoparticle to mutant Tf. She can make delicious desserts, but too bad that she doesn't eat Korean barbeque.

My diagnostics project started when I teamed up with Foad to combine ATPS with LFA. It was a smooth collaboration since we both knew our individual technologies very well. This collaboration was so promising and productive that Foad and I founded Phase Diagnostics in Nov 2011, aiming to commercialize our technologies. There were numerous sleepless nights where we worked through grant applications and business plans. He always took my advice (but not my inappropriate jokes) seriously and his personality made working with him a pleasant experience. Alec, Parsa, and Cameron were all excellent both in lab and on the basketball court. A lot of kinks in our protocol were resolved by them which made my projects progress quickly.

I was Garrett's TA when he joined the program, and one day he approached me and asked about how the Kamei Lab was like, and I told him, "This is the best experience I ever had." And I am glad that he listened. He was very determined and detailed, and these are the attributes that I need from him in order for our startup to succeed.

Erik was one of the most reliable undergrad students whom I worked with. His tai-chi inspired membrane printing skill is unparalleled. Phuong and Alison has brought so much laughter to the lab; they are always happy and consistently ask me for more tasks with a smile. David is a humble and hard working guy who I felt comfortable passing along all the techniques and knowledge that I have gained to him; he would do great things in this lab if he keeps up his good work ethic.

It is apparent that we have treated everyone in the Kamei Lab as family members, and this "steady state" environment is created by Dan, whose caring, honesty, selflessness, attention to details, and thrive for perfection attributes have inspired everyone around him, and in turn, everyone in the lab maintains this equilibrium. I am very proud of being in the Kamei Lab and

after 6 years of basking in Dan's inspiration, I am ready to preach the "Kameism" to others as I move on.

I would also like to thank my parents, who always believe in me and completely support all my decisions. We have talked to each other every single day for the past 14 years since I left home. They told me to enjoy my graduate school life since this is the last time in my life that I can fully indulge in something I love without too much responsibility, and I followed that advice and took full advantage of it. I would like to thank my sister Jenny, who despite having very busy schedules, would help her brother out in a heartbeat. I also like to thank my uncle Anson, who took care of me when I first came to the US. He first talked me out of pursuing a music career, then gave me a C++ textbook. That boring book forced me to search my soul and find my true passion in bioengineering.

Lastly, I would like to thank the love of my life, Karen. For the past 12 years, we have been through bad times and good times. She understood my passion for research and has quietly supported and took care of me. I am not sure where our next destination will be, but I know she will be standing next to me as we pursue our dreams and live for a brighter future.

Chapter 1 is the overall motivation and background of my thesis.

Chapter 2 and 3 is a version of: R.Y.T. Chiu, T. Tsuji, S.J. Wang, J. Wang, C.T. Liu, and D.T. Kamei, "Improving the systemic drug delivery efficacy of nanoparticles using a transferrin variant for targeting," *J. Control. Release.* **180** (2014), 33-41, Copyright (2014), reprinted with permission from Elsevier. D.T. Kamei was the director of research for this article. This work was supported by the Department of Defense Prostate Cancer Research Program under award number W81XWH-09-1-0584 and Global COE of Micro-Nano Mechatronics of Nagoya University.

Chapter 4 is a version of: F. Mashayekhi, R.Y.T. Chiu, A.M. Le, F.C. Chao, B.M. Wu, and D.T. Kamei, "Enhancing the lateral-flow immunoassay for viral detection using an aqueous two-phase micellar system," *Anal. Bioanal. Chem.* **398** (2010), 2955-2961, Copyright (2010), reprinted with permission from Springer. D.T. Kamei was the director of research for this article. This work was supported by UCLA funds to D.T. Kamei.

Chapter 5 is a version of: E. Jue, C.D. Yamanishi, R.Y.T. Chiu, B.M. Wu, and D.T. Kamei, "Using an aqueous two-phase polymer-salt system to rapidly concentrate viruses for improving the detection limit of the lateral-flow immunoassay," *Biotechnol. Bioeng.*, that is currently in revision. D.T. Kamei was the director of research for this article. This work was supported by UCLA funds to D.T. Kamei.

Chapter 6 is a version of: R.Y.T. Chiu, P.T. Nguyen, J. Wang, E. Jue, B.M. Wu, and D.T. Kamei, "Dextran-coated gold nanoprobe for the concentration and detection of protein biomarkers," *Ann. Biomed. Eng.* D.T. Kamei was the director of research for this article. This work was supported by UCLA funds to D.T. Kamei. The final publication is available at www.springerlink.com.

Chapter 7 is a recently submitted version of: R.Y.T. Chiu, A.V. Thach, and D.T. Kamei, "A rapid and sensitive paper-based immunoassay for protein detection using interface extraction of an aqueous two-phase system" . D.T. Kamei was the director of research for this article. This work was supported by UCLA funds to D.T. Kamei.

Chapter 8 is a recently submitted version of: R.Y.T. Chiu, E. Jue, A.T. Yip, A.R. Berg, S.J. Wang, A.R. Kivnick, P.T. Nguyen, and D.T. Kamei, "Simultaneous concentration and

detection of biomarkers on paper". D.T. Kamei was the director of research for this article. This work was supported by UCLA funds to D.T. Kamei.

Lastly, chapter 9 is a combination of manuscripts currently in preparation for submission in the near future.

VITA

2005

B.S., Bioengineering
University of California,
San Diego, California

2009-2013

Teaching Assistant
Department of Bioengineering
University of California, Los Angeles

2014

M.S., Bioengineering
University of California,
Los Angeles, California

PUBLICATIONS

F. Mashayekhi, R.Y.T. Chiu, A.M. Le, F.C. Chao, B.M. Wu, and D.T. Kamei, "Enhancing the lateral-flow immunoassay for viral detection using an aqueous two-phase micellar system," *Anal. Bioanal. Chem.* **398** (2010), 2955-2961.

R.Y.T. Chiu, T. Tsuji, S.J. Wang, J. Wang, C.T. Liu, and D.T. Kamei, "Improving the systemic drug delivery efficacy of nanoparticles using a transferrin variant for targeting," *J. Control. Release.* **180** (2014), 33-41.

R.Y.T. Chiu, P.T. Nguyen, J. Wang, E. Jue, B.M. Wu, and D.T. Kamei, "Dextran-coated gold nanoprobe for the concentration and detection of protein biomarkers," *Ann. Biomed. Eng.* Accepted 2014.

Chapter 1: Motivation and background

As their name suggests, nanoparticles (NPs) range from 1 to several hundreds of nanometers in size. NPs have unique physical and chemical properties, such as large surface area to mass (or volume) ratio and extremely small size. This enables bioengineers to modify fundamental properties, such as solubility, immunogenicity, diffusivity, and hydrophilicity, to overcome limitations inherent in traditional therapeutic and diagnostic agents [1]. In the past decade, numerous NP-based therapeutic and diagnostic modalities have been developed for the treatment and detection of cancer, infectious diseases, and allergens [2, 3]. As therapeutic agents, these NPs enabled less invasive routes of administration, lower systemic toxicity, increased half-lives, and targeted delivery and controlled release of therapeutics. As diagnostics agents, NPs have given rise to detection on the molecular level, and they have also been shown to drastically improve the sensitivity and specificity of current gold standards in diagnostics [4]. The most common NP platforms today include polymeric NPs, liposomes, dendrimers, gold NPs, magnetic NPs, silicon oxide NPs, and quantum dots [5]. This thesis focused on the development of (i) polymeric NPs to enable and facilitate targeted delivery of therapeutic agents for the treatment of cancer and (ii) gold NPs to rapidly detect infectious diseases in resource poor settings at the point-of-care.

1.1 Nanoparticles for drug delivery applications

Cancer is the second leading cause of death in the United States, contributing to more than 23% of the total deaths per year. According to the National Cancer Institute, Americans have a 28.5% probability of developing cancer in their lifetime [6]. A report from the American

Society of Clinical Oncology published in March 2014 predicted that cancer will surpass heart disease and become the top leading cause of death in less than 16 years [7]. A major problem with current standard-of-care cancer treatments, such as chemotherapy and radiation therapy, is that they are nonspecific and often result in severe side effects. Hence, there is a need for better treatment modalities for cancer.

Nanoscale drug delivery vehicles, or nanocarriers, provide great potential to overcome the nonspecificity problem and have numerous additional benefits which will be discussed in this section. Cancer therapeutics can be dissolved in, entrapped within, encapsulated inside, or attached to nanocarriers and can be made using a variety of materials such as polymers [8-11], lipids [12-15], and metals [16, 17].

Compared to molecular therapeutics, the larger size of nanocarriers leads to their selective accumulation in tumor tissue via the enhanced permeability and retention (EPR) effect [18]. This phenomenon results from the leaky vasculature associated with cancer angiogenesis and the dysfunctional lymphatic drainage within the tumor region [19]. These defective tumor vessels allow for the extravasation of macromolecular anti-cancer agents up to 400 nm in diameter, which is otherwise prevented in normal vasculature [20]. Moreover, poor lymphatic drainage in tumors results in the nanocarriers accumulating in the tumor, thereby facilitating drug release within the vicinity of the cancer cells. NP therapeutics can therefore exploit the EPR effect to passively target neoplastic regions. Molecular drug conjugates, on the other hand, cannot passively discriminate tumor tissue from normal tissue since their small size is not as affected by the poor lymphatic drainage.

Besides taking advantage of the EPR effect, nanocarriers offer many other advantages and have been reviewed extensively [21]. Encapsulation inside a nanocarrier can protect the

drug from premature degradation and from prematurely interacting with the biological environment. The increased size of nanocarriers also allows them to carry a larger cytotoxic payload, and unlike molecular conjugates, the type and number of drug molecules inside the carriers do not affect the pharmacokinetic properties and biodistribution of the nanocarriers themselves. Several studies have also demonstrated the ability for these nanocarriers to bypass the multidrug resistance mechanisms of certain cancer cell lines. Furthermore, the release kinetics of drug molecules within nanocarriers can be tightly controlled to match the drug's mechanism of action.

Although nanocarriers can passively target tumor tissues through the EPR effect, their antitumor efficacy and selectivity within the neoplastic tissue can be further enhanced by the additional attachment of cell-specific targeting ligands. Therefore, instead of being restricted to nonspecific cellular uptake, which can be a rather inefficient process, these conjugated nanocarriers can also take advantage of the natural intracellular trafficking pathway of the targeting agent. Furthermore, because they are large enough to accommodate many copies of one targeting ligand as well as many copies of multiple targeting ligands, these nanocarriers also benefit from multivalency effects that increase the binding affinity of the nanocarrier towards its receptor. In fact, many studies have demonstrated that these active-targeting nanocarriers exhibit greater cellular uptake and enhanced potency compared to their non-targeted counterparts. For example, anti-HER2 immunoliposomes encapsulating doxorubicin resulted in greater therapeutic efficacy compared to non-targeted liposomes in HER-2 overexpressing breast cancer xenograft models [15]. Additionally, transferrin-conjugated NPs formed by cyclodextrin-containing polycations and siRNA resulted in a significant inhibition of tumor growth in a murine model of metastatic Ewing's sarcoma, while the removal of transferrin led to an inability to shrink the

tumors. All of these attributes have rendered targeted nanocarriers as a promising treatment modality for cancer. The first part of this thesis focused on the development of a cancer drug delivery system using a novel engineered transferrin molecule conjugated to a polymeric NP composed of poly(lactide-co-glycolide) (PLGA), a biodegradable polymer that has been studied extensively.

1.1.1 PLGA

PLGA is a copolymer of lactic acid and glycolic acid (or lactide and glycolide). It can undergo hydrolysis of its ester linkages in water to produce the biodegradable monomers, lactic and glycolic acid, which can be eliminated by normal metabolic pathways. The physical properties of PLGA are tunable for different applications by adjusting parameters such as the ratio of lactide to glycolide or the overall polymer molecular weight. PLGA is an FDA-approved biodegradable polymer for drug delivery because of its biodegradability, mechanical properties, and compatibility with drugs [22, 23]. It has been extensively studied for its use in drug delivery and diagnostic applications, as well as in clinical research for cardiovascular diseases, cancer, and vaccine and tissue engineering [24]. The following table summarizes PLGA-based drug delivery systems that have entered the market:

Table 1.1 Commercially available PLGA based drug delivery systems.

Drug	Company	Product name	Indication	Reference
Naltrexone	Cephalon	Vivitrol®	Alcohol dependence	[25, 26]
Bromocriptine	Novartis	Parlodel LA®	Parkinson disease	[27, 28]
Risperidone	Janssen	Risperdal ®	Schizophrenia	[29]

	Pharmaceuticals			
Minocycline hydrochloride	OraPharma	Arestin®	Peridental disease	[30]
Buserelin acetate	Mochida Pharmaceutical Co.	Suprecur MP	Endometriosis	[31]
Lanreotide acetate	Ispen	Somatuline® LA	Acromegaly	[32]
Triptorelin embonate	Ispen	Pamorelin®	Prostate cancer	[33]
Triptorelin pamoate	Pfizer	Telstar®	Prostate cancer	[34]
Triptorelin acetate	Ispen	Decapeptyl® SR	Prostate cancer	[35-37]
	Sidus	Decapeptyl® Retard		
	Techofarma	Decapeptyl®		
	Ferring Pharmaceuticals	Decapeptyl® Depot		
Leuprolide acetate	TAP Pharmaceuticals	Lupron Depot®	Prostate cancer	[38, 39]
	Takeda	Enantone®		
	Wyeth	Prostap SR		
Octreotide acetate	Novartis	Sandostatin LAR® Depot	Acromegaly	[40]
Human growth hormone	Genentech	Nutropin Depot®	Pediatric growth hormone deficiency	[41, 42]

Besides its use in the development of drug delivery systems, PLGA has also been used in a variety of tissue engineering applications, such as grafts and prosthetic devices [43]. There is a growing trend in the field of tissue engineering which uses degradable porous scaffolds encapsulating cells or growth factors to regenerate tissues [44]. This approach requires a scaffold that can provide temporary mechanical function while being able to promote mass transport. In these applications, it is critical that a scaffold can provide adequate mechanical support in the range of hard (10-1500 MPa) and soft tissues (0.4-350 MPa) [45]. Scaffolds using traditional techniques such as gas foaming or porogen leaching with materials such as polylactide could not

satisfy such design criteria, but incorporating PLGA in a three-dimensional printing process yielded a scaffold with a reasonable peak elastic modulus up to 450 MPa, capable of providing mechanical support for both hard and soft tissues [46].

1.1.1.1 Drug encapsulation and nanoparticle preparation

PLGA NPs can be prepared by emulsion-solvent evaporation or nanoprecipitation. Generally, in emulsion-solvent evaporation, PLGA polymers are dissolved in a water immiscible, volatile organic solvent, followed by emulsification in an aqueous solution containing an emulsifier or surfactant, such as polyvinyl alcohol (PVA). The mixture is then stirred to allow the evaporation of the organic solvent, leaving behind the solid particles. This method can be adjusted to produce particles of desirable size. Increasing the rate of stirring and reducing the organic to aqueous phase ratio ensures the formation of nanoscale particles [47]. This method is primarily used in the encapsulation of hydrophobic drugs, where the drugs can be initially dissolved in the volatile organic solvent. To encapsulate hydrophilic molecules and proteins, a modification of this procedure using multiple emulsion steps can be applied. In this procedure, the hydrophilic drug or protein is dissolved in an aqueous phase, followed by the addition of an organic phase containing dissolved PLGA with vigorous stirring to yield a water-in-oil emulsion. This emulsion is then added to another aqueous phase which again contains an emulsifier for further emulsification to form a double emulsion. The organic solvent is allowed to evaporate to form the solid particles [48]. The choice of solvents and the stirring rate are the dominate factors in determining the encapsulation efficiency and the particle size in this procedure.

Drug-loaded PLGA NPs can also be synthesized by nanoprecipitation. In this procedure, the polymer and drug are dissolved in acetone, and the resulting solution is added drop-wise to an aqueous solution containing surfactants. Acetone is then evaporated, leaving behind the polymeric NPs encapsulated with drug. In this method, the drop speed, organic to aqueous phase ratio, choice of surfactant, and the stirring speed are all factors that determine particle size. Recently, a new nanoprecipitation procedure has been developed, which doesn't use a volatile organic solvent, but instead utilizes dimethyl sulfoxide (DMSO) as the organic phase to dissolve PLGA and the drug. When this organic phase is added to the aqueous phase, instead of evaporating, DMSO leaves the organic droplet since it is miscible with water, which leads to the formation of the solid nanoparticle [49].

1.1.1.2 PLGA NP degradation and the drug release mechanism

To successfully release the encapsulated drug, it is essential to understand the degradation profile of PLGA NPs. As opposed to surface erosion, where the degradation begins at the nanoparticle surface, the degradation of a PLGA NP is generally through bulk degradation, where the rate of polymer degradation is slower than the rate at which water penetrates into the particle [50]. This leads to an autocatalyzing effect associated with water penetrating into the core of the NP to trigger hydrolysis throughout the entire particle. As the PLGA polymers break down into oligomers, the surface layer acts as a semi-permeable diffusion barrier for the entrapped oligomers, while allowing water to diffuse inward [51]. This leads to an increase of carboxylic groups inside the particle due to the increase in oligomers, which further accelerates the hydrolysis process. As a result, the rate of degradation is higher in the particle core than on its surface [52]. The oligomers eventually further break down into lactic and glycolic acid

monomers. Lactic acid is metabolized through the tricarboxylic acid (TCA) cycle and subsequently eliminated as carbon dioxide and water [53]. Glycolic acid is either excreted through the kidney or can also enter the TCA cycle and leave the body in a similar fashion as lactic acid.

The degradation rate of the PLGA polymer is mostly dependent on the composition of the polymer. Studies have shown that a higher ratio of glycolic acid to lactic acid in the PLGA polymer would lead to faster degradation since glycolic acid is more hydrophilic than lactic acid [54, 55]. The molecular weight of the PLGA polymer also affects the degradation rate with a higher molecular weight exhibiting a lower degradation rate [51]. It has also been suggested that enzymatic degradation may play a role *in vivo*; however, the results reported by different research groups have been conflicting [56, 57].

The release profile of encapsulated drug from NP is complicated and can vary depending on the drug type, but it generally follows a biphasic pattern [58, 59]. The first phase is an initial burst release of drug that usually occurs as the drug on the surface of the NPs comes in contact with the medium, and is released as a function of its solubility and the penetration of water into the particle matrix. The second phase is when drug gradually diffuses through the tortuous paths created by water penetrating inside the particle.

1.1.1.3 Bioconjugation of PLGA NP

The drug-loaded PLGA NPs are designed to target cancer cells by conjugating targeting ligands onto the surfaces. In addition, their stability and *in vivo* half-lives can be improved by conjugating polyethylene glycol (PEG) to the surfaces, a process referred to as PEGylation. While there are various methods to introduce targeting ligands and PEG onto PLGA NPs, the

most common method of bioconjugation is to utilize the carboxyl functional group of the PLGA monomer, which is abundant on the surface of a PLGA NP. These carboxyl functional groups can be activated by 1-ethyl-3-(3-dimethylaminopropyl)-carbodiimide (EDC) and N-hydroxysuccinimide (NHS) in an acidic environment. The activated functional groups are reactive to amines, and leads to the conjugation of proteins through the lysine residues on the protein surface and PEG through the use of amine-functionalized PEG molecules. Since the density of PLGA is about 1.25 g/L, free proteins and PEG molecules can be easily purified from the conjugated nanoparticles via centrifugation.

1.2 Nanoscale sensor system

While cancer is the major cause of death in the United States, infectious diseases is the leading cause of mortality and morbidity in the developing world [60]. While healthcare benefits and services are provided in developed countries that can help battle infectious diseases, they are often inadequate or even lacking in many developing countries [61]. For example, among the world population of more than 6 billion people, 3 billion lack basic sanitation, 2 billion do not have access to electricity, and more than 1 billion lack basic healthcare services and clean drinking water [62]. Hence, it is not surprising that more than 95% of deaths due to major infectious diseases occur in developing countries, and most of these deaths are due to improper diagnosis and treatment. Currently, all gold standard diagnostics for infectious diseases require electricity, lab-based equipment, and trained personnel. Therefore, a new effective and inexpensive point-of-care (POC) diagnostics that can be used in resource-poor settings is urgently needed. The World Health Organization developed a set of generic guidelines for the development of diagnostic devices that are suitable for the developing world, summarized as

ASSURED: Affordable, Sensitive, Specific, User-friendly, Rapid and robust, Equipment-free, and Deliverable [63]. The second part of my thesis therefore focused on the development of the next generation POC diagnostics for resource-poor settings using colloidal gold nanoparticles.

1.2.1 Gold nanoparticles

Gold NPs have been used in a wide range of diagnostic applications, including optical biosensing [64], detection of DNA [65], and cancer diagnostics [66]. These applications take advantage of the gold nanoparticles' unique optical and electronic properties to detect biomolecules at low concentrations. A gold nanoparticle solution is an intense red color due to the interaction of incident light with a collective oscillation of free electrons in the particles, a phenomenon known as localized surface plasmon resonance. Unlike fluorescent dyes, their optical properties are not altered by exposure to light, and diagnostic tests using gold can be directly visualized. This unusual optical property, combined with its low cost and ease of functionalization with proteins and other molecules, led to the widespread use of gold NPs in detection and diagnostics.

1.2.1.1 Preparation and characterization of gold NPs

There are a wide variety of methods to synthesize gold NPs. Most of them start by reducing the commercially available chloroauric acid (HAuCl_4). Citrate reduction of Au^{3+} to Au^0 in water was introduced by Hillier and coworkers in 1951 [67]. The procedure was further refined by Frens in 1973 [68] to produce NPs of controlled size by varying the ratio between the reducing agent and the chloroauric acid. The resulting NPs were stabilized by a loose shell of

citrate ions adsorbed on the particle surface. This method is still the most commonly used procedure to synthesize gold NPs or precursors to other gold NP-based materials.

The Brust-Schiffrin method for gold NP synthesis reported in 1994 [69] also had a significant impact because it allowed the synthesis of thermally stable gold NPs with very low polydispersity for particle diameters anywhere between 1.5 and 5.2 nm. These gold NPs can be repeatedly dissolved and recovered in common organic solvents without aggregation. This method still involves the reduction of Au^{3+} to Au^0 using sodium citrate, but instead of stabilizing with citrate ions, the NPs are stabilized by thiol ligands that strongly bind to the particle surface.

The most common characterization technique for gold NPs is high-resolution transmission electron microscopy (HR-TEM), which provides a precise image of the gold core [70]. Other methods, such as atomic force microscopy (AFM), small-angle X-ray scattering (SAXS) [71], and laser desorption-ionization mass spectrometry (LDI-MS) [72], can also quantify the sizes of gold NPs. In recent years, there have been efforts to simplify the quantification of the size and concentration of gold NPs using UV-visible spectra [73] and dynamic light scattering [74].

1.2.1.2 Surface plasmon resonance of gold NPs

As mentioned previously, the red color displayed by a gold NP solution is due to a phenomenon called surface plasmon resonance (SPR), or the collective oscillations of electrons at the surfaces of NPs that is correlated with the incident light. The nature of SPR was rationalized by Mie theory. According to this theory, an electromagnetic frequency can induce a resonant coherent oscillation of free electrons if the dimension of the particle is much smaller than the wavelength of light. In general, the surface plasmon band is around 520 nm, but it is very sensitive to the composition, size, shape, and environment, as well as the ligand shell that is

adsorbed on the NP surface. This sensitivity of the surface plasmon band has led to the development of sensitive sensors, which measure the shifting of the surface plasmon band as the gold surface interacts with samples.

1.2.1.3 Colloidal stability

The interactions that govern the colloidal stability of gold NPs play a significant role in diagnostics since the aggregation and dispersion of the NPs can affect their optical properties [75] and their ability to bind target molecules. The colloidal stability of gold NPs is often explained by the Derjaguin-Landau-Verwey-Overbeek (DLVO) theory [76, 77], where the interaction potential energy between two equal spheres ($\Phi_{DLVO}^{equal\ spheres}$) is equal to the sum of the interaction potential energies due to van der Waals ($\Phi_{vdW}^{equal\ spheres}$) and electrostatic ($\Phi_{elec}^{equal\ spheres}$) interactions.

$$\Phi_{DLVO}^{equal\ spheres} = \Phi_{vdW}^{equal\ spheres} + \Phi_{elec}^{equal\ spheres} \quad (1.1)$$

The van der Waals interaction energy includes the interactions between two permanent dipoles (the Keesom interaction), a permanent dipole and an induced dipole (the Debye interaction), and two induced dipoles (the London dispersion interaction). Using the Derjaguin approximation, the van der Waals interaction potential energy between two equal spheres is given by:

$$\Phi_{vdW}^{equal\ spheres} = -\frac{AR}{12D} \quad (1.2)$$

where A is the Hamaker constant, which is always positive and includes all the coefficients in the Keesom, Debye, and London interactions; R is the radius of the sphere, and D is the distance

of closest approach between the two spheres. Since R and D are always positive, the van der Waals potential is always negative.

In the DLVO theory, the electrostatic interaction potential energy between two equal spheres is given by:

$$\Phi_{elec}^{equal\ spheres} = 64\pi R k_B T n_{salt,bulk} \kappa^{-2} \Lambda_0^2 \exp\left(-\frac{d}{\kappa^{-1}}\right) \quad (1.3)$$

where $k_B T$ is the thermal energy, $n_{salt,bulk}$ is the concentration of salt in the bulk solution (*i.e.*, very far from the spheres where the potentials are no longer felt), κ is the inverse of the Debye-Hückel screening length, and Λ_0 is dependent on the thermal energy, the valence of the symmetrical salt ions, and the electrostatic potential of the colloid at its surface.

Figure 1.1 shows the van der Waals and electrostatic potentials separately, as well as their summation corresponding to the DLVO potential (green), as a function of the distance of closest approach between the particles.

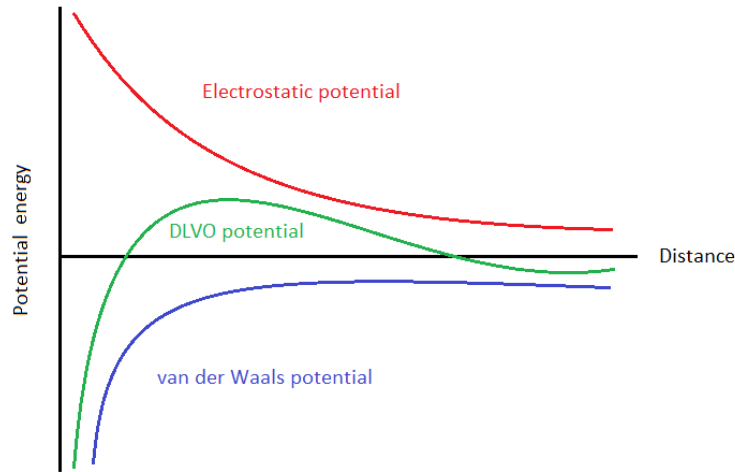


Figure 1.1. The van der Waals, electrostatic, and DLVO potential energies between two equal spheres.

Under normal conditions, gold NPs prepared using the Frens method are stable in water due to the negative surface charges on the NPs associated with the adsorbed citrate ions. However, these NPs can coagulate in an aqueous solution of high ionic strength when the concentration of salt exceeds the critical coagulation concentration (CCC) of the NPs. The CCC is the concentration of salt at which the particles lose stability and begin coagulating. This concentration can be derived using the DLVO theory and was found to be strongly dependent on the valence of the counterion. If gold NPs are placed in an aqueous solution with a high salt concentration, the positively charged cations are attracted near the negatively charged surfaces of the gold NPs. Due to this greater concentration of counterions, the net charge in the vicinity of the gold NP goes down, and by Gauss's Law, this decreases the electric field emanating from the gold NP. This screening effect weakens the electrostatic interactions between the NPs, and allows the van der Waals attractive interactions to dominate, causing the NPs to coagulate.

Since electrostatic repulsions cannot maintain colloidal stability of the gold NPs in a high salt environment, the NPs are coated with polymers to provide steric stabilization. When two polymer-coated NPs approach each other, they experience repulsive excluded-volume interactions, which are sometimes also explained by the unfavorable entropy associated with compressing the polymer chains [78, 79]. The interactions between the polymer-coated nanoparticles depend on the type of polymer, the length of the polymer, the coverage of polymer, and the nature of the solvent [80]. The most commonly used polymer for steric stabilization is PEG, which has been studied extensively and utilized in multiple applications [81-83].

1.2.1.4 Bioconjugation of gold nanoparticles

Gold NPs can be utilized as diagnostic agents by decorating their surfaces with ligands that can specifically bind to target biomolecules. The colloidal stability of the NPs can also be enhanced by PEGylation or conjugating with various stabilizing agents, such as bovine serum albumin (BSA). Most conjugation procedures to gold surfaces involve the formation of dative bonds. Dative bonds are different from normal covalent linkages, since they are formed from two electrons being donated from a single atom, instead of two atoms donating one electron each. The most common dative bond formed with gold surfaces is that formed with a thiol, where the lone pair of electrons on the sulfur atom can form a dative bond with a gold atom. Oxygen- and nitrogen-containing organic molecules can also form dative bonds with gold atoms. Proteins are thought to form dative bonds with gold NPs via their surface amines from the lysine residues, although the exact mechanism is still not well-understood. With regard to PEG, gold NPs can be PEGylated by utilizing thiolated PEG. Since gold NPs have a much higher density than water, unconjugated ligands and polymers can be purified from gold NPs via centrifugation.

1.2.2 Lateral-flow immunoassay

One application that was drastically improved with the use of gold NPs is the lateral-flow immunoassay (LFA), which now utilizes gold NPs as the colorimetric indicator. The most common form of LFA is a test strip which consists of 4 components: a sample pad where the sample is applied, a conjugate pad which contains the dry form of gold NPs that are conjugated with antibodies specific for the target analyte, a nitrocellulose membrane where the binding occurs and results can be interpreted, and the absorbance pad which acts as a sink for excess fluid (Fig. 1.2).

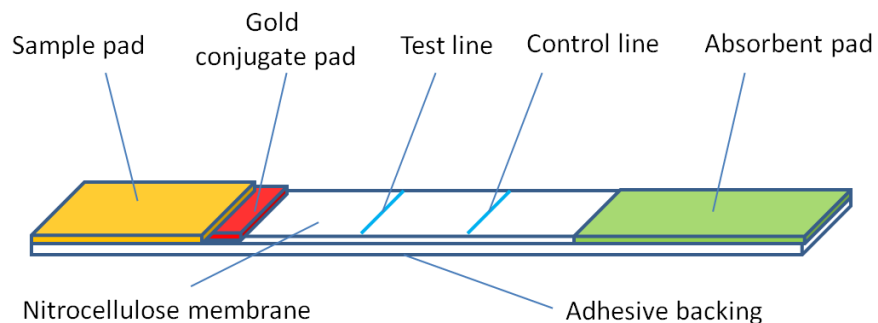


Fig. 1.2. Schematic representation of a typical LFA test strip and its components.

Prior to the use of gold NPs as the colorimetric indicator, latex microspheres encapsulated with dyes were used. However, these microspheres were more expensive and difficult to synthesize, and the larger sizes of these microspheres also had several limitations. Specifically, due to the smaller surface area to mass (or volume) ratio of these microspheres, the sensitivity of the assay was worse as fewer antibodies could be conjugated to the particle surface and thus fewer target molecules could bind to the particle. These larger microspheres also increased the assay time since they took a longer time to travel through the paper strip, and were also often trapped within the pores of the materials, leading to high background noise that also reduced the sensitivity of the assay.

The aforementioned limitations were addressed by incorporating gold NPs with LFA. The current LFA device is easy to develop and inexpensive to manufacture. The assay is also rapid and does not require any lab-based equipment or trained personnel to operate. Given its huge benefits and economic potential, it is surprising that very little research effort has been devoted to LFA, and the majority of these devices are still based on the design first reported in 1979 [84]. One major disadvantage of LFA is that its sensitivity is lower than lab-based assays, and it cannot be used when the target analyte is present only in low concentrations in samples of

interest. One of the most common applications for LFA is the pregnancy test since human chorionic gonadotropin (hCG) exists abundantly in the urine of pregnant women. On the other hand, LFA is not sensitive enough to replace lab-based assays, such as the enzyme-linked immunosorbent assay (ELISA), when diagnosing infectious diseases since the detection limits of ELISA for infectious pathogens are generally 10-100 fold less than commercially available LFA tests [85]. This explains why there are hundreds of LFA companies manufacturing pregnancy tests or tests for abused drugs, while only 2 USA companies currently develop LFA for a few infectious diseases (Table 1.2). In fact, there are also frequent reports that the actual sensitivities of these assays are lower than those claimed by the manufacturers [86, 87]. For example, OraSure's HIV LFA claimed to have a sensitivity greater than 99%, while recent studies have shown that the actual sensitivity of the assay can be as low as 86%, meaning 1 in every 6 tests would display a false negative result [88]. There is therefore an urgent need to develop sensitive LFA tests for many infectious diseases in resource-poor settings or at the point-of-need.

Table 1.2. Commercially available LFA tests for infectious diseases.

Company	Infectious disease	Biomarker	Medium	Sensitivity/ specificity
OraSure	AIDS	Anti-HIV-1/2 antibody	Whole blood, oral fluid	99.2%/99%
	Hepatitis C	Anti HCV antibody	Whole blood	98%/>99%
	Influenza A/B	Anti influenza A/B antibody	Nasal specimen	Influenza A: 97%/94.2% Influenza B: 94.3%/93.5%
Alere	Peptic ulcer disease	Anti- <i>Helicobacter pylori</i> antibody	Whole blood	93%/89.2%
	Mononucleosis	Anti mononucleosis heterophile antibody	Whole blood	98%/>99%
	Giardia	Giardia cyst antigen	Fecal	98.9%/100%

			specimen	
	Cryptosporidium	Cryptosporidium oocyst antigen	Fecal specimen	100%/99.8%
	AIDS	Anti HIV-1/2 antibody + p24 antigen	Whole blood	99.9%/99.8%
	Malaria	Histidine-rich protein II on <i>Plasmodium falciparum</i>	Whole blood	99.7%/94.2%
	<i>Legionella pneumophila</i>	<i>Legionella pneumophila</i> serogroup 1 antigen	Urine	95%/95%

1.2.2.1 LFA mechanism

There are two different approaches for the LFA: the sandwich assay and the competition assay. The sandwich assay is used when the target molecule is large, such as a viral particle, and may have multiple binding sites for its specific antibodies. The competition assay is used if the target molecule is a small molecule or a protein, which can only bind to one antibody.

In the sandwich assay (Fig. 1.3), antibodies specific for the target of interest are immobilized on a nitrocellulose membrane in the form of a line, called the test line. Secondary antibodies against the primary antibody are also immobilized on the nitrocellulose membrane in the form of a line, called the control line. In LFA, a sample first comes into contact with the gold nanoprobe (GNP), which is a gold nanoparticle decorated with specific antibodies. If the target molecules are present in the sample, they would first bind to GNPs. Subsequently, as these GNPs move up the LFA strip, the target molecules would be sandwiched between the specific antibodies immobilized on the test line and those on the GNPs. The presence of a visual band at the test line indicates a positive result. Alternatively, if the target molecule is not present in the solution, the GNPs would not bind to the immobilized antibodies at the test line. This

indicates a negative result. Furthermore, regardless of the presence of the target molecule in the sample, the GNPs would bind to the immobilized secondary antibodies at the control line, which indicates that the fluid had flowed completely throughout the strip and that the test is valid.

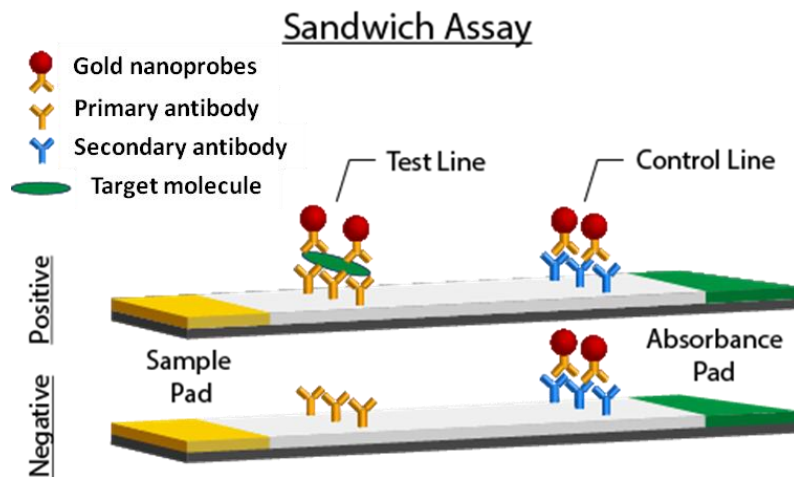


Figure 1.3. Schematic representation of the positive and negative results for the sandwich assay.

In the competition assay (Fig. 1.4), the target molecule or its fragment which contains the antibody recognition site is immobilized on the nitrocellulose membrane to form the test line. A secondary antibody is again immobilized downstream of the test line as the control line. When sample first comes in contact with the GNPs, if the target molecule is present, they will first bind and saturate the primary antibodies decorated on the gold nanoparticles. Subsequently, as these GNPs move up the LFA strip, they will not be able to bind to the test line since all the binding sites on the antibodies are occupied. The lack of the test line indicates a positive result. Alternatively, if the target molecule is not present in the solution, the GNPs would be able to bind to the test line. The visible test line indicates a negative result. Furthermore, regardless of

the presence of the target molecule in the sample, the GNPs would be able to bind the immobilized secondary antibodies on the control line, which indicates a valid test.

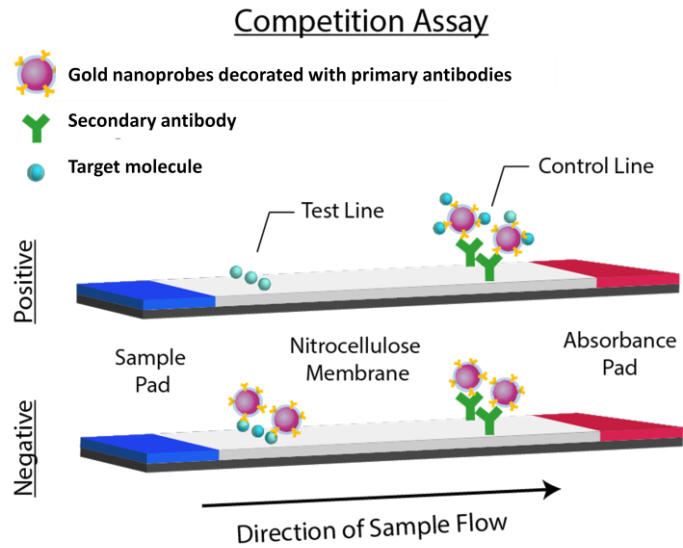


Figure 1.4. Schematic representation of the positive and negative results for the competition assay.

Chapter 2: Improving the systemic drug delivery efficacy of nanoparticles using a transferrin variant for targeting

2.1 Motivation and background

Since current standard chemotherapy often leads to severe side effects, recent efforts have focused on cancer therapeutics demonstrating specificity towards the tumor and reduced toxicity to normal tissues. Tf has been used as a cancer-targeting agent in multiple delivery systems since the transferrin receptor (TfR) is overexpressed in many types of cancer cells. The investigation of CALAA-01, a Tf-conjugated cyclodextrin polymer-based nanoparticle, achieved the first targeted delivery of siRNA in a Phase I clinical trial in May 2008 [89, 90]. Additionally, MBP-426, a Tf-bound liposome containing the cytotoxic platinum-based drug oxaliplatin, has proved promising, as it has completed Phase I clinical trials for solid tumors and is currently being evaluated in Phase II studies [91]. These nanocarriers, some of which are NPs, exploit the enhanced permeability and retention (EPR) effect to passively target tumors when administered systemically [18, 92, 93]. Once these NPs have accumulated inside the tumor, they can actively target cancer cells via the Tf decorated on their surfaces. Due to the overexpression of TfR, the Tf-conjugated NPs (Tf-NPs) can specifically internalize into cancer cells and deliver their drug payloads.

Although the conjugation of native Tf improves tumor-specific cellular uptake, significant limitations in Tf's efficacy as a drug carrier still exist since an iron-bound Tf molecule (holo-Tf) is restricted to a single 5 to 10 minute passage through a cell [94, 95]. Once holo-Tf binds TfR, becomes internalized via receptor-mediated endocytosis, and releases iron,

iron-free Tf (apo-Tf) is then recycled to the cell surface, where it quickly dissociates from TfR. Since rebinding of iron by Tf is an inefficient process, recycled Tf is often assumed to not be able to rebind iron and, therefore, TfR, thus limiting the amount of payload delivered by the NP.

In order to increase the probability of delivering therapeutics to TfR-overexpressing cancer cells, we wanted to increase the time Tf remained within a cell, *i.e.*, increase its cellular association. Using a mathematical model that we developed for the Tf/TfR cellular trafficking pathway (8), we discovered that inhibiting the iron release from Tf in the endosome could increase the cellular association of Tf. To verify this prediction, we previously generated a variant of Tf by replacing the synergistic carbonate anion of Tf with oxalate, since oxalate can stabilize the iron atoms in Tf and therefore decrease Tf's iron release rate in the endosome [96]. Intracellular trafficking experiments with various cancer cell lines demonstrated that oxalate Tf exhibited an increased cellular association compared to native Tf, which led to enhanced delivery of a conjugated drug, diphtheria toxin [97]. Subsequently, site-directed mutagenesis was utilized to engineer Tf mutants that exhibited even slower iron release rates. Accordingly, conjugates of these Tf mutants with diphtheria toxin possessed even greater potency in *in vitro* cytotoxicity experiments with ovarian cancer [98] and glioblastoma cell lines. Moreover, intratumoral injections into xenografted glioma tumors in a mouse model resulted in near-complete tumor regression within 8 days [99].

Based on the greater cellular association and efficacy of our molecular oxalate and mutant Tf-drug conjugates, the work presented in this chapter is a natural extension of our previous research with Tf variant systems and corresponds to the first investigation of the drug carrier properties of NPs conjugated to a Tf variant. In contrast to our laboratory's molecular drug conjugates, which are very promising for cancers treated locally, oxalate Tf-NPs

administered intravenously may prove to be more suitable for most types of cancers, as they can avoid the competitive inhibition associated with endogenous Tf present at higher concentrations in the blood serum (3-6 μM) (8). More importantly, our novel oxalate Tf-NPs and Tf variant-drug conjugates are similar in that both may bypass native Tf's rapid recycling (Fig. 2.1). Specifically, we hypothesized that oxalate Tf-NPs would be able to significantly improve upon the status quo.

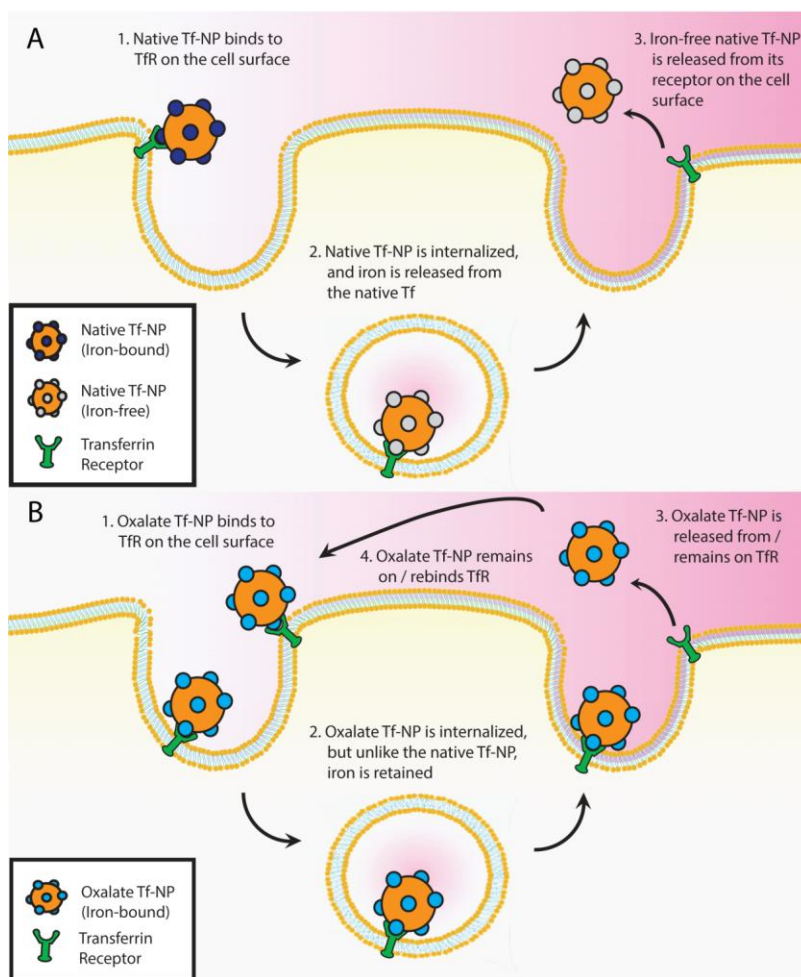


Figure 2.1. Schematic of the native and oxalate Tf-NP/TfR trafficking pathways. (A) Iron-bound native Tf-NP binds TfR, is internalized, and releases iron once it enters the acidic environment (pH ~5.6) of the endosome. Iron-free Tf-NP is then recycled to the cell surface, where it quickly dissociates and is assumed to be lost, due to the inefficiency with which Tf-NP rebinds iron. (B) Oxalate Tf-NP is internalized, but exhibits inhibited iron release in the acidified endosomal compartment. Iron-bound Tf-NP, instead of iron-free Tf-NP, returns to the cell surface. Since iron-bound Tf-NP retains its high

affinity for TfR at the cell surface, it exhibits a slow dissociation rate. As a result, iron-bound Tf-NP can either remain bound to TfR and re-enter the cellular trafficking pathway or, if dissociation occurs, quickly rebind another TfR for internalization. Accordingly, cellular association is increased by increasing the number of cycles, not by lengthening the residence time of one cycle. For simplicity, only monovalent Tf-TfR binding is depicted in this figure, but multiple Tf on a Tf-NP can exhibit multivalency effects and bind to multiple TfR on the cell surface.

To test our hypothesis, we performed a number of theoretical and experimental studies. An extension of our previous mathematical model predicted an increased cellular association for oxalate Tf-NPs, and this prediction was experimentally verified via cellular trafficking studies with radiolabeled Tf-conjugated polystyrene NPs (Tf-PNPs). To see if this improvement could be translated into increased potency with drug-loaded NPs, doxorubicin (DOX)-loaded poly(lactide-co-glycolide) (PLGA) nanoparticles (DP) were prepared and then conjugated with polyethylene glycol (PEG) and Tf to form Tf-PEG-DPs (TPDPs). The variant TPDP demonstrated increased potency over the native Tf-system in *in vitro* cytotoxicity assays. Finally, through *in vivo* experiments with a mouse model, we showed that using a single, intravenous injection of variant TPDPs led to a much greater inhibition of tumor growth compared with native TPDPs and the phosphate-buffered saline (PBS) control.

2.2 Materials and Methods

2.2.1 Mathematical model of Tf-NP/TfR trafficking pathway

We extended the Tf/TfR trafficking model previously developed by our laboratory [97]. This extended model, which was derived using the principles of mass action kinetics, describes the trafficking behavior of Tf-NP, including its binding to cell-surface receptors, internalization, partitioning in the endosomal compartment, recycling, and degradation. To transition from describing the trafficking behavior of molecular ligands to that of nanoparticles, two main

parameters from the previous model were altered, namely, the equilibrium dissociation constant (K_D) of Tf-NP binding to TfR and the partitioning of the drug carrier in the endosomal compartment.

The system of ordinary differential equations was solved using the modeling software Berkeley Madonna. The length of the model simulations was set to 2 h with initial conditions set to zero for all species except the concentration of holo Tf-NP in the media (0.75 pM) and the number of TfR on the cell surface. The area under the curve (AUC) of internalized Tf-NPs versus time was calculated and used as the metric to quantify the cellular association of Tf-NPs. This was the same metric as the one used in our previous mathematical model [97].

2.2.2 Cell culture

PC3 human prostate cancer cells were a kind gift from Dr. Lily Wu (University of California at Los Angeles Pharmacology, Los Angeles, CA). A549 human non-small cell lung cancer cells were purchased from the American Type Culture Collection (ATCC, Manassas, VA). Both cells were seeded onto 75 cm² tissue culture flasks (Corning Incorporated, Corning, NY) and grown in RPMI 1640 (for PC3 cells, Invitrogen, Carlsbad, CA) or F12K (for A549 cells, Invitrogen) supplemented with 10% fetal bovine serum (Hyclone, Logan, UT) and 1% penicillin/streptomycin (Invitrogen) at a pH of 7.4. The cells were incubated in a humidified atmosphere with 5% CO₂ at 37°C. All cell lines used in this study were authenticated by Laragen, Inc. (Culver City, CA) using the Promega StemElite (Promega) for STR analysis. Results indicated that the cell lines used in this study are authentic. All reagents and materials were purchased from Sigma-Aldrich (St. Louis, MO) unless otherwise specified.

2.2.3 Conjugation of Tf to PNP

PNP (100 nm diameter) were purchased from Phosphorex, Inc. (Fall River, MA) with free surface amines and encapsulated with a proprietary hydrophobic dye. Apo-transferrin (apo-Tf) was purchased from Sigma-Aldrich (St. Louis, MO). The molecules 2-iminothiolane (IT; Pierce, Rockford, IL) and N-succinimidyl 3-[2-pyridyldithio]-propionate (SPDP; Pierce) were used as crosslinkers for conjugating Tf to PNP. To thiolate Tf, 1 mg of Tf was dissolved in 100 mM borate buffer (pH 8.0). IT was then added to the Tf solution to yield a 5:1 molar ratio between IT and Tf. The mixture was then incubated for 60 min at room temperature. Free IT was removed by centrifugation through Zeba desalt spin columns (Pierce) in phosphate buffer (pH 7.4). Subsequently, 0.85 mg of PNP was mixed with 1 mL of ddH₂O to form a PNP solution. Excess SPDP (5000:1 SPDP:PNP molar ratio) was then added to the PNP solution, and the mixture was incubated for 60 min at room temperature. Free SPDP was removed by overnight dialysis (MWCO: 100,000 Da) in ddH₂O at room temperature. Subsequently, the thiolated Tf and SPDP modified PNP were mixed in a 5000:1 Tf:PNP molar ratio and incubated for 20 h at 4°C. The free Tf molecules were removed by 48 h dialysis (MWCO: 100,000 Da) in phosphate buffer at room temperature. The undesirable highly crosslinked NPs were removed by centrifugation at 9000 rpm for 10 min. The supernatant was collected and stored at 4°C for characterization.

2.2.4 Iron loading of Tf and generation of oxalate Tf

Prior to all experiments, all Tf and Tf conjugated NP samples were iron loaded. Briefly, 20 µL of 250 mM of the iron chelating agent nitrilotriacetate (NTA) was mixed with 10 µL of 250 mM iron (III) chloride. To generate native Tf samples, the mixture of NTA and iron (III)

chloride was mixed with 20 mM 4-(2-hydroxyethyl)-1-piperazineethanesulfonic acid (HEPES buffer) containing 20 mM bicarbonate. To generate oxalate Tf samples, the mixture of NTA and iron (III) chloride was instead mixed with 20 mM HEPES buffer containing 20 mM oxalate. This iron mixture with bicarbonate or oxalate was subsequently added to Tf samples in a 10:1 Fe:Tf molar ratio and incubated at room temperature for 2 h to ensure all Tf were iron loaded. Excess free iron from iron-loaded samples was removed by Zeba desalt spin columns for the Tf molecule, dialysis for the Tf-PNP, and centrifugation for the TPDP.

2.2.5 Characterization of Tf-PNP samples

The size and zeta potential of the Tf-PNP samples were quantified using a Malvern Zetasizer Nano ZS model Zen 3600 (Malvern Instruments Inc, Westborough, MA). The concentration of Tf on Tf-PNP was quantified by the bicinchoninic acid (BCA) assay, while the PNP concentration was determined by measuring the fluorescence of the hydrophobic dye that was encapsulated in PNP and using a standard curve that was previously constructed with known concentrations of PNP.

2.2.6 Radiolabeling Tf and Tf-PNP samples

Tyrosine residues of Tf and Tf-PNP samples were radiolabeled with Na¹²⁵I using IODO-BEADS (Pierce). Radiolabeled Tf samples were purified from free iodine-125 with a Sephadex G10 size exclusion column with bovine serum albumin (BSA) added to prevent nonspecific binding to the column. Radiolabeled Tf-PNP samples were purified with the same procedure, except that a Sephadex G50 size exclusion column was used instead of a G10 column. The

phosphotungstic acid (PTA) assay was used to quantify the specific activity and concentration of each radiolabeled sample [100].

2.2.7 Intracellular trafficking of Tf and Tf-PNP samples

Both PC3 prostate cancer and A549 lung cancer cells were seeded onto 35 mm dishes (Becton Dickinson and Company, Franklin Lakes, NJ) with a seeding density of 3×10^4 cells/cm² in growth medium. After 15 h of incubation in a humidified 5% CO₂ and 37°C environment, the growth medium was aspirated, and new incubation medium with 1 nM radiolabeled Tf or 0.75 pM radiolabeled Tf-PNP was added to each dish. The incubation medium was RPMI 1640 (for PC3 cells) or F12K (for A549 cells) supplemented with 20 mM HEPES and 1% penicillin/streptomycin (pH 7.4). The cells were incubated in this medium at 37°C for 5, 15, 30, 60, 90, and 120 min. At each time point, the incubation medium was removed, and the cells were washed 5 times with ice-cold WHIPS (20 mM HEPES, 1 mg/mL polyvinylpyrrolidone (PVP), 130 mM NaCl, 5 mM KCl, 0.5 mM MgCl₂, and 1 mM CaCl₂, pH 7.4) to remove nonspecifically bound Tf or Tf-PNP on cell surfaces. Cell-surface bound Tf or Tf-PNP was then separated from internalized Tf or Tf-PNP by adding 1 mL of ice-cold acid strip (50 mM glycine-HCl, 100 mM NaCl, 1 mg/mL PVP, and 2 M urea, pH 3.0) to each dish. The cells were placed on ice for 12 min. Each dish was then washed once more with 1 mL of acid strip. Lastly, the cells were solubilized by adding 1 mL of a 1 N NaOH solution to each dish for 30 min, followed by another 1 mL NaOH wash. The two NaOH washes were collected, and the radioactivity in the solution was quantified using a Cobra Series Auto-Gamma Counter (Packard Instrument Co., Meriden, CT) to determine the amount of internalized ligand or NP. Each entire

experiment was performed three times, where triplicate measurements were obtained for each time point in each experiment.

2.2.8 Preparation of DP

Poly(D,L-lactide-co-glycolide) (PLGA, 50:50, MW 7,000-17,000, acid terminated), D-alpha-tocopherol polyethylene glycol 1000 succinate (TPGS), and doxorubicin hydrochloride (DOX) were purchased from Sigma-Aldrich. DP was prepared by modifying the nanoprecipitation method described by Mu and Feng [101]. Briefly, 100 mg of PLGA and 2 mg of DOX were dissolved in 2.5 mL of dimethyl sulfoxide (DMSO). The polymer solution was then added dropwise to an aqueous phase (10 mL ddH₂O containing 0.02% TPGS surfactant) with mixing using a magnetic stir bar. The NP dispersion was stirred overnight. Subsequently, the dispersion was filtered through a 0.22 µm pore-size membrane (Millipore, Bedford, MA). The NPs were then washed with ddH₂O three times by centrifugation at 9000 rpm for 30 min at 20°C. The washed DP was stored at 4°C.

2.2.9 Conjugation of PEG and Tf to DP

The 1-ethyl-3-(3-dimethylaminopropyl)-carbodiimide (EDC) molecule and N-hydroxysuccinimide (NHS) were used to activate surface carboxyl groups on DP. In brief, 3 mg of DP was suspended in 0.2 mL of 2-(N-morpholino) ethanesulfonic acid (MES) buffer (100 mM, pH 5.5). To activate the carboxyl groups on the DP, 3.2 µL of NHS (1mg/mL) and 4.5 µL of EDC (1mg/mL) were mixed with the above DP suspension for 15 min. The reaction was quenched by raising the suspension pH to 7.4 by adding 10x phosphate buffer. To PEGylate DP,

heterobifunctional PEG maleimide-PEG₁₀₀₀₀-NH₂ (Nanocs Inc., New York, NY) with a 5000:1 PEG:DP molar ratio was added to the activated DP suspension. The solution was then allowed to react for 2 h at room temperature to allow the amine groups on heterobifunctional PEG to form a permanent link with the activated DP. Free EDC/NHS and PEG were removed by centrifugation at 9000 rpm. To couple Tf to PEGylated DP, Tf was first thiolated with IT as described previously. Free IT was removed by centrifugation through Zeba desalting columns in phosphate buffer. The thiolated Tf (5000:1 Tf:DP molar ratio) was subsequently added to the PEGylated DP, enabling the thiolated Tf to form a permanent linkage with the maleimide group on the PEGylated DP. After overnight incubation at room temperature, free Tf molecules were removed by centrifugation. The TPDP was collected and stored with 50 mM HEPES at 4°C. An overview of the nanoprecipitation and conjugation procedures for TPDP is shown in Fig. 2.2.

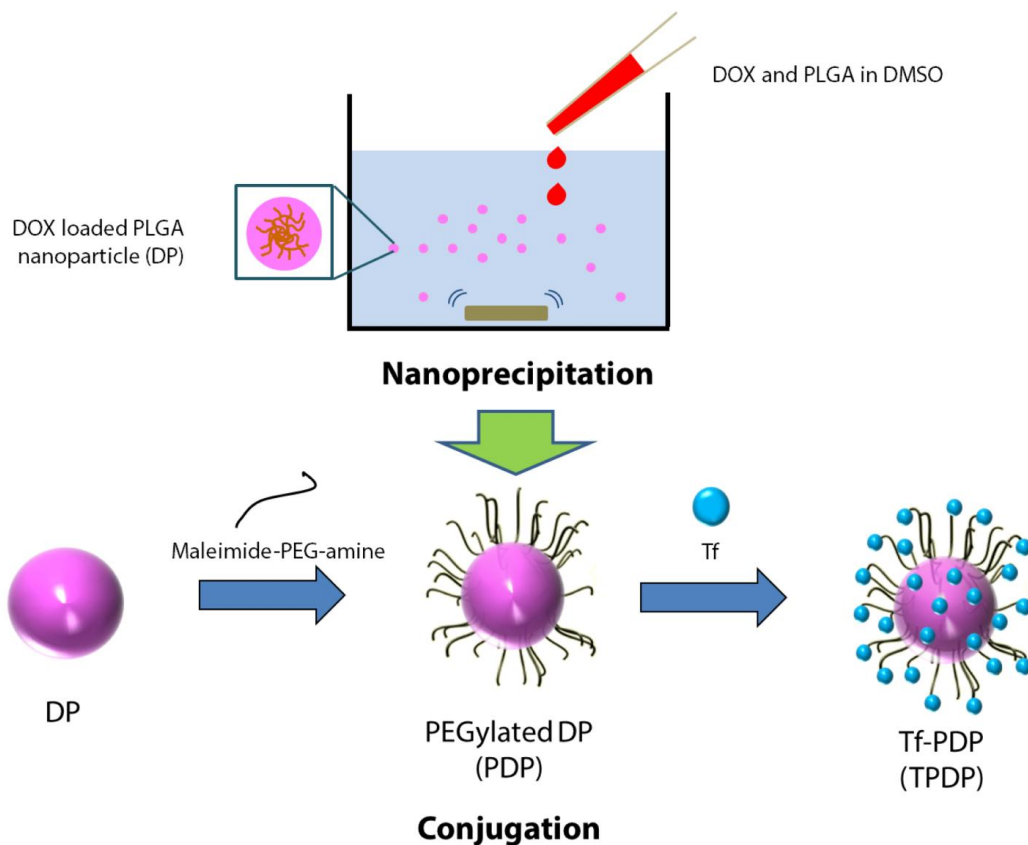


Figure 2.2. Schematic representation for the preparation of DP and conjugation of PEG and Tf to DP.

2.2.10 Characterization of DP and TPDP

The sizes and zeta potentials of DP and TPDP were quantified by dynamic light scattering (DLS) and zeta potential measurements, respectively. The mass of DP was measured after freeze drying. The amount of DOX loaded in DP was quantified by first dissolving the freeze dried DP samples in DMSO. The concentration of DOX in this solution was then determined by measuring its visible absorbance at 490 nm relative to background at 700 nm. The measured absorbance was correlated to the concentration of DOX using a standard curve that was previously constructed with solutions containing known DOX concentrations. The DOX loading ratio was determined with the following equation:

$$\text{Loading ratio (\%)} = \frac{\text{mass of DOX in DP}}{\text{mass of PLGA in DP}} * 100$$

The concentration of Tf on TPDP was quantified by the BCA assay, allowing the number of Tf molecules conjugated to each NP to be estimated.

2.2.11 In vitro cytotoxicity studies

The CellTiter 96 aqueous nonradioactive cell proliferation MTS assay (Promega Corp., Madison, WI) was used to determine cell viability. PC3 and A549 cells were seeded onto each well of a 96-well tissue culture plate with seeding densities of 2.5×10^4 cells/cm². Native or oxalate TPDP was prepared in growth medium, and their concentrations were varied from 0.01 μ M to 10 μ M. After aspirating the original medium from each well, 100 μ L of the prepared medium containing TPDP was added to each well and incubated for 72 h in a humidified environment (37°C, 5.0% CO₂). Subsequently, 20 μ L of the MTS reagent were added to each well, and the plate was incubated for an additional 1 h. Cell viability relative to control wells (cells incubated in media without TPDP) was quantified by reading the visible light absorbance values at 490 nm and 700 nm with an Infinite F200 plate reader (Tecan System Inc., San Jose, CA). Each entire experiment was performed three times, where triplicate measurements were obtained for each concentration of TPDP in each experiment.

2.2.12 Cytotoxicity studies in mouse PC3 xenograft models

All mouse experiments were performed in accordance with the Animal Research Committee at the University of California, Los Angeles. Solid PC3 flank tumors were

established in 4- to 6-week-old nu/nu male mice (Charles River Laboratories International, Inc., Wilmington, MA) by s.c. injection of 6×10^6 cells accompanied with basement membrane matrix Matrigel (BD Biosciences, San Jose, CA). Mice were constantly monitored and had free access to food and water. Tumor volumes were calculated using the formula of $0.5 \times (\text{length} \times \text{width}^2)$ by measuring the tumor dimensions every other day. Once tumors reached volumes of $300 - 350 \text{ mm}^3$, the tumor-bearing mice were randomly assigned into one of the 3 treatment groups (PBS control, native TPDP, and oxalate TPDP). For systemic therapeutic treatment of tumors, each mouse received either a 200 μL tail vein injection of PBS containing no drug (PBS control) or 200 μL of either native or oxalate TPDP with dose per weight of 8 mg DOX/kg. Each treatment group consisted of 5 mice. Only 1 injection was given, and the tumor volumes were monitored for a period of 4 weeks or until the tumor reached 15 mm in diameter, after which the tumor-bearing mice were sacrificed.

2.2.13 Data analysis

GraphPad Prism (GraphPad Software Inc, La Jolla, CA) and Stata 13 (StataCorp LP, College Station, TX) were used to analyze the data. For the *in vitro* intracellular trafficking studies, the Student's *t*-test was used to examine whether the difference in AUC value between native and oxalate Tf and the difference in AUC value between native and oxalate Tf-PNP were statistically significant ($P < 0.05$). For the *in vitro* cytotoxicity studies, the IC_{50} value, or the DOX concentration at which 50% inhibition of cellular growth occurs, was used as a metric for measuring the potency of TPDP. The Student's *t*-test was used to examine whether the difference in IC_{50} value between native and oxalate TPDP was statistically significant ($P < 0.05$).

For the *in vivo* efficacy study, a repeated measures mixed model analysis was used to determine whether there was a statistically significant difference in tumor volume among the three treatment groups (PBS control, native TPDP, and oxalate TPDP) or over time. Subsequently, tests of simple main effects were performed to evaluate if and when the difference in tumor volume between the treatments using native and oxalate TPDP was statistically significant ($P < 0.05$).

2.3 Results

2.3.1 Mathematical model confirms that Tf iron release is still a governing factor for cellular association of Tf-NP

To test our hypothesis that the Tf variant also improves the cellular association when conjugated to NP, we modified our previous model in order to more accurately represent the Tf-NP trafficking pathway. Specifically, we adjusted the equilibrium dissociation constant (K_D) of Tf-NP with TfR at the cell surface and inside the endosomal compartment, as well as the partitioning of the NPs in the endosomal compartment (κ).

Multiple studies have reported that the K_D of a ligand-conjugated NP for its receptor is smaller than that of the corresponding monovalent ligand itself [102, 103]. Specific calculations demonstrating this relationship are shown in the Chapter 3. Since the equilibrium dissociation constant is not a parameter in our model, we needed to implement this decrease in K_D by altering k_f and k_r , the association and dissociation rate constants between Tf-NP and TfR, respectively. Given the relationship $K_D = \frac{k_r}{k_f}$, the decrease in K_D for Tf-NP can be implemented by either increasing k_f , decreasing k_r , or performing a combination of both. Previously, Shaw and

colleagues demonstrated that the k_f of a nanoparticle conjugated with many ligands had no consistent trend in relation to the k_f of a free ligand. On the other hand, the k_r of this same nanoparticle was always smaller than that of the corresponding free ligand [104]. Therefore, we decided to capture multivalency effects within K_D by decreasing k_r by 1000-fold (see Chapter 3).

Once a Tf-NP binds with the above-mentioned higher affinity, it is endocytosed and brought to the endosome, where it may either partition into endosomal tubules and recycle back to the cell surface or remain inside the endosomal vesicle and eventually undergo degradation. The amount of internalized ligands and associated carriers that may be found in the tubule versus the vesicle at any given time is reflected in κ , or the vesicle/tubule partition coefficient. Defined as the concentration of the ligand or NP in the tubule divided by that in the vesicle, this partition coefficient accounts for excluded-volume interactions between the ligand or NP and the tubules and is a function of the size of the drug carrier divided by that of the tubules [105]. Accordingly, in comparison to free Tf, Tf-NPs have a larger diameter and therefore a smaller value of κ . Because tubule sizes were found to vary widely amongst the measurements of different laboratories [106, 107], κ of Tf-NP could not be fixed at an exact value. Therefore, based on the previously determined molecular Tf κ value of 0.81 [97], we varied κ from 0.001-0.1 for Tf-NP.

Simulations with the k_r value being 1000 times less than that of a single Tf molecule and with various values of κ were generated, and an example of some representative plots are shown in Fig. 2.3. Regardless of how κ was varied, all predicted responses exhibited the same trend and demonstrated that a lowered iron release rate from Tf is predicted to increase cellular association, even when the Tf ligand is conjugated to nanoparticles.

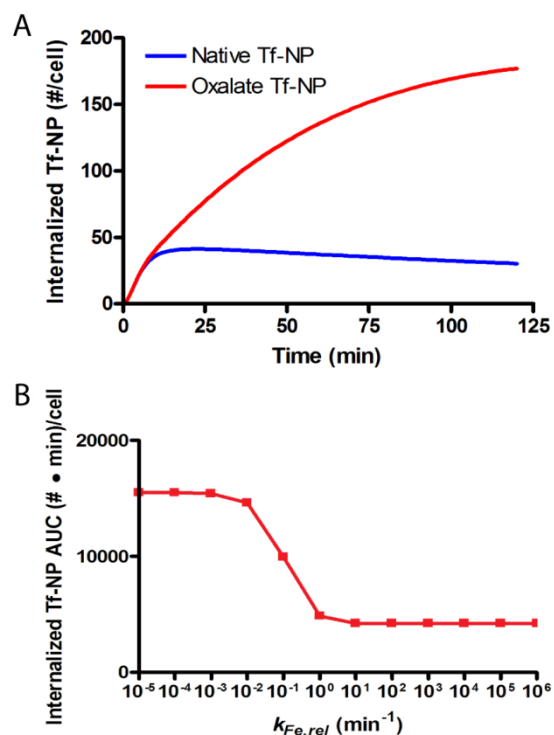


Figure 2.3. Representative predicted curves generated using k_r decreased by 1000-fold relative to that of the Tf molecule and a κ value of 0.01. (A) Internalized Tf/cell for oxalate Tf-NP ($k_{Fe,rel} = 10^{-3} \text{ min}^{-1}$) vs. native Tf-NP ($k_{Fe,rel} = 10^2 \text{ min}^{-1}$). (B) Area under the curve values for plots of internalized Tf/cell vs. time for a range of iron release rates.

2.3.2 Characterization of Tf-PNP

According to the vendor, the number of free surface amine functional groups ($-\text{NH}_2$) on PNP was estimated to be approximately 3000. We therefore used a 5000-fold molar excess of SPDP to PNP to ensure that most of the surface amines would be activated for conjugation. We also used a 5000:1 molar ratio of Tf:PNP to ensure that the maximum amount of Tf could be conjugated to the surface of PNP. The diameters, zeta potentials, and polydispersity indices of PNP and Tf-PNP are shown in Table 2.1.

Table 2.1. Characterization of PNP and Tf-PNP.

Parameter	PNP	Tf-PNP
-----------	-----	--------

Diameter	105 ± 1 nm	125 ± 1 nm
Zeta potential	$+48.3 \pm 3.6$ mV	$+32.1 \pm 3.6$ mV
Polydispersity index	0.098 ± 0.005	0.103 ± 0.023
Tf # per PNP	--	1300

Tf is a 78 kDa protein with dimensions of 9.5 nm x 6 nm x 5 nm [108]. The diameter of Tf-PNP was found to be 125 ± 1 nm, which is 20 nm longer than the diameter of PNP, suggesting that a Tf monolayer was conjugated to the PNP.

At physiological pH, positively charged PNP is favored due to the protonation of its surface amine functional groups. Tf, on the other hand, is slightly negatively charged ($pI = 5.5 - 6.1$) [109]. As expected, the zeta potential measurements, which quantified the surface charge of Tf-PNP, showed that Tf-PNP has a lower zeta potential value of $+32.1 \pm 3.6$ mV, compared to the zeta potential value of PNP ($+48.3$ mV). Nevertheless, since the zeta potential of Tf-PNP is above $+30$ mV, Tf-PNP should remain stable at physiological pH. The small value of the polydispersity index of Tf-PNP suggests that the purification process had removed most impurities following conjugation.

The BCA protein quantification assay was used to quantify the concentration of Tf, while a fluorescence standard curve constructed with known PNP concentrations was used to quantify the concentrations of PNP in the Tf-PNP samples. The Tf:PNP ratio was calculated and found to be approximately 1:1300, indicating that 1300 Tf molecules were conjugated to each PNP.

2.3.3 Intracellular trafficking of Tf and Tf-PNP samples

Our group had previously demonstrated that Tf variants with slower iron release rates have a greater cellular association compared to native Tf. Consequently, these variants were shown to be more effective drug delivery vehicles, as a greater cellular association increases the probability of drug release once internalized into the cell. We therefore investigated NPs conjugated to these Tf variants to assess whether the Tf variants could increase the cellular association and thus, the therapeutic efficacy of the NPs as well. Oxalate Tf, which was previously shown to have a slower iron release rate, was used for this study [96, 97].

The first step was to confirm through trafficking experiments that oxalate Tf and oxalate Tf-PNP exhibit a greater cellular association in PC3 human prostate cancer and A549 human lung cancer cells when compared to their native Tf counterparts. The concentration of radiolabeled holo-Tf used in our trafficking experiments was 1 nM, which is lower than the equilibrium dissociation constant (K_D) of holo-Tf binding to TfR (5 – 13 nM) [110] and would therefore avoid saturation of TfR on the cell surface. The concentration of Tf-PNP used in this experiment was 0.75 pM, which is also lower than the predicted K_D of Tf-PNP binding to TfR (see Chapter 3).

Our results from the trafficking studies are shown in Fig. 2.4. After 2 h of incubation with PC3 cells, the internalization level of native Tf had reached 4×10^4 molecules per cell, while the internalized oxalate Tf was significantly higher at 9×10^4 molecules per cell. For Tf-PNP, similar results were observed. After 2 h of incubation, the internalized level of native Tf-PNP had reached 7 NPs per cell, while oxalate Tf-PNP had reached 17 NPs per cell.

The area under the curve (AUC) of each of these plots was used as a metric for cellular association, since this quantity reflects the cumulative exposure of the cells to a drug if it is

conjugated to Tf or loaded into Tf-PNP. For the PC3 cells, the average AUC values were 3.57×10^6 and 6.72×10^6 (#*min)/cell for native Tf and oxalate Tf, respectively, indicating an AUC increase of 88% between oxalate and native Tf ($P < 0.0001$). For Tf-PNP, the average AUC values were 5.52×10^2 and 1.36×10^3 (#*min)/cell for native Tf-PNP and oxalate Tf-PNP, respectively, for an AUC increase of 147% ($P < 0.0001$). For the A549 cell line, the average AUC values were 1.77×10^6 and 4.38×10^6 (#*min)/cell for native Tf and oxalate Tf, respectively, translating into an AUC increase of 147% ($P < 0.0001$). For Tf-PNP, the average AUC values were 6.05×10^2 and 2.06×10^3 (#*min)/cell for native Tf-PNP and oxalate Tf-PNP, respectively, for an increase of 240% ($P = 0.0037$).

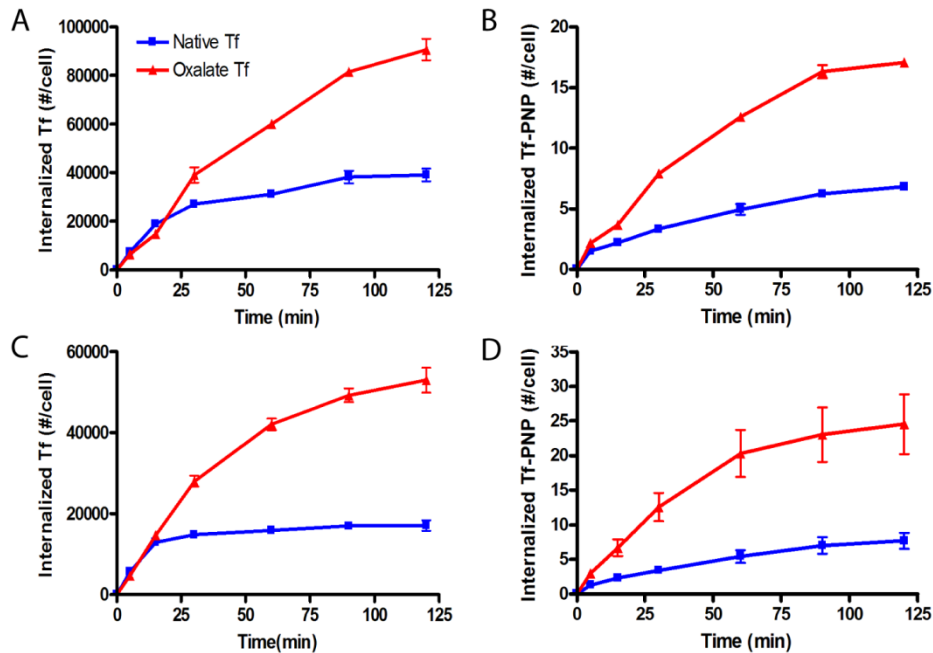


Figure 2.4. Results of the intracellular trafficking studies. Number of internalized (A) Tf and (B) Tf-PNP per PC3 cell and (C) Tf and (D) Tf-PNP per A549 cell are plotted as a function of time for native and oxalate Tf (at 1 nM) and Tf-PNP (at 0.75 pM). Error bars represent standard errors of the mean from an average of at least four measurements.

2.3.4 Characterization of DP and TPDP

After demonstrating the increased cellular association of oxalate Tf-PNP, another nanoparticle system was investigated that was able to encapsulate and release drug. This led to the development of DP, which can be prepared by nanoprecipitation. Our characterization indicated that our DP samples had a similar diameter to PNP, were monodisperse, and exhibited colloidal stability (Table 2.2). In order to perform *in vivo* experiments, the DPs were PEGylated to achieve steric stabilization. Subsequently, native or oxalate Tf was conjugated onto PEG to form TPDP. Similar to the conjugation of Tf to PNP, a 5000:1 molar ratio of Tf:DP was used during conjugation. The increased diameter of TPDP from DP indicated successful conjugation, with about 1100 Tf on the particle surface. The zeta potential value dropped from -27.5 mV to -15.0 mV due to the replacement of some of the negatively charged carboxyl groups by the neutral PEG molecules. Although -15.0 mV is greater than -30.0 mV, these nanoparticles still exhibited colloidal stability due to the steric stabilization provided by PEG. The loading ratio of DOX in DP was approximately 1.8%, which is comparable to values found in the literature [111-114].

Table 2.2. Characterization of DP and TPDP.

Parameter	DP	TPDP
Diameter	99.4 ± 0.2 nm	126 ± 2 nm
Zeta potential	-27.5 ± 0.2 mV	-15.0 ± 0.7 mV
Polydispersity index	0.071 ± 0.008	0.112 ± 0.021
Tf # per NP	--	1100

2.3.5 In vitro cytotoxicity of TPDPs

The MTS assay was performed to determine the potency of native TPDP and oxalate TPDP on PC3 and A549 cells. The cytotoxicity results of native and oxalate TPDP are shown in Fig. 2.5. The plots indicate that oxalate TPDP is more potent than native TPDP as less of the drug in oxalate TPDP is required to achieve the same growth inhibition as that in native TPDP. The IC_{50} value was used as a metric to quantify the potency of TPDP samples. Quantitatively, the IC_{50} values were $0.122 \pm 0.016 \mu\text{M}$ and $0.055 \pm 0.008 \mu\text{M}$ for native TPDP and oxalate TPDP in PC3 cells, respectively. The IC_{50} values were $0.518 \pm 0.040 \mu\text{M}$ and $0.242 \pm 0.042 \mu\text{M}$ for native TPDP and oxalate TPDP in A549 cells, respectively. The lower IC_{50} value of oxalate TPDP indicates greater potency compared to native TPDP ($P = 0.0041$ for PC3; $P = 0.0094$ for A549), since a lower concentration of drug is required to achieve the same therapeutic effect. *In vitro* cytotoxicity studies with both native and oxalate TPDP in human umbilical vein endothelial cells (HUVECs), which are normal cells that do not overexpress TfR, were also performed (see Chapter 3). Both native and oxalate TPDP were less toxic towards normal cells compared with cancer cells. In addition, oxalate TPDP did not exhibit greater cytotoxicity than native TPDP towards normal cells, indicating that the enhanced drug delivery efficacy of oxalate TPDP should not cause increased toxicity towards normal cells, due to the lower number of TfR molecules on normal cells.

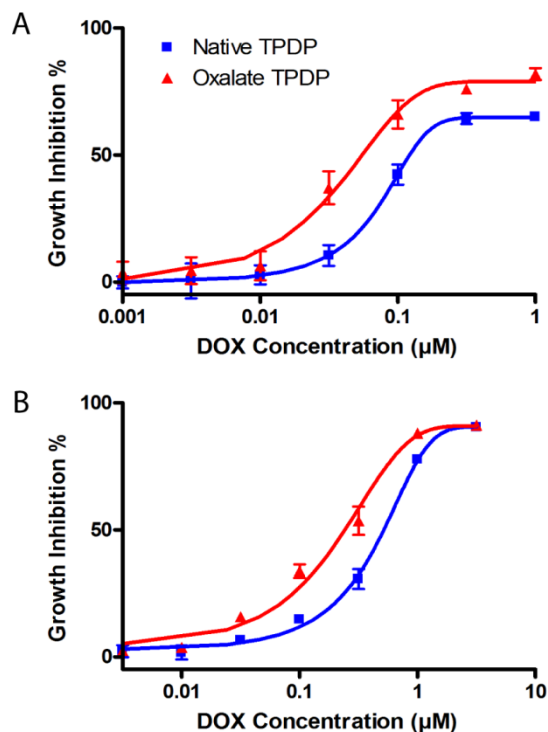


Figure 2.5. *In vitro* cytotoxicity comparisons between native and oxalate TPDPs in (A) PC3 and (B) A549 cells. Error bars represent standard errors of the mean from an average of three measurements.

2.3.6 *In vivo* efficacy of TPDP delivered systemically to mice

Having successfully demonstrated the ability to enhance the *in vitro* drug carrier efficacy of oxalate TPDP, the systemic delivery efficacy of the oxalate TPDP was determined through *in vivo* experiments. Specifically, oxalate TPDP, native TPDP, or a PBS control was injected intravenously into nude mice with established subcutaneous PC3 flank tumors. Only one i.v. injection was performed in each experiment. All mice involved in this study were examined and weighed every other day, and all mice gained weight at a similar rate throughout the study, suggesting that the systemic toxicity of the treatment could be minimal. Tumors on the mice in the PBS control group showed rapid growth, as no drugs were administered (Fig. 2.6). As a result, the 5 mice in the PBS control group were prematurely sacrificed within 2 weeks after the

PBS injection. The repeated measures mixed model analysis of the data indicated that the differences in tumor volume due to both time and the three treatment groups were statistically significant ($F(17,124) = 9.69, P < 0.0001$). Furthermore, tests of simple main effects indicated that mice treated with native TPDP showed a significant inhibition in tumor growth compared with mice treated with PBS control after day 4 ($P < 0.05$ after day 4, $P < 0.005$ after day 10). The delayed growth profile associated with tumors on mice treated with native TPDP confirms other reported findings that demonstrate the ability of Tf-conjugated nanoparticles to inhibit tumor growth. More importantly, mice treated with oxalate TPDP showed a significant inhibition in tumor growth compared with not only mice treated with PBS control after day 4 ($P < 0.005$), but also mice treated with native TPDP after day 14 ($P < 0.005$).

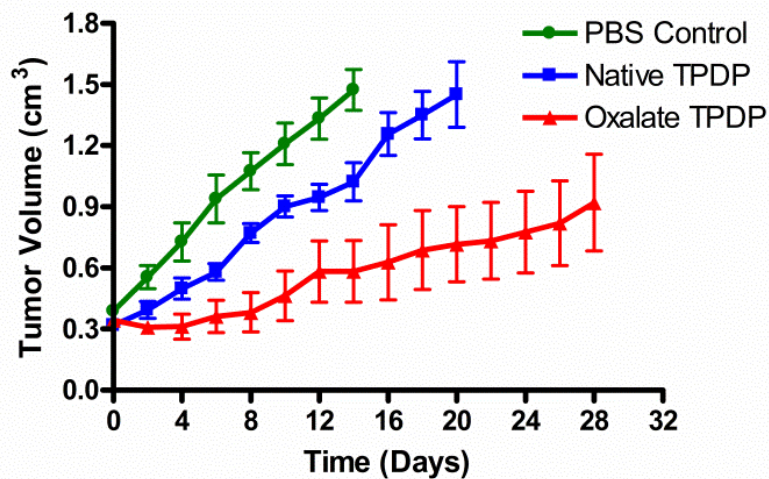


Figure 2.6. Tumor volume data for male nude mice with established PC3 flank tumors treated with the PBS control, native TPDP, or oxalate TPDP. The mean tumor volume was evaluated from an average of five tumors within each treatment group. The error bars represent standard errors of the mean from an average of five measurements. Only one i.v. injection was performed on day 0, which corresponds to when tumors reached volumes of 300 – 350 mm³.

2.4 Discussion

Tf has been widely used to target drugs to cancer cells, since many cancer cells overexpress TfR on their cell surfaces. However, Tf's short residence time in the cell (~5 to 10 min) limits the time frame it has to deliver a conjugated drug. In order to enhance Tf's efficacy as a drug carrier, our laboratory previously developed a mathematical model of the Tf/TfR intracellular trafficking pathway to identify novel design criteria for increasing Tf's cellular association. We identified the release rate of iron from Tf as a previously unidentified factor influencing the degree of cellular association, and demonstrated that oxalate Tf, with its lower iron release rate, associated with HeLa cervical cancer cells to a greater extent compared to native Tf [97]. Subsequently, we conjugated oxalate Tf to diphtheria toxin and demonstrated through *in vitro* cytotoxicity studies that the increased cellular association of oxalate Tf further translates into a greater potency towards cancer cells.

While our molecular Tf-drug conjugates can be used for cancers that are treated locally, they cannot be administered systemically due to competition from endogenous Tf, which is present at a high concentration. To address this challenge, researchers have used Tf as a targeting ligand on NPs with diameters between 60 and 400 nm, since these NPs have the ability to reach and accumulate in tumors via the EPR effect. Furthermore, NPs can outcompete endogenous Tf due to multivalency effects associated with multiple Tf on a NP. We therefore decided to expand upon our previous studies by comparing the therapeutic efficacy of NPs conjugated with oxalate Tf to those conjugated with native Tf. Our hypothesis was that oxalate Tf may also increase the cellular association, and consequently, the potency of the NPs towards cancer cells. These studies were performed with oxalate Tf, instead of the genetically engineered Tf mutants, because the Tf:NP ratio remains constant between the native and oxalate Tf-NP

samples. Specifically, Tf is first conjugated to the NPs, and the population is then split and either carbonate or oxalate is loaded onto Tf. This allows us to focus entirely on the difference between the iron release rates of native and oxalate Tf without interference from any effects associated with conjugating different numbers of Tf molecules to the NPs.

Our extended mathematical model predicted that oxalate Tf would still lead to increased cellular association, even when conjugated to NPs. To confirm this experimentally, we performed trafficking experiments in the hopes of demonstrating that oxalate Tf and oxalate Tf-NPs exhibit a greater cellular association with PC3 human prostate carcinoma cells and A549 human lung carcinoma cells when compared to their native Tf counterparts. PNP was utilized as our model NP, since it is monodisperse, has abundant amines on its surface for conjugation, and has the ability to encapsulate a hydrophobic dye, which is useful for quantification. More importantly, unlike PLGA NP, which can degrade with time to release its encapsulated cargo, PNP is rigid and does not degrade, allowing the investigation of the trafficking behavior without confounding effects.

Our trafficking experiments with Tf-PNPs demonstrated that oxalate Tf-PNP also exhibits an increased cellular association in both PC3 and A549 cell lines, thereby supporting our hypothesis. These results were encouraging, since the greater cellular association of oxalate Tf ultimately led to an enhanced delivery of the drug diphtheria toxin in our previous *in vitro* and *in vivo* studies with Tf-drug molecular conjugates. To investigate whether oxalate Tf-NPs could yield similar results, we produced PLGA NPs encapsulating the chemotherapeutic DOX. DOX and PLGA were chosen in this study as both components have been well established and approved by the FDA, and the DOX encapsulated PLGA nanoparticle system has also been well

studied [111, 115]. The particles were then PEGylated, followed by conjugation with Tf and loading of Tf with carbonate or oxalate.

Prior to our *in vitro* and *in vivo* studies, we examined the toxicity of the carriers without drug (*i.e.*, PLGA NP and Tf-conjugated PEGylated PLGA NP), and they were found to be minimally toxic in the concentration range of interest. Our results confirmed that the increased cellular association of oxalate TPDP did translate into better drug potency. Quantitatively, from our *in vitro* cytotoxicity experiments, there were 2.21- and 2.14-fold decreases in IC₅₀ values between native and oxalate TPDP in PC3 and A549 cells, respectively. Moreover, our *in vivo* studies demonstrated significant tumor growth inhibition by our oxalate TPDP. It is important to note that only a single i.v. injection was employed in this study. By increasing the dose per weight in a single injection or administering multiple injections of similar or smaller doses, we may be able to achieve complete tumor regression with the oxalate TPDP without causing systemic side effects to the mice. This chapter presents our cumulative work that was presented at three recent meetings [116-118]. Since these presentations, Yang and coworkers published a manuscript that demonstrated that oxalate Tf conjugated quantum dots (<50 nm) have a longer cellular association when injected intratumorally to a nude mouse xenograft [119]. It is rewarding to see that our work with engineered Tf proteins for drug delivery continues to be successful.

2.5 Conclusion

In conclusion, we are the first to use oxalate Tf to improve the targeted delivery of drug-encapsulated NPs to cancer cells. While various classes of NPs that target the transferrin receptor have attained some clinical success [89-91], we wanted to further improve their

efficacy, since it is known that Tf has a short residence time inside the cell (i.e., low cellular association), thus limiting its probability of delivering its drug payload. Previous members of our lab developed a mathematical model that led to the engineering of oxalate Tf, which exhibits a lower iron release rate and greater cellular association than native Tf. Building upon our successes with *in vitro* and *in vivo* studies performed with molecular variant Tf-diphtheria toxin conjugates, we wanted to see if we could achieve similar results with NPs encapsulating the drug doxorubicin. We first extended our mathematical model to predict that oxalate Tf-NPs can also achieve greater cellular association and cytotoxicity relative to native Tf-NPs. This was confirmed through *in vitro* intracellular trafficking studies and *in vitro* cytotoxicity studies in A549 and PC3 cancer cells. These promising results motivated us to perform *in vivo* studies using PC3 flank tumors generated in mice. These results demonstrated that oxalate TPDP suppressed tumor growth much more effectively than native TPDP. Our fundamental understanding of the Tf system and the accumulation of our Tf variant results over many years, including our recent intravenous injection into mouse xenograft models, lead us to believe that the conjugation of Tf variants onto existing NPs has potential in the future to improve upon Tf-conjugated NPs currently undergoing clinical trials.

Chapter 3: Mathematical model for nanoparticles conjugated with a transferrin variant and *in vitro* studies with non-cancerous cells

This chapter details the mathematical model that we derived for transferrin variant conjugated nanoparticles along with our *in vitro* experiments with human umbilical vein endothelial cells (HUVECs). The theoretical and experimental studies described in this chapter support the investigation presented in Chapter 2.

3.1 Mathematical model for Tf-NP cellular trafficking pathway

Our previous mathematical model for molecular transferrin, which was derived using the principles of mass action kinetics, was extended to reflect two key characteristics of the nanoparticle platform. The dissociation rate constants of iron-bound Tf-NP (FeTf-NP) for Tf receptor (TfR) on the cell surface and within the endosome were decreased (see “Estimation of the equilibrium dissociation constant of Tf-NP” below) in order to capture the increase in probability of binding when multiple Tf are conjugated to a nanoparticle. Additionally, the vesicle/tubule partition coefficient was varied to account for the larger size of Tf-NPs in comparison to molecular Tf.

Bulk and surface equations

Species balance for bulk extracellular iron-bound Tf-NP (FeTfNP)

$$\begin{aligned}
 \frac{d(FeTfNP_{bulk})}{dt} &= (-k_{FeTfNP,f}FeTfNP_{bulk}TfR_{surf} + k_{FeTfNP,r}FeTfNP_{TfR_{surf}} \\
 &+ k_{rec}FeTfNP_{rec})\frac{n_{cell}}{V_{bulk}N_A} \quad (3.1)
 \end{aligned}$$

Species balance for bulk extracellular iron-free Tf-NP (TfNP)

$$\begin{aligned}
 \frac{d(TfNP_{bulk})}{dt} &= (-k_{TfNP,f}TfNP_{bulk}TfR_{surf} + k_{TfNP,r}TfNP_{TfR_{surf}} \\
 &+ k_{rec}TfNP_{rec})\frac{n_{cell}}{V_{bulk}N_A} \quad (3.2)
 \end{aligned}$$

Species balance for surface TfR

$$\begin{aligned}
 \frac{d(TfR_{surf})}{dt} &= -k_{FeTfNP,f}FeTfNP_{bulk}TfR_{surf} + k_{FeTfNP,r}FeTfNP_{TfR_{surf}} \\
 &- k_{TfNP,f}TfNP_{bulk}TfR_{surf} + k_{TfNP,r}TfNP_{TfR_{surf}} - k_{int}TfR_{surf} \\
 &+ k_{rec}TfR_{rec} + k_{deg}TfR_{deg} + k_{deg}FeTfNP_{TfR_{deg}} \\
 &+ k_{deg}TfNP_{TfR_{deg}} \quad (3.3)
 \end{aligned}$$

Species balance for surface FeTfNP/TfR complex

$$\begin{aligned}
 & \frac{d(FeTfNP_{TfR_{surf}})}{dt} \\
 & = k_{FeTfNP,f}FeTfNP_{bulk}TfR_{surf} - k_{FeTfNP,r}FeTfNP_{TfR_{surf}} \\
 & - k_{int}FeTfNP_{TfR_{surf}} + k_{rec}FeTfNP_{TfR_{rec}} \quad (3.4)
 \end{aligned}$$

Species balance for surface TfNP/TfR complex

$$\begin{aligned}
 & \frac{d(TfNP_{TfR_{surf}})}{dt} \\
 & = k_{TfNP,f}TfNP_{bulk}TfR_{surf} - k_{TfNP,r}TfNP_{TfR_{surf}} - k_{int}TfNP_{TfR_{surf}} \\
 & + k_{rec}TfNP_{TfR_{rec}} \quad (3.5)
 \end{aligned}$$

Vesicular equations

Species balance for vesicular FeTfNP

$$\begin{aligned}
 & \frac{d(FeTfNP_{ves})}{dt} \\
 & = -k_{Fe,rel}FeTfNP_{ves} - \frac{k_{endo,f}FeTfNP_{ves}TfR_{ves}}{N_A V_{endo}} + k_{endo,r}FeTfNP_{TfR_{ves}} \\
 & - \frac{k_{endo,f}FeTfNP_{ves}TfR_{tub}}{N_A V_{endo}} + \frac{k_{endo,r}FeTfNP_{TfR_{tub}}}{\kappa} - k_{sv}FeTfNP_{ves} \\
 & - k_{st}FeTfNP_{ves} \quad (3.6)
 \end{aligned}$$

Species balance for vesicular TfNP

$$\begin{aligned}
\frac{d(TfNP_{ves})}{dt} &= k_{Fe,rel}FeTfNP_{ves} - \frac{k_{endo,f}TfNP_{ves}TfR_{ves}}{N_A V_{endo}} + k_{endo,r}TfNP_TfR_{ves} \\
&\quad - \frac{k_{endo,f}TfNP_{ves}TfR_{tub}}{N_A V_{endo}} + \frac{k_{endo,r}TfNP_TfR_{tub}}{\kappa} - k_{sv}TfNP_{ves} \\
&\quad - k_{st}TfNP_{ves}
\end{aligned} \tag{3.7}$$

Species balance for vesicular TfR

$$\begin{aligned}
\frac{d(TfR_{ves})}{dt} &= k_{int}TfR_{surf} - \frac{k_{endo,f}FeTfNP_{ves}TfR_{ves}}{N_A V_{endo}} + k_{endo,r}FeTfNP_TfR_{ves} \\
&\quad - \frac{k_{endo,f}TfNP_{ves}TfR_{ves}}{N_A V_{endo}} + k_{endo,r}TfNP_TfR_{ves} - \gamma TfR_{ves} \\
&\quad - k_{sv}TfR_{ves}
\end{aligned} \tag{3.8}$$

Species balance for vesicular FeTfNP/TfR complex

$$\begin{aligned}
&\frac{d(FeTfNP_TfR_{ves})}{dt} \\
&= k_{int}FeTfNP_TfR_{surf} - k_{Fe,rel}FeTfNP_TfR_{ves} + \frac{k_{endo,f}FeTfNP_{ves}TfR_{ves}}{N_A V_{endo}} \\
&\quad - k_{endo,r}FeTfNP_TfR_{ves} - \gamma FeTfNP_TfR_{ves} \\
&\quad - k_{sv}FeTfNP_TfR_{ves}
\end{aligned} \tag{3.9}$$

Species balance for vesicular TfNP/TfR complex

$$\begin{aligned}
\frac{d(TfNP_TfR_{ves})}{dt} &= k_{int}TfNP_TfR_{surf} + k_{Fe,rel}FeTfNP_TfR_{ves} + \frac{k_{endo,f}TfNP_{ves}TfR_{ves}}{N_A V_{endo}} \\
&- k_{endo,r}TfNP_TfR_{ves} - \gamma TfNP_TfR_{ves} \\
&- k_{sv}TfNP_TfR_{ves}
\end{aligned} \tag{3.10}$$

Tubular equations

Species balance for tubular TfR

$$\begin{aligned}
\frac{d(TfR_{tub})}{dt} &= -\frac{\kappa k_{endo,f}FeTfNP_{ves}TfR_{tub}}{N_A V_{endo}} + k_{endo,r}FeTfNP_TfR_{tub} \\
&- \frac{\kappa k_{endo,f}TfNP_{ves}TfR_{tub}}{N_A V_{endo}} + k_{endo,r}TfNP_TfR_{tub} + \gamma TfR_{ves} \\
&- k_{st}TfR_{tub}
\end{aligned} \tag{3.11}$$

Species balance for tubular FeTfNP/TfR complex

$$\begin{aligned}
\frac{d(FeTfNP_TfR_{tub})}{dt} &= -k_{Fe,rel}FeTfNP_TfR_{tub} + \frac{\kappa k_{endo,f}FeTfNP_{ves}TfR_{tub}}{N_A V_{endo}} \\
&- k_{endo,r}FeTfNP_TfR_{tub} + \gamma FeTfNP_TfR_{ves} \\
&- k_{st}FeTfNP_TfR_{tub}
\end{aligned} \tag{3.12}$$

Species balance for tubular TfNP/TfR complex

$$\begin{aligned}
 \frac{d(TfNP_TfR_{tub})}{dt} &= k_{Fe,rel}FeTfNP_TfR_{tub} + \frac{\kappa k_{endo,f}TfNP_{ves}TfR_{tub}}{N_A V_{endo}} - k_{endo,r}TfNP_TfR_{tub} \\
 &+ \gamma TfNP_TfR_{ves} \\
 &- k_{st}TfNP_TfR_{tub}
 \end{aligned} \tag{3.13}$$

Degradation equations

Species balance for degraded FeTfNP

$$\frac{d(FeTfNP_{deg})}{dt} = k_{sv}FeTfNP_{ves} - k_{deg}FeTfNP_{deg} \tag{3.14}$$

Species balance for degraded TfNP

$$\frac{d(TfNP_{deg})}{dt} = k_{sv}TfNP_{ves} - k_{deg}TfNP_{deg} \tag{3.15}$$

Species balance for degraded TfR

$$\frac{d(TfR_{deg})}{dt} = k_{sv}TfR_{ves} - k_{deg}TfR_{deg} \tag{3.16}$$

Species balance for degraded FeTfNP/TfR complex

$$\frac{d(FeTfNP_TfR_{deg})}{dt} = k_{sv}FeTfNP_TfR_{ves} - k_{deg}FeTfNP_TfR_{deg} \tag{3.17}$$

Species balance for degraded TfNP/TfR complex

$$\frac{d(TfNP_TfR_{deg})}{dt} = k_{sv}TfNP_TfR_{ves} - k_{deg}TfNP_{TfR_{deg}} \quad (3.18)$$

Recycling equations

Species balance for recycled FeTfNP

$$\frac{d(FeTfNP_{rec})}{dt} = \kappa k_{st}FeTfNP_{ves} - k_{rec}FeTfNP_{rec} \quad (3.19)$$

Species balance for recycled TfNP

$$\frac{d(TfNP_{rec})}{dt} = \kappa k_{st}TfNP_{ves} - k_{rec}TfNP_{rec} \quad (3.20)$$

Species balance for recycled TfR

$$\frac{d(TfR_{rec})}{dt} = k_{st}TfR_{tub} - k_{rec}TfR_{rec} \quad (3.21)$$

Species balance for recycled FeTfNP/TfR complex

$$\frac{d(FeTfNP_TfR_{rec})}{dt} = k_{st}FeTfNP_TfR_{tub} - k_{rec}FeTfNP_{TfR_{rec}} \quad (3.22)$$

Species balance for recycled TfNP/TfR complex

$$\frac{d(TfNP_TfR_{rec})}{dt} = k_{st}TfNP_TfR_{tub} - k_{rec}TfNP_{TfR_{rec}} \quad (3.23)$$

Internalized TfNP equation

Species balance for total internalized TfNP

$$\begin{aligned}
 \text{Internalized} = & (1 + \kappa)FeTfNP_{ves} + (1 + \kappa)TfNP_{ves} + FeTfNP_{TfR_{ves}} + TfNP_{TfR_{ves}} \\
 & + FeTfNP_{TfR_{tub}} + TfNP_{TfR_{tub}} + FeTfNP_{rec} + TfNP_{rec} + FeTfNP_{TfR_{rec}} \\
 & + TfNP_{TfR_{rec}} + FeTfNP_{deg} + TfNP_{deg} + FeTfNP_{TfR_{deg}} \\
 & + TfNP_{TfR_{deg}} \quad (3.24)
 \end{aligned}$$

Table 3.1. List of parameters in the Tf-NP intracellular trafficking model.

Rate Constant	Definition	Value	Reference
$k_{FeTfNP,f}$	Association rate constant of FeTf-NP for TfR	$(4 \pm 1) \times 10^7 \text{ M}^{-1} \text{ min}^{-1}$	[94, 120]
$k_{FeTfNP,r}$	Dissociation rate constant of FeTf-NP for TfR	$(1.3 \pm 0.5) \times 10^{-3} \text{ min}^{-1}$	[94]and Est.
$k_{TfNP,f}$	Association rate constant of Tf-NP for TfR	$0 \text{ M}^{-1} \text{ min}^{-1}$	[121]
$k_{TfNP,r}$	Dissociation rate constant of Tf-NP for TfR	2.6 min^{-1}	[122]
$k_{endo,f}$	Endosomal association rate constant of FeTf-NP for TfR	$(4.4 \pm 0.4) \times 10^7 \text{ M}^{-1} \text{ min}^{-1}$	[121]
$k_{endo,r}$	Endosomal dissociation rate constant of FeTf-NP for TfR	$(5.6 \pm 1.2) \times 10^{-5} \text{ min}^{-1}$	[121]and Est.
k_{int}	TfR-mediated internalization	$3.0 \times 10^{-1} \text{ min}^{-1}$	[122]

	rate constant		
$k_{Fe,rel}$	Endosomal Tf iron release rate constant	$1.0 \times 10^2 \text{ min}^{-1a}$ $1.0 \times 10^{-3} \text{ min}^{-1b}$	Est.
k_{sv}	TfR-mediated vesicle to degradation rate constant	$1.2 \times 10^{-1} \text{ min}^{-1}$	[123]
k_{st}	TfR-mediated tubule to recycling rate constant	$5.3 \times 10^{-1} \text{ min}^{-1}$	[123]
k_{deg}	TfR-mediated degradation rate constant	$6.0 \times 10^{-2} \text{ min}^{-1}$	[123]
k_{rec}	TfR-mediated recycling rate constant	$1.5 \times 10^{-1} \text{ min}^{-1}$	[123]
κ	Vesicle/tubule partition coefficient	0.001 – 0.1	N/A
γ	TfR-mediated vesicle to tubule rate constant	1.0 min^{-1}	[123]
n_{cell}	Cell number	4×10^5 cells	N/A
V_{bulk}	Bulk media volume	1×10^{-3} L	N/A
V_{endo}	Endosomal volume	1.0×10^{-14} L	[123]
N_A	Avogadro's number	$6.02 \times 10^{23} \text{ mol}^{-1}$	N/A

^aNative Tf-NP

^bOxalate Tf-NP

3.2 Estimation of the equilibrium dissociation constant of Tf-NP

An equation relating the equilibrium dissociation constant of Tf-NP binding TfR to that of Tf binding TfR was derived in order to obtain more representative values of $k_{FeTfNP,r}$ and $k_{endo,r}$

(see Table 3.1), and to determine the concentration of Tf-NP to be used for trafficking experiments. The derivation below was performed for cell-surface binding of Tf to TfR, but an analogous derivation applies to the analogous endosomal event.

Let's first start with the equilibrium dissociation constant of Tf binding to TfR:

$$K_{D,Tf} = \frac{[Tf][TfR]}{[Tf - TfR]} \quad (3.25)$$

where [Tf] is the concentration of free Tf, [TfR] is the number of cell-surface TfR molecules per cell, and [Tf-TfR] is the number of cell-surface Tf-TfR complexes. Rearranging Eq. (3.25) leads to:

$$[Tf - TfR] = \frac{[Tf][TfR]}{K_{D,Tf}} \quad (3.26)$$

Let's now write the expression for the equilibrium dissociation constant of TfNP:

$$K_{D,TfNP} = \frac{[TfNP][TfR]}{[TfNP - TfR]} \quad (3.27)$$

where [TfNP] is the concentration of Tf-NP, and [TfNP-TfR] is the number of cell-surface TfNP-TfR complexes. Assuming there are 1000 Tf molecules per NP and that one Tf-NP binds to only one TfR:

$$[TfNP - TfR] = \sum_{i=1}^{1000} [TfNP - TfR]_i \quad (3.28)$$

where i is used to index the particular Tf on the NP, and $[TfNP - TfR]_i$ is the number of cell-surface TfNP-TfR complexes when Tf number i on the nanoparticle is bound to TfR. Note that

Eq. (3.28) states that the total number of cell-surface TfNP-TfR complexes is equal to the sum of the different TfNP-TfR complexes where different Tf molecules on NP are bound to TfR. If we assume that each individual Tf molecule on the particle still has the ability to bind to a TfR molecule with a K_D of Tf alone,

$$K_{D,Tf} = \frac{[TfNP][TfR]}{[TfNP - TfR]_i} \quad (3.29)$$

Solving Eq. (3.29) for $[TfNP - TfR]_i$ and substituting the result into Eq. (3.28) yields:

$$[TfNP - TfR] = \sum_{i=1}^{1000} \frac{[TfNP][TfR]}{K_{D,Tf}} = 1000 \frac{[TfNP][TfR]}{K_{D,Tf}} \quad (3.30)$$

Substituting Eq. (3.30) into Eq. (3.27) gives rise to:

$$K_{D,TfNP} = \frac{K_{D,Tf}}{1000} = \frac{1 \text{ nM}}{1000} \quad (3.31)$$

Accordingly, the K_D of Tf-NP is theoretically 1000-fold less than that of Tf if (i) there are 1000 Tf molecules per NP, (ii) each Tf binds with the K_D of Tf alone, and (iii) one NP can bind to only one TfR molecule. This predicted decrease in K_D is due to the increase in the probability of binding. The binding of Tf-NP with TfR to form complexes is entropically favored, since there are many possible configurations for different Tf molecules on a NP to bind to TfR. Moreover, although all Tf on the NP may not have an equal chance of binding to TfR, multiple Tf on one NP translates to multiple opportunities for one Tf-NP to bind a receptor and form a complex.

We used 1 nM Tf in the native/oxalate Tf trafficking experiments. Accordingly, we used a concentration of 0.75 pM of Tf-PNP (a value lower than $(1/1000) \times (1 \text{ nM})$) for our Tf-PNP trafficking experiments.

3.3 *In vitro* cytotoxicity studies with a normal cell line

To demonstrate that the enhanced drug delivery efficacy of oxalate TPDP would not result in increased toxicity towards normal cells, *in vitro* cytotoxicity studies were also performed with human umbilical vein endothelial cells (HUVECs), which are normal cells that do not overexpress TfR. Briefly, HUVECs were seeded onto 96-well tissue culture plates with a seeding density of 4.5×10^4 cells/cm². Native or oxalate TPDP was prepared in growth medium, and their concentrations were varied from 0.0316 μM to 31.6 μM . After aspirating the original medium from each well, 100 μL of the prepared medium containing TPDP was added to each well and incubated for 72 h in a humidified environment (37°C, 5.0% CO₂). Subsequently, 20 μL of the MTS reagent were added to each well, and the plate was incubated for an additional 1 h. Cell viability relative to control wells (cells incubated in media without TPDP) was quantified by reading the visible light absorbance values at 490 nm and 700 nm with an Infinite F200 plate reader (Tecan System Inc., San Jose, CA). Each entire experiment was performed three times, where triplicate measurements were obtained for each concentration of TPDP in each experiment.

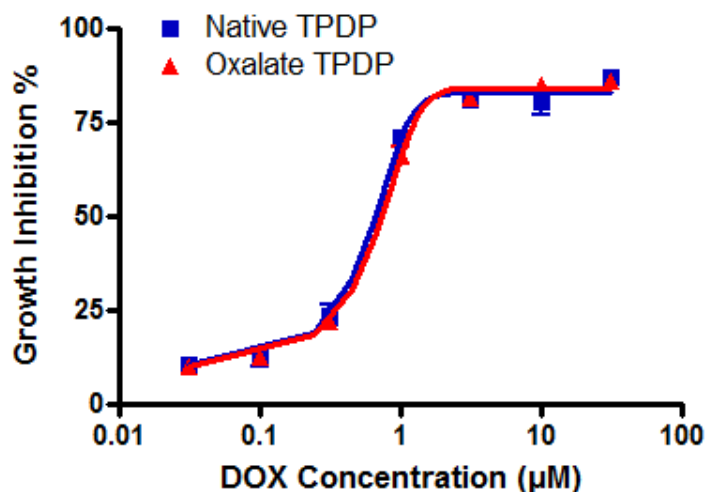


Figure 3.1. *In vitro* cytotoxicity comparisons between native and oxalate TPDPs in HUVECs. Error bars represent standard errors of the mean from an average of three measurements.

Both native and oxalate TPDP have higher IC_{50} values in HUVECs than in PC3 and A549 cells. The IC_{50} values in HUVECs were 0.658 ± 0.063 and 0.728 ± 0.076 μM for native and oxalate TPDP, respectively (see Figure 3.1). For reference, the IC_{50} values were 0.122 ± 0.016 μM and 0.055 ± 0.008 μM for native and oxalate TPDP in PC3 cells, respectively. The IC_{50} values were 0.518 ± 0.040 μM and 0.242 ± 0.042 μM for native and oxalate TPDP in A549 cells, respectively. This indicates that more of the drug was necessary to achieve 50% cellular growth inhibition in HUVECs than in PC3 and A549 cells. Additionally, the cytotoxicity curves for native and oxalate TPDP overlapped in the case for HUVECs, indicating that oxalate TPDP does not exhibit greater cytotoxicity than native TPDP towards HUVECs. These results confirm that the enhanced cytotoxicity of oxalate TPDP is significantly reduced for normal cells, as they do not express as much TfR on their surfaces.

Chapter 4: Enhancing the lateral-flow immunoassay for viral detection using an aqueous two-phase micellar system

4.1 Motivation and background

The recent outbreak of swine-origin influenza A (H1N1) virus infection [124] highlighted the need for a means to rapidly and accurately detect infectious agents and pandemic pathogens at the point-of-care (POC), which in turn could result in better patient management, such as timely use of appropriate antiviral treatments and isolation of confirmed cases, to aid in preventing outbreaks [125, 126]. One detection method that has gained much attention in recent years due to its ease of use, rapid time to result, and minimal power and laboratory equipment requirements is the lateral-flow (immuno)assay (LFA). LFA utilizes a test strip that collects a sample through lateral flow, and detects the presence of a target molecule through its specific antibody labeled with a colorimetric indicator. While LFA has been used to detect a wide range of biomolecules [127], its sensitivity in detecting viruses has been shown to range from 19% to 96% compared to the gold standards, namely viral culture and real-time PCR [126, 128-132]. Although LFA is superior to viral culture and real-time PCR in terms of ease of use and rapid time to result, its typically low sensitivity in detecting pathogens and viruses limits its effectiveness as a reliable POC assay for preventing pandemic outbreaks. Therefore, the sensitivity of LFA for detection of infectious viruses must first be improved before it can reliably be used as an effective POC solution.

One approach to achieve a higher sensitivity for LFA is to improve the assay itself. Another approach is to concentrate the target biomolecule prior to the detection step. The focus of this work is on the latter approach, and we investigated concentrating a target virus using an

aqueous two-phase system (ATPS) prior to its detection via LFA. Although ATPS have also been previously studied, the work reported here is novel and significant, since it represents the first time the established technologies of LFA and ATPS have been combined. In fact, ATPS, which can be formed with micelles (ATPMS), polymers (ATPPS), or a combination of the two, have generally been examined for large-scale biotechnological applications [133-139] and not small-scale diagnostic applications. ATPS are very appropriate for a POC device, since they are easy to use, can be rapid, and are scalable (to require minimal sample volume). Furthermore, ATPS also do not require any laboratory equipment and are low in cost compared to chromatography [140-142].

In this proof-of-principle study, an aqueous two-phase micellar system (ATPMS) comprised of the nonionic surfactant Triton X-114 and phosphate-buffered saline (PBS) was investigated for concentrating a model virus, namely bacteriophage M13 (M13). In an aqueous solution at concentrations above their critical micelle concentration (CMC), the surfactant molecules form micelles [143]. The Triton X-114 micellar system exhibits a homogeneous, isotropic phase at low temperatures. Upon increasing the temperature, the solution undergoes a macroscopic phase separation to yield a top, micelle-poor phase and a bottom, micelle-rich phase. Biomolecules would then distribute, or partition, unevenly between the two phases based on their physico-chemical characteristics, such as hydrophobicity [144] and size [145]. First, we wanted to gain an understanding of the main driving forces for M13 partitioning in the Triton X-114 micellar system to assess the predictability of the M13 partitioning behavior. Accordingly, the experimentally measured partitioning behavior of M13 was compared with our theoretical predictions based on a model developed recently for the partitioning of cylindrical biomolecules in ATPMS [139]. Next, M13 was concentrated in the top, micelle-poor phase by manipulating

the volume ratio (the volume of the top, micelle-poor phase divided by that of the bottom, micelle-rich phase). After ensuring that we could concentrate M13 in the ATPMS in a predictive manner, we developed an LFA for the detection of M13 in-solution. Once the detection limit of the immunoassay was established, M13 was concentrated by utilizing the ATPMS prior to the detection step to investigate the effect of the concentration step on the immunoassay's detection limit.

4.2 Materials and Methods

4.2.1 Culturing and Quantifying M13

Escherichia coli bacteria (American Type Culture Collection, ATCC, Manassas, VA) were incubated in 6 mL of lysogeny broth (LB, 10 g/L tryptone (BD, Franklin Lakes, NJ), 5 g/L yeast extract (BD), and 10 g/L NaCl) at 37°C and 240 rpm in a shaker incubator for 12 hours. In order to culture M13 (ATCC), 10 µL of the stock M13 solution was added to the cultured bacteria solution. The bacteria solution was then incubated in a shaker incubator at 37°C and 240 rpm for 5 hours. The solution was then centrifuged at 4°C and 8000 g for 15 min to remove the bacteria. The supernatant containing M13 was collected and filtered using a 0.22 µm syringe filter (Millipore, Billerica, MA).

As described previously [146], the plaque assay was used to quantify the concentration of M13 in-solution, and therefore, the concentration of M13 is reported as plaque forming units (pfu) per mL. All reagents and materials were purchased from Sigma-Aldrich (St. Louis, MO) unless otherwise noted.

4.2.2 Partitioning and Concentrating M13

For each M13 partitioning experiment, three identical 3.5 mL Triton X-114 solutions in Dulbecco's phosphate-buffered saline (PBS, Invitrogen, pH 7.4, containing 1.47 mM KH_2PO_4 , 8.10 mM Na_2HPO_4 , 137.93 mM NaCl, 2.67 mM KCl, and 0.49 mM MgCl_2) were prepared. M13 was added to the solutions at a concentration of 10^8 pfu/mL. In order to ensure that each solution is in one phase prior to phase separation, the solutions were equilibrated at 4°C prior to the addition of M13. Once M13 was added, the solutions were mixed and placed in a water bath set at the appropriate temperature which yielded a volume ratio equal to approximately 1. After incubating the three solutions in the water bath for 18 hours, the two coexisting micellar phases were withdrawn carefully using syringe and needle sets, and the concentration of M13 in each of the two phases was determined using the plaque assay. Each partitioning experiment, which involved triplicate solutions, was repeated at least twice.

By altering the volume ratio of the partitioning experiments, M13 can be concentrated in the top, micelle-poor phase. The same protocol described above for partitioning M13 was used, except that the initial Triton X-114 surfactant concentrations and operating temperatures were varied in order to achieve the desired volume ratios.

4.2.3 Preparing Colloidal Gold Probes

The colloidal gold nanoparticles were prepared according to Frens [68]. The colloidal gold-antibody probe was prepared as described by Horisberger and Clerc [147]. Briefly, the pH of a 2.5 mL colloidal gold nanoparticle solution was adjusted to pH 9 using 0.1 M NaOH. Subsequently, 40 μg of anti-M13 mouse monoclonal antibody (Abcam Inc., Cambridge, MA) at a concentration of 0.2 mg/mL was added to the colloidal gold solution and mixed for 10 min on a

shaker. To prevent nonspecific binding of other proteins to the surfaces of the colloidal gold nanoparticles, 250 μL of 10% w/v bovine serum albumin (BSA) was added to the mixture and mixed for 15 min on a shaker to block all excess surfaces on the colloidal gold nanoparticles. The mixture was then centrifuged for 30 min at 4°C and 9000 g to remove free antibody and BSA. The pellet, which contained the colloidal gold nanoparticles, was resuspended in 375 μL of 0.1 M sodium borate buffer, pH 9.

4.2.4 Preparing LFA Test Strips

There are two different approaches for the LFA: the sandwich assay and the competition assay. In this study, we implemented the sandwich assay. In the sandwich assay, antibodies specific for the target of interest are immobilized on a nitrocellulose membrane in the form of a line, called the test line. Secondary antibodies against the primary antibody are also immobilized on the nitrocellulose membrane in the form of a line, called the control line. In LFA, a sample first comes into contact with the colloidal gold probes. If the target molecules are present in the sample, they would first bind to their specific antibodies immobilized on the colloidal gold nanoparticles. Subsequently, as the colloidal gold nanoparticles move up the LFA strip, the target molecules present in the colloidal gold-antibody-target molecule complexes would bind to their specific antibodies immobilized on the test line. Due to the presence of “trapped” colloidal gold particles, which exhibit a purplish red color, a visual band is formed at the test line that indicates a positive result. Alternatively, if the target molecule is not present in the solution, the colloidal gold-complexed antibodies would not be “trapped” by the immobilized antibodies at the test line. This indicates a negative result. Furthermore, regardless of the presence of the target molecule in the sample, colloidal gold-complexed antibodies would bind and get “trapped”

by the immobilized secondary antibodies on the control line, which indicates a valid test. The LFA test strips used in this study were prepared using a similar approach to that of Schuurs and coworkers [148].

4.2.5 Performing LFA on M13

The operating condition that was used for performing the concentration step prior to the detection step resulted in M13 being concentrated in the top, micelle-poor phase with a Triton X-114 concentration of 0.065% w/w in PBS. Therefore, to be consistent between the immunoassays performed with or without the concentration step, solutions of M13 in 0.065% w/w Triton X-114 in PBS were used to perform the LFA without the concentration step. The LFA was performed as follows: Solutions containing varying M13 concentrations diluted in 0.065% w/w Triton X-114 in PBS were first prepared. 45 μL of the M13 solutions were then added to 10 μL of the colloidal gold probes solution and 25 μL of test buffer (0.2% BSA, 0.3% Tween20, 0.2% sodium azide, 0.1% polyethylene glycol, 0.1 M Trizma base, pH 8), which was used to facilitate the flow of the samples through the test strips. The resulting solutions were mixed, and incubated for 5 min before a test strip was dipped vertically into each solution so that only the sample pad would come in contact with the solution. After 20 min, the test strips were taken out of the solution, and an image of each strip was immediately taken by a Canon EOS 1000D camera (Canon U.S.A., Inc., Lake Success, NY).

4.2.6 Combining ATPMS with LFA

To combine the concentration step with the detection step, M13 was first concentrated following the same protocol as mentioned previously in *Partitioning and Concentrating M13*. Solutions containing 9.50% w/w Triton X-114 in PBS were used, and the solutions were incubated at 26.0°C for 18 hours. At these operating conditions, a volume ratio of 1/9 (0.111) was obtained. In addition, various amounts of M13 were added to each solution to obtain appropriate initial concentrations of M13. After phase separation, the top phases were withdrawn carefully using syringe and needle sets. The LFA was performed as described in *Performing LFA on M13*, except instead of using 45 µL of the M13 solutions diluted in 0.065% w/w Triton X-114 in PBS, 45 µL of the withdrawn top, micelle-poor phases were used.

4.3 Results and Discussion

4.3.1 Partitioning M13 in ATPMS

The partitioning behavior of a biomolecule in an ATPMS is quantified by evaluating the partition coefficient, K_{bm} , which is defined as follows:

$$K_{bm} \equiv \frac{C_{bm,t}}{C_{bm,b}} \quad (4.1)$$

where $C_{bm,t}$ and $C_{bm,b}$ are the concentrations of the biomolecule in the top and bottom phases, respectively. Based on its shape, M13 can be modeled as a cylindrical biomolecule. We had previously extended a model, which was developed by Blankschtein and coworkers [145, 149] for the partitioning of spherical, water-soluble proteins in ATPMS, to cylindrical biomolecules

(cb). This model incorporates the repulsive, steric, excluded-volume interactions that operate between the cylindrical biomolecule and the cylindrical micelles, and the following expression was derived for the partition coefficient of a cylindrical biomolecule, such as M13 [139]:

$$K_{cb}^{EV} = \exp \left[-(\phi_t - \phi_b) \left(I + \frac{l_{cb} R_{cb}^2}{l_m R_m^2} + \frac{I}{2} \left[\frac{R_m (l_m + R_m)(l_{cb} + \pi R_{cb}) + R_{cb} (l_{cb} + R_{cb})(l_m + \pi R_m)}{l_m R_m^2} \right] \right) \right] \quad (4.2)$$

where Φ_t and Φ_b are the surfactant volume fractions in the top and bottom phases, respectively, R_{cb} and R_m are the cross-sectional radii of the biomolecule and micelles, respectively, and l_{cb} and l_m are the lengths of the biomolecule and micelles, respectively. The cross-sectional radius of M13 was estimated to be 7 nm, and its length was estimated to be 900 nm [150]. The cross-sectional radius of Triton X-114 micelles was estimated to be 23.4 Å [139], while their lengths were estimated to be between 10 nm and 1 µm [151-155]. Based on Eq. (4.2), the values for the dimensions of M13 and Triton X-114 micelles, and the one-to-one correspondence between operating temperature and $(\Phi_t - \Phi_b)$ found previously [139], extremely large ($\gg 1000$) M13 partition coefficients as a function of temperature were predicted. However, as shown previously for the partitioning behavior of DNA fragments and spherical viruses in ATPMS [139, 156], the entrainment of micelle-poor domains in the macroscopic micelle-rich phase has a significant impact on the partitioning behavior of such large hydrophilic macromolecules.

Due to the small density difference and interfacial tension between the micelle-rich and micelle-poor domains, macroscopic phase separation equilibrium is not attained even after waiting a long time. As a result, some micelle-poor domains are entrained in the macroscopic micelle-rich phase, and similarly, some micelle-rich domains are entrained in the macroscopic micelle-poor phase. If M13 partitions extremely into the micelle-poor domains, as predicted by the model, the concentration of M13 in the micelle-poor domains would be orders-of-magnitude

greater than that in the micelle-rich domains. Therefore, the effect of entrained micelle-poor, M13-rich domains on the measured concentration of M13 in the macroscopic, micelle-rich, M13-poor phase would be drastic, while the effect of entrained micelle-rich, M13-poor domains on the measured concentration of M13 in the macroscopic, micelle-poor, M13-rich phase would be negligible. Defining x as the volume fraction of *micelle-poor domains* entrained in the bottom, macroscopic, micelle-rich phase, the newly predicted partition coefficient could be written as follows [139, 156]:

$$K_{M13}^{EV+Ent} = \frac{K_{M13}^{EV}}{1 + x \cdot (K_{M13}^{EV} - 1)} \quad (4.3)$$

where K_{M13}^{EV} is the partition coefficient of M13 based only on excluded-volume interactions. For large values of K_{M13}^{EV} , as in the case of M13 in ATPMS, Eq. (4.3) simplifies to:

$$\lim_{K_{M13}^{EV} \rightarrow \infty} K_{M13}^{EV+Ent} \approx \frac{1}{x} \quad (4.4)$$

Equation (4.4) indicates that the partition coefficient of M13 should only be dependent on x . It has also been shown by Blankschein and coworkers that x is only a function of the volume ratio [156]. Therefore, if the volume ratio is maintained at 1 for all temperatures, the measured partition coefficients for M13 should not change by varying the operating temperature. Fig. 4.1 shows the partition coefficients of M13 obtained experimentally at various operating temperatures, while the volume ratio was maintained at approximately 1. As expected and shown in Fig. 4.1, the partitioning behavior of M13 in the aqueous two-phase Triton X-114 micellar system is fairly insensitive to the operating temperature, suggesting that M13 partitioning is driven by the excluded-volume interactions between M13 and micelles, but is

limited by entrainment. Nevertheless, since the measured values of the M13 partition coefficients are much greater than 1, they can still be exploited as described below.

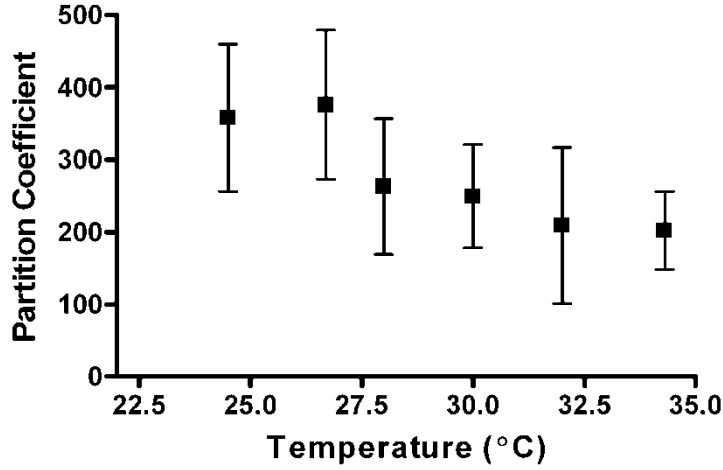


Figure 4.1. Experimentally measured partition coefficients for bacteriophage M13 at various temperatures. Error bars represent standard deviations from at least six measurements.

4.3.2 Concentrating M13 by Manipulating the Volume Ratio

In an approach similar to that developed previously [133], the concentration factor, that is, the concentration of the virus in the top phase divided by the initial concentration, can be expressed by using the following equation [139]:

$$\text{concentration factor} \equiv \frac{C_{M13,t}}{C_{M13,0}} = \frac{\frac{V_t}{V_b} + I}{\frac{V_t}{V_b} + \frac{I}{K_{M13}^m}} \quad (4.5)$$

where V_t and V_b are the volumes of the top and bottom phases, respectively, $C_{M13,0}$ is the initial concentration of M13 in the homogeneous micellar solution prior to phase separation, $C_{M13,t}$ is

the concentration of M13 in the top phase, and K_{M13}^m is the measured partition coefficient. For large values of K_{M13}^m , the concentration factor could be approximated as follows:

$$\text{concentration factor} \approx 1 + \frac{I}{\frac{V_t}{V_b}} \quad (4.6)$$

Based on Eq. (4.6), and the large values of K_{M13}^m obtained experimentally (Fig. 4.1), the concentration factor can be manipulated by simply varying the volume ratio. Therefore, the volume ratio was varied from 1 to approximately 1/8 (0.121), and a 2- to 7-fold concentration of M13 in the top phase was achieved (Fig. 4.2). In addition, as indicated in Fig. 4.2, there is reasonable agreement between the experimentally measured concentration factors and the predictions obtained from Eq. (4.6).

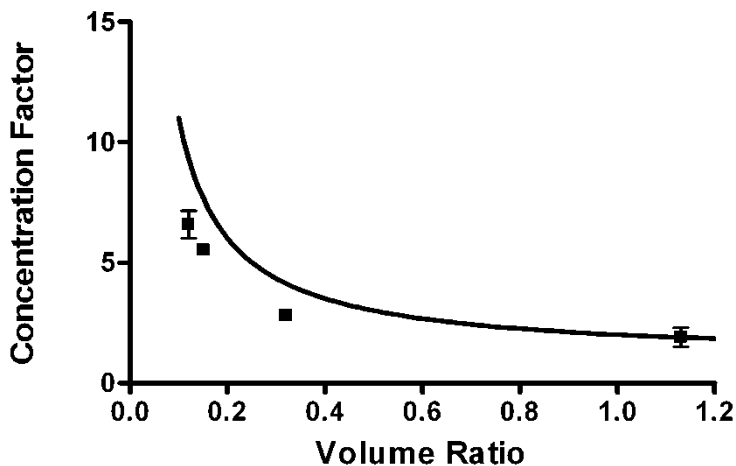


Figure 4.2. (a) Experimentally measured partition coefficients for M13 at various temperatures, and (b) comparison of experimentally measured (■) and theoretically predicted (—) M13 concentration factors for various volume ratios. Error bars represent standard deviations from at least three measurements

4.3.3 Detecting M13 via LFA

After demonstrating that M13 could be concentrated via an ATPMS, we prepared colloidal gold probes and LFA test strips by utilizing goat polyclonal anti-mouse IgG antibody and mouse monoclonal antibody to M13's coat protein pVIII. Figure 4.3 shows the LFA results. As mentioned previously, the presence of the top line, which contains immobilized goat polyclonal anti-mouse IgG antibody, indicates a valid test. The presence of the lower test line, which contains mouse monoclonal antibody to M13's coat protein pVIII, indicates the presence of M13. As indicated in Fig. 4.3, while no test line appeared for the negative control solution, which did not contain any M13, the intensity of the test line decreased with the decreasing concentration of M13 until the test line was no longer present for the solution containing 10^8 pfu/mL (Fig. 4.3f). This indicated a detection limit of approximately 5×10^8 pfu/mL for the M13 LFA performed without a prior concentration step.

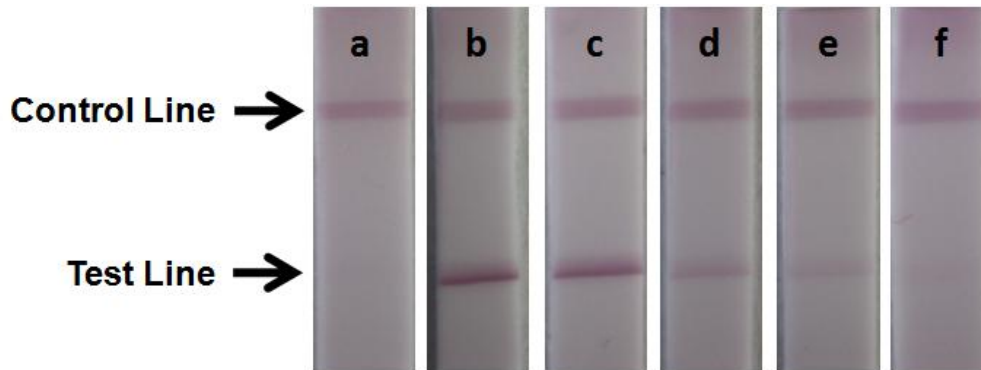


Figure 4.3. LFA used to detect M13 without a prior concentration step. The negative control without any M13 is shown in panel (a). The remaining solutions contained M13 at concentrations of (b) 1×10^{10} , (c) 5×10^9 , (d) 1×10^9 , (e) 5×10^8 , and (f) 1×10^8 pfu/mL

4.3.4 Concentrating M13 Prior to LFA

After establishing the detection limit, we investigated the possible improvement of the detection limit if M13 were to be concentrated by utilizing an ATPMS prior to the detection step.

To do so, 9.50% w/w Triton X-114 in PBS solutions with different initial concentrations of M13 were incubated at 26.0°C for 18 hours. At these operating conditions, a volume ratio of 1/9 was obtained, and based on Eq. (4.6), an approximately 10-fold concentration of M13 in the top, micelle-poor phase was predicted. After phase separation, the top, micelle-poor, M13-rich phases were withdrawn using syringe and needle sets, and were consequently used in the LFA. The results of the LFA with the prior concentration step are shown in Fig. 4.4. While no test line appeared for the negative control solution, which did not contain any M13, the intensity of the test line decreased with the decreasing concentration of M13 until the test line was no longer present for the solution containing 10^7 pfu/mL (Fig. 4.4h). This indicated a detection limit of approximately 5×10^7 pfu/mL for the M13 LFA when combined with the prior concentration step, which represented a 10-fold improvement of the detection limit of the LFA assay. Furthermore, the intensity of the test line for all of the detectable concentrations clearly increased when the concentration step was incorporated prior to the detection step. It should be noted that, in this proof-of-concept study, a volume ratio of only 1/9 was utilized to demonstrate the improvement of the concentration step on LFA's detection limit. In the future, even lower volume ratios may be implemented to yield greater concentration factors that can lead to even lower detection limits. Furthermore, while phase separation of an ATPS could be sped up via low-speed centrifugation [157], since the ultimate goal of this approach is to enhance the detection of pathogens at the point-of-care without using any laboratory equipment, other ATPS could instead be utilized and optimized to achieve rapid separation within the time frame of typical LFA diagnostic tests without the need of centrifugation.

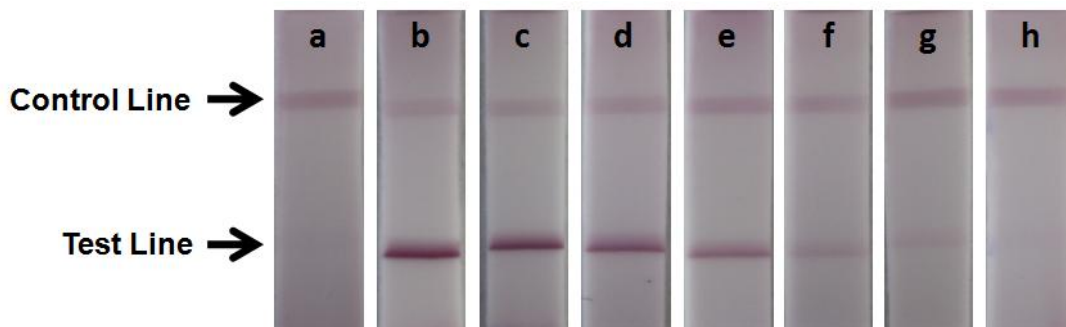


Fig. 4.4. LFA used to detect M13 with the prior concentration step. The negative control without any M13 is shown in panel (a). The remaining solutions initially contained M13 at concentrations of (b) 1×10^{10} , (c) 5×10^9 , (d) 1×10^9 , (e) 5×10^8 , (f) 1×10^8 , (g) 5×10^7 , and (h) 1×10^7 pfu/mL

4.4 Conclusions

Concentrating infectious agents, such as infectious viruses, prior to LFA could significantly increase the effectiveness of using LFA for patient management at the POC. This study demonstrated this approach by the novel combination of an ATPMS with LFA to improve the detection limit of bacteriophage M13. The micellar system was generated using the nonionic surfactant Triton X-114 and PBS. We first compared experimentally measured partition coefficients with our theoretical predictions obtained from a model developed previously for cylindrical biomolecules. The agreement between theory and experiment indicated that the partitioning behavior of M13 in the nonionic micellar system is primarily driven by repulsive, steric, excluded-volume interactions that operate between the micelles and M13 particles, but is limited by the entrainment of micelle-poor, M13-rich domains in the macroscopic, micelle-rich phase. Next, the volume ratio was manipulated to concentrate M13 particles in the top phase. By decreasing the volume ratio from 1 to 1/8, M13 particles were concentrated in the top phase 2- to 7-fold in a predictive manner. After demonstrating that we could concentrate M13 in the ATPMS, we developed an LFA for the detection of M13 in-solution. The detection limit of the

M13 LFA itself was found to be 5×10^8 pfu/mL. M13 was subsequently concentrated approximately 10-fold by utilizing the ATPMS, which led to a 10-fold improvement in the LFA detection limit to 5×10^7 pfu/mL. Therefore, we demonstrated proof-of-principle that concentrating a target virus with ATPS prior to the detection step enhances the detection limit of the LFA, thereby increasing the sensitivity of the immunoassay. In the future, the operating conditions could be manipulated to obtain even lower volume ratios, which in turn should result in obtaining higher concentration factors that yield even lower detection limits. Furthermore, the ATPS utilized could be optimized to achieve rapid phase separation within the time frame of typical LFA diagnostic tests, so that the complete detection assay, including the concentration step, could be completed within an hour. We believe once optimized, the novel approach of utilizing ATPS to concentrate target molecules, such as infectious viruses, prior to the detection step could significantly improve the sensitivity of LFA, which in turn could enhance its effectiveness as a POC solution for preventing pandemic outbreaks.

Chapter 5: Using an aqueous two-phase polymer-salt system to rapidly concentrate viruses for improving the detection limit of the lateral-flow immunoassay

5.1 Motivation and background

The early and rapid detection of viruses at the point-of-need (PON) is crucial for controlling viral pandemics [158]. These concerns are further intensified in the developing world due to the lack of medical equipment and trained personnel [159]. A rapid PON detection assay which can be used in these settings can lead to faster isolation of confirmed cases, reduced hospital stays, and the timely administration of treatments [158, 160, 161]. Such an assay can also protect many military and civilian lives when used to detect biological warfare agents [162].

The lateral-flow immunoassay (LFA) is suitable for PON detection because it does not require power or equipment, is portable and cheap, is easy to use, and produces a faster time-to-result than its laboratory-based competitors [85, 163, 164]. However, in viral applications, the sensitivity of LFA (the percentage of accurately detected positive results) has been shown to be inferior to laboratory-based tests, such as viral culture and real-time polymerase chain reaction (PCR) [129, 130, 158, 160, 165, 166]. One study demonstrated that the reported LFA sensitivities for seasonal H1N1, swine H1N1, and H3N2 influenza were low at values of 63%, 51%, and 31%, respectively, for samples that were confirmed as positive via PCR [165]. Despite the many advantages of LFA for PON detection, its low sensitivity limits its effectiveness in containing outbreaks and the early detection of biological warfare agents.

To improve the sensitivity of LFA, we previously investigated a pre-concentration step which involved a liquid-liquid extraction process [167, 168]. Liquid-liquid extractions are suitable for PON applications, since they are affordable, simple to use, and require little to no

power or laboratory equipment. Liquid-liquid extractions can also be scaled down for small sample sizes and integrated into a portable diagnostic device. In contrast to conventional oil-water two-phase systems that can denature or inactivate biomolecules, we investigated an aqueous two-phase system (ATPS). Because the two phases of the ATPS are predominantly comprised of water, both phases provide a mild environment for the biomolecules [169].

The partitioning behavior of cells, proteins, and viruses in ATPSs have been extensively researched, and it has been found that biomolecule partitioning between the two phases is dependent on the physical and chemical properties of the biomolecule [156, 170-179]. While these studies have focused primarily on the large-scale purification of biomolecules, we have been investigating small-scale diagnostic applications for combination with LFA. We previously studied a micellar ATPS to concentrate the model virus, bacteriophage M13 (M13) [167], and improved the detection limit of LFA using this approach. Although this micellar ATPS met most of the design criteria for a PON device, it was not fast enough as it phase separated on the order of hours.

In order to increase the viability of combining ATPS with LFA in a PON setting, we made the following modifications to our system: (1) investigated a polyethylene glycol (PEG) and potassium phosphate (salt) ATPS with a shorter phase separation time, (2) examined the kinetic behavior of biomolecule partitioning which allowed a significant further reduction in extraction time, (3) ensured compatibility between the gold nanoprobe indicator used for LFA with the salt-rich phase of the PEG-salt ATPS by decorating PEG on the gold surface, and (4) generated a custom MATLAB script to quantify the observed LFA signal intensities. A visual representation summarizing these changes is shown in Figure 5.1.

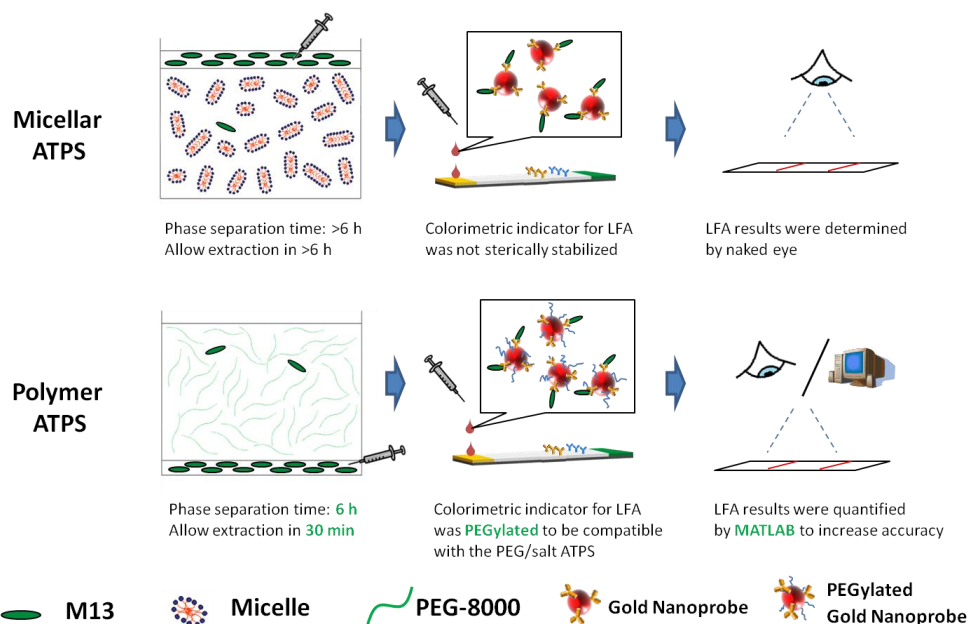


Figure 5.1. Graphical summary of our recent improvements relative to our previous proof-of-concept study.

5.2 Materials and Methods

5.2.1 Culturing Bacteriophage M13

Escherichia coli (*E. coli*) bacteria, strain ER2738 (American Type Culture Collection, ATCC, Manassas, VA), were incubated in 8 mL of Luria broth (Sigma Aldrich, St. Louis, MO) at 37°C in an incubator shaker for 6 h. To culture model virus bacteriophage M13 (ATCC), a small amount of frozen M13 was added to the bacterial culture. The bacterial culture was then placed in an incubator shaker at 37°C for 14 h. The solution was centrifuged at 4°C and 6000 g for 15 min to isolate the M13 in the supernatant from the bacteria in the pellet. The supernatant was extracted from the solution and filtered through a 0.22 µm syringe filter (Millipore, Billerica, MA). Dilutions of this stock M13 solution were calculated using the concentration of M13 as determined by the plaque assay, and therefore, the M13 concentrations are reported in

plaque-forming units per mL (pfu/mL) [180]. All reagents and materials were purchased from Sigma-Aldrich (St. Louis, MO) unless otherwise noted.

5.2.2 Finding Volume Ratios for the PEG-Salt System

For the polymer-salt ATPS, polyethylene glycol 8000 (PEG, VWR, Brisbane, CA) and potassium phosphate (5:1 dibasic:monobasic) were dissolved in Dulbecco's PBS (Invitrogen, Grand Island, NY, pH 7.4, containing 1.47 mM KH_2PO_4 , 8.1 mM Na_2HPO_4 , 137.92 mM NaCl, 2.67 mM KCl, and 0.49 mM MgCl_2). The final solutions were made with a total mass of 5 g containing 2% (w/w) Luria broth to be consistent with the experiments involving M13 samples which contain Luria broth. Equilibrium volume ratios (the volume of the macroscopic top phase divided by the macroscopic bottom phase) were measured after a minimum of 12 h (well past equilibrium) by marking the outside of the tube at the interface and the top of the solution. Tubes were then emptied, dried, and weighed on a scale. Water was added up to the marks, and the volumes of both phases were determined using 1 g/mL as the density of water. The different equilibrium volume ratios were found by varying the initial PEG concentration, initial salt concentration, and holding the temperature constant at 37°C. It should be noted that these volume ratios were selected on the same tie-line to ensure similar partitioning of the biomolecule, and the specific operating conditions that were used are listed in Table 5.1.

Table 5.1. Initial PEG and salt concentrations for various equilibrium volume ratios.

Volume Ratio	PEG-8000 (% w/w)	Potassium Phosphate* (% w/w)
9:1	21.6%	3.83%
6:1	20.6%	4.19%
3:1	18.1%	5.18%
1:1	12.2%	7.50%

*Used in a 5:1 dibasic to monobasic ratio.

5.2.3 Partitioning and Concentrating M13

For each concentration experiment, 4 identical 5 g PEG-salt solutions were prepared. Of these solutions, 3 were used for the concentration step (n=3), while 1 was used as a control to represent the initial M13 concentration. To ensure each solution was in one phase prior to phase separation, all solutions were equilibrated at 4°C and mixed to homogeneity. M13 was then added to the 4 solutions to yield an overall initial concentration of 1×10^8 pfu/mL. To determine how M13 concentration varies with time, 9:1 volume ratio solutions were incubated in a 37°C water bath for 30 min, 1 h, 4 h, and 24 h. To determine how M13 concentration varies with volume ratio, the 9:1, 6:1, 3:1, and 1:1 volume ratio solutions were incubated in a 37°C water bath for 30 min. In each experiment, the bottom phase of 3 of the solutions was carefully withdrawn using a syringe. The control solution underwent the same incubation step to mimic the same conditions as the test solutions. However, after the incubation, the control was once again equilibrated to 4°C and mixed to homogeneity before withdrawing an aliquot to represent the initial concentration of M13 in the ATPS. The M13 concentrations of the extracted bottom phases and the control solution were determined by the plaque assay.

5.2.4 Preparing Gold Nanoprobes

Colloidal gold nanoparticles were initially prepared according to Frens [181]. The diameters of the gold nanoparticles were then determined using dynamic light scattering (DLS) with a Zetasizer Nano SZ particle analyzer (Malvern Instruments Inc., Westborough, MA). Subsequently, the concentration of gold nanoparticles was determined using Beer's Law. The absorbance values used were at the peak absorbance, and the molar extinction coefficients were taken from a data sheet provided by BBInternational Life Sciences (Madison, WI).

Following the quantification of the gold nanoparticles, mouse monoclonal antibodies against M13's coat protein pVIII (Abcam Inc., Cambridge, MA) were added to the nanoparticle solution at a ratio of 16 μg of anti-M13 per 1 mL of colloidal gold to form the gold nanoprobes. The pH of the solution was adjusted to 9.0 using 0.1 M NaOH to promote dative bonds between the antibodies and the gold, and this solution was mixed on a shaker for 30 min. To provide steric colloidal stabilization when adding gold nanoprobes to the PEG-poor, salt-rich phase prior to LFA, PEG-2000-SH (Nanocs, Boston, MA) molecules were bound to the gold nanoprobes at a molar ratio of 5000 PEG-2000-SH molecules to 1 gold nanoprobe. The solution was mixed for an additional 30 min. To prevent nonspecific binding, 100 μL of a 10% bovine serum albumin (BSA) solution was added to 1 mL of the colloidal gold solution to block remaining excess surfaces, and this solution was mixed for 30 min. Finally, the solution was centrifuged at 4°C and 8600 g for 30 min to remove free antibody, PEG, and BSA. The decorated gold nanoprobes were resuspended in 150 μL of 0.1 M sodium borate buffer at pH 9.0.

5.2.5 Combining ATPS with LFA

To combine the ATPS pre-concentration step with LFA, varying M13 concentrations were added to the 9:1 volume ratio PEG-salt solution. After a 30 min incubation at 37°C, the concentrated bottom phase was extracted using a syringe. For consistency between immunoassays performed with and without the pre-concentration step, M13 was added to a bottom phase sample of a 9:1 solution that initially did not contain M13, thus forming the control solutions. Subsequently, 30 μL of the bottom phase samples and 10 μL of the anti-M13 decorated colloidal gold probe solution were mixed together with 30 μL of running buffer. The running buffer solution, which aids the flow of samples through the test strips, consisted of 0.2% w/v BSA, 0.3% w/v Tween 20, 0.2% w/v sodium azide, 0.1% PEG-8000, and 0.1 M Trizma base in ddH₂O with the pH adjusted to 8. To allow antibodies to bind to M13, the resulting solutions were mixed and incubated for 5 min before adding the LFA strip. The LFA strips were assembled to implement the sandwich assay as previously described [167]. After 10 min, the LFA strips were removed and results were obtained by visually examining the test and control lines on the LFA strip.

5.2.6 Analyzing LFA Quantitatively

Pictures of the LFA strips were taken immediately after the tests were complete with a Canon DSLR camera in a controlled lighting environment. To quantify the LFA results, we wrote a custom MATLAB script with an approach similar to that of Yager and coworkers [182]. Cropped images were converted to 8-bit grayscale matrices. Subsequently, the matrix was split in half, with one resulting matrix containing the control line and the other containing the test line. For each half matrix, the minimum intensity (darkest spot) was located along vectors

perpendicular to the control or test line. The mean location of these minima was used as the center of a 15 pixel-high rectangular region, spanning the length of the control or the test line. Subsequently, the mean grayscale intensity of all pixels in the control line region (I_{control}) was calculated. The same procedure was applied to the remaining half of the image containing the test line, yielding the mean grayscale intensity of the test line region (I_{test}). The mean grayscale intensity of a third reference region ($I_{\text{reference}}$), 15 pixels wide and 50 pixels upstream of the test line, was used to normalize the intensities of the test and control lines as follows:

$$\text{Signal}_{\text{control}} \equiv I_{\text{reference}} - I_{\text{control}} \quad (5.1)$$

for the control line, and

$$\text{Signal}_{\text{test}} \equiv I_{\text{reference}} - I_{\text{test}} \quad (5.2)$$

for the test line. Note that high values of intensity correspond to white regions.

5.3 Results and Discussion

5.3.1 Biomolecule Partitioning

Previously, we showed that the Triton X-114 micellar ATPS can be combined with LFA to achieve a 10-fold improvement in the LFA viral detection limit [167]. The Triton X-114 micellar system takes more than 6 h for the volumes of both phases to equilibrate. In contrast, we investigated the polymer-salt ATPS in this study, which phase separates more rapidly, and also used an early extraction time of 30 min for the 9:1 volume ratio.

An aqueous solution composed of salt and PEG, which is a polymer that significantly participates in hydrogen bonding interactions, will undergo macroscopic phase separation. A PEG-rich, salt-poor phase will form on top, while a PEG-poor, salt-rich phase will form on

bottom [183]. Large, hydrophilic biomolecules have previously been shown to partition extremely into the bottom, PEG-poor phase [184, 185]. For our studies, we investigated bacteriophage M13, a model virus similar in size and shape to the Ebola and Marburg viruses. Since M13 has a length of 900 nm [186] and a relatively hydrophilic protein shell [187], we expected it to partition extremely into the bottom, PEG-poor phase due to experiencing fewer repulsive, steric, excluded-volume interactions with the PEG polymers in that phase relative to those in the PEG-rich phase. Note that, in the aqueous two-phase micellar system, we observed M13 to partition extremely into the macroscopic micelle-poor phase where the M13 viral particles also experienced fewer excluded-volume interactions [167].

When the solution is heated and phase separation first begins, PEG-rich (M13-poor) domains and PEG-poor (M13-rich) domains form throughout the entire solution. The viral concentrations in these microscopic domains are assumed to reach their equilibrium values very quickly [176], and like-domains begin to coalesce with each other. As these domains grow larger, their difference in density generates uneven gravitational and buoyant forces which cause the PEG-rich domains to rise and the PEG-poor domains to sink. This results in the formation of the macroscopic top, PEG-rich (M13-poor) phase and the macroscopic bottom, PEG-poor (M13-rich) phase. The kinetics of this process and the effects of entrained, or trapped, domains are further explained below.

Since the viruses are expected to partition extremely into the macroscopic bottom phase, we are only interested in the biomolecule concentration in the bottom phase at the time of extraction. The concentration factor is then defined as the concentration of virus in the macroscopic bottom phase, $C_{\text{virus,bottom}}$, divided by the initial overall concentration, $C_{\text{virus,initial}}$.

$$\text{Concentration Factor} \equiv \frac{C_{\text{virus,bottom}}}{C_{\text{virus,initial}}} \quad (5.3)$$

One potential concern that could negatively affect the concentration factor is the presence of PEG-rich (M13-poor) domains entrained in the macroscopic bottom phase. Prior to equilibrium, not all of the domains have had enough time to travel to their respective macroscopic phases. However, this is not an issue when using the equilibrium volume ratio of 9:1. Due to the greater volume associated with the PEG-rich domains in the 9:1 volume ratio, it is easier for them to coalesce and form a continuous phase. The PEG-rich domains also have a smaller distance to travel in order to reach the macroscopic top phase because the macroscopic bottom phase is very small. As a result, there is minimal entrainment of PEG-rich (M13-poor) domains in the macroscopic bottom phase, and the concentration of the biomolecule is expected to be close to its equilibrium value. It should be noted, however, that entrainment of PEG-poor (M13-rich) domains is still expected in the macroscopic top phase. Due to the smaller volume associated with the PEG-poor domains, it is more difficult for these domains to coalesce. They also have to travel a further distance through a more viscous PEG-rich macroscopic phase to reach the macroscopic bottom phase. However, because we are only concerned with the biomolecule concentration in the bottom phase and only require small volumes for LFA, it is possible to extract at 30 min and still achieve our equilibrium predicted concentration factors.

We visually examined the phase separation of the 9:1 volume ratio solution as a function of time. Initially, PEG-rich and PEG-poor domains form throughout the entire solution. The PEG-rich domains quickly coalesce and form the continuous phase. The solution appears turbid because the entrained PEG-poor domains cause light to scatter (Fig. 5.3A). As PEG-poor domains coalesce and sink to the bottom due to their greater density, the macroscopic bottom,

PEG-poor phase forms from the bottom upwards. After 30 min, there is a turbid macroscopic top, PEG-rich phase that is separated from the clear macroscopic bottom, PEG-poor phase (Fig. 5.3B). Although the top phase contains entrained PEG-poor (M13-rich) domains at this time, we are only interested in the turbidity of the bottom phase since it contains our concentrated biomolecule. After a long period of time, all, or most, of the PEG-poor domains have traveled to the bottom, macroscopic phase, and the system is near equilibrium as indicated by the two clear phases (Fig. 5.3C). Note that the bottom phase at 30 min is already clear, due to the absence of significant entrained PEG-rich (M13-poor) domains, suggesting that the measured concentration of virus in that phase should already reflect its equilibrium value.

In order to extract the bottom phase at 30 min, we wanted to confirm that the macroscopic bottom, PEG-poor (M13-rich) phase did not contain significant PEG-rich (M13-poor) domains. The concentration factor was therefore determined as a function of time to indicate that the measured concentration of M13 in the bottom phase was equal to its equilibrium value even after a short period of time. Specifically, we ran M13 partitioning experiments using the same temperature and initial PEG and salt concentrations as those used in Figure 5.3 (*i.e.*, those conditions which yielded a 9:1 equilibrium volume ratio), and extracted the bottom phase at 30 min, 1 h, 4 h, and 24 h (well past equilibrium). As shown in Figure 5.4, the concentration factor remained constant as a function of extraction time between 30 min and 24 h, demonstrating that the entrainment of PEG-rich (M13-poor) domains in the macroscopic bottom, PEG-poor (M13-rich) phase is indeed minimal. Therefore, for all of our subsequent studies, we used the 30 min extraction time as short times are necessary for PON applications.

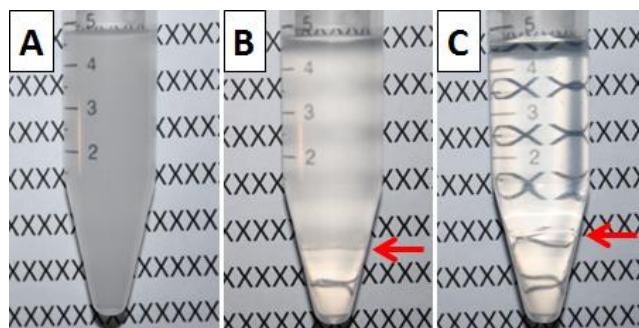


Figure 5.3. The aqueous two-phase PEG-salt system after incubation in a 37°C water bath for (A) 10 min, (B) 30 min, and (C) 24 h. The white paper was filled with the letter “X” to help visualize the turbidity of each phase. The arrows denote the location of the macroscopic interface.

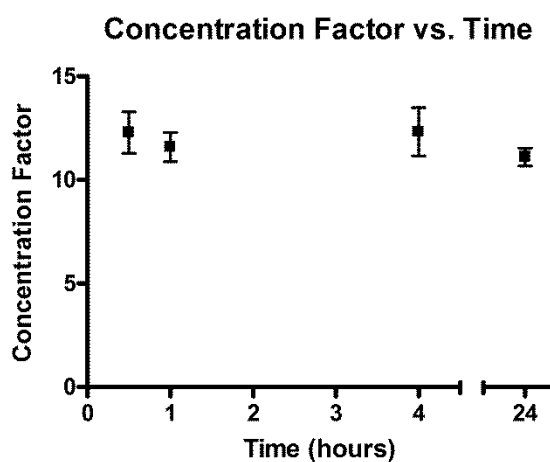


Figure 5.4. Experimentally determined concentration factors at various time points. Error bars represent standard deviations from triplicate measurements.

5.3.2 Partitioning M13 in ATPS

The concentration factor in Equation (5.3) can be shown to be a function of the volume ratio. Using a mole balance to equate the initial moles of virus in the single homogeneous phase with the sum of the moles of virus in the two resulting phases, we obtain the following expression:

$$C_{\text{virus,initial}} V_{\text{total}} = C_{\text{virus,top}} V_{\text{top}} + C_{\text{virus,bottom}} V_{\text{bottom}} \quad (5.4)$$

where $C_{\text{virus,top}}$ is the concentration of virus in the macroscopic top phase, and V_{top} and V_{bottom} are the volumes of the top and bottom phases, respectively. Rearranging Equation (5.4) yields the following expression for the concentration factor:

$$\text{Concentration Factor} = \frac{1 + \frac{V_{\text{bottom}}}{V_{\text{top}}}}{\frac{C_{\text{virus,top}}}{C_{\text{virus,bottom}}} + \frac{V_{\text{bottom}}}{V_{\text{top}}}} \quad (5.5)$$

Using the 9:1 volume ratio ATPS, we measured the M13 partition coefficient (the equilibrium concentration in the top phase divided by the equilibrium concentration in the bottom phase) to be less than 0.0001. Since this measured partition coefficient is much less than the $V_{\text{bottom}}/V_{\text{top}}$ value of 1/9, this expression can be approximated as follows:

$$\text{Concentration Factor} \approx 1 + \frac{V_{\text{top}}}{V_{\text{bottom}}} \quad (5.6)$$

Accordingly, a linear relationship is predicted for the concentration factor as a function of the volume ratio. It makes sense for the concentration factor to increase with increasing volume ratio because the biomolecule partitions extremely into the bottom phase, and increasing the volume ratio corresponds to shrinking the phase where M13 extremely partitions into.

Specifically, if a 9:1 volume ratio is used, we expect M13 would be concentrated by 10-fold, since the volume of the phase that M13 partitions extremely into is 1/10 of the initial volume.

Subsequently, we wanted to test this prediction using our 30 min extraction time, since short times are necessary for PON applications. We ran M13 partitioning experiments at 37°C and with initial concentrations of PEG and salt that yielded the 9:1, 6:1, 3:1, and 1:1 equilibrium volume ratios. Figure 5.5 shows the results of our experiments which tested concentration factor as a function of volume ratio. To statistically determine if our experimental data agreed with our

model predictions, the coefficient of determination, or R-squared value, was calculated. The R-squared value was found to be 0.858, suggesting that our experimental data agrees reasonably well with our predicted values, further confirming that the simple model is appropriate even for the 30 min extraction time.

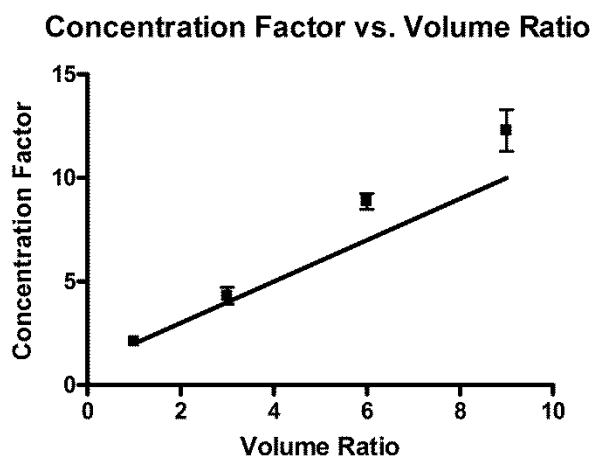


Figure 5.5. Experimentally determined concentration factors at various volume ratios. The symbols correspond to the experimental data, and the error bars represent standard deviations from triplicate measurements. The solid line corresponds to the predictions from Equation (5.6).

5.3.3 Detecting M13 via LFA

After demonstrating that M13 could be concentrated in 30 min via an ATPS, we prepared colloidal gold probes and LFA strips. PEG decorated on the surface of the gold probes provided steric stability and prevented aggregation of gold probes in the environment of the extracted salt-rich phase. Figure 5.6 shows the results of LFA with samples that did not experience the pre-concentration step. M13 concentrations were selected at equally spaced points along the logarithmic scale. The presence of the control line or the upper band, which contains polyclonal anti-IgG antibody, indicates a valid test as it confirms that the sample has flowed through the entire strip. The presence of the test line or lower band, which contains the antibody to M13's

coat protein pVIII, indicates the presence of M13. The negative control, as shown in Figure 5.6A, contained no M13, and there is no visible test line as expected. Of the remaining panels, the intensity of the test line is greatest for the highest M13 concentration shown in Figure 5.6B, and line intensity decreases with decreasing M13 concentration. The test line is no longer visible at 3.2×10^8 pfu/mL (Fig. 4.6E), indicating a detection limit of approximately 1×10^9 pfu/mL (Fig. 5.6D).

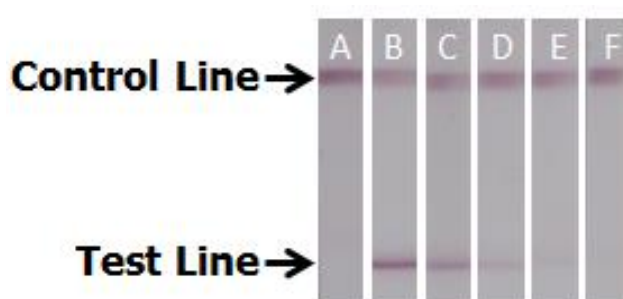


Figure 5.6. LFA for detecting M13 without a prior concentration step. Panel (A) shows the negative control in which no M13 was added. The remaining solutions contained M13 at concentrations of (B) 1×10^{10} , (C) 3.2×10^9 , (D) 1×10^9 , (E) 3.2×10^8 , and (F) 1×10^8 pfu/mL.

5.3.4 Concentrating M13 prior to LFA

With the detection limit established at 1×10^9 pfu/mL, we then investigated the possible improvement of the detection limit by utilizing our ATPS. We used the 9:1 volume ratio solution, which was predicted to yield an approximately 10-fold concentration factor based on Equation (5.6). Following a 30 min incubation at 37°C , the bottom phase was extracted, and the samples were prepared for LFA. Figure 5.7 shows the results of the LFA with the pre-concentration step. Again, a test line is absent for the negative control, which contains no M13 (Fig. 5.7A). Of the remaining panels, the initial M13 concentrations are 10-fold less than those shown in Figure 5.6, but the LFA test line intensities match those of the samples without the pre-concentration step. The test line intensity decreases with decreasing M13 concentration until it is

no longer visible at 3.2×10^7 pfu/mL (Fig. 5.7E), indicating a detection limit of approximately 1×10^8 pfu/mL (Fig. 5.7D). This indicated a 10-fold improvement in the detection limit when the ATPS concentration step was applied.

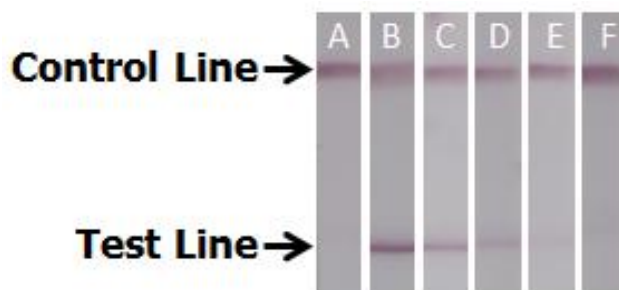


Figure 5.7. LFA for detecting M13 with the prior concentration step. Panel (A) shows the negative control in which no M13 was added. The remaining solutions initially contained M13 at concentrations of (B) 1×10^9 , (C) 3.2×10^8 , (D) 1×10^8 , (E) 3.2×10^7 , and (F) 1×10^7 pfu/mL.

To confirm the conclusions from our visual interpretation of the LFA strips, we converted our LFA images to grayscale and examined the test line intensity against the background using our custom MATLAB script. The results are shown in Figure 5.8 with and without the ATPS concentration step. Note that the two curves are separated by a 10-fold difference in initial M13 concentration for approximately the same test line signal, further confirming our 10-fold concentration improvement.

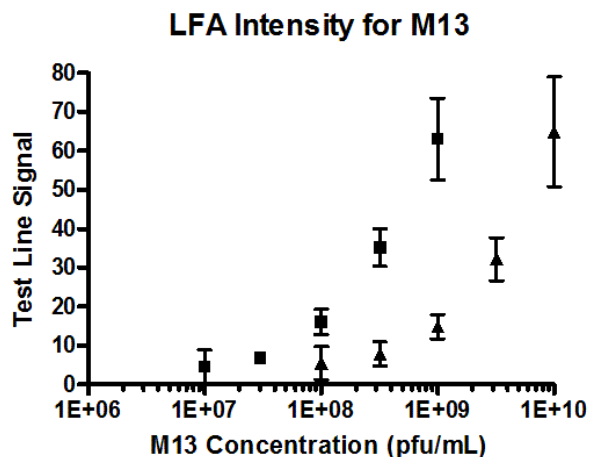


Figure 5.8. LFA signal intensity for M13 with (■) and without (▲) the prior concentration step. Error bars represent standard deviations from at least three measurements.

5.4 Conclusions

The addition of a concentration step prior to LFA could significantly improve the viral detection limit of LFA, and the studies summarized in this chapter extended our previous proof-of-concept investigation which used the micellar ATPS. In this recent work, we investigated a more rapid polymer-salt ATPS which allowed us to dramatically accelerate the concentration step. We first investigated the effects of entrainment, and visually observed no PEG-rich (M13-poor) domains in the macroscopic PEG-poor (M13-rich) phase even after short time periods. We also demonstrated that the concentration factor for M13 in the macroscopic PEG-poor (M13-rich) phase did not change between 30 min and 24 h. Accordingly, since LFA can be performed in ~10 min, the combined approach of using ATPS and LFA can be performed in under 45 min, greatly increasing the potential for its use in a PON device. It should also be noted that the use of a centrifuge could further decrease the macroscopic phase separation time, but this would defeat the purpose of developing an inexpensive and portable device. Using volume ratios

between 1:1 and 9:1 and a 30 min extraction time period, M13 was concentrated between approximately 2- and 10-fold, agreeing reasonably well with our predictions. After forming gold nanoprobe decorated with PEG for steric colloidal stabilization in the extracted PEG-poor, salt-rich phase, we demonstrated that using a 9:1 volume ratio in a prior ATPS step concentrated M13 by 10-fold, which, in turn, led to a 10-fold improvement in the LFA detection limit. This visual observation of the LFA strips was further confirmed by the conversion of the test line signals to grayscale units. In the future, greater concentration-fold improvements could be achieved by manipulating the operating conditions to obtain more extreme volume ratios. Moreover, a simple device that can provide temperature control and that can simultaneously combine ATPS and LFA will be investigated. Such a novel device has much potential for use in PON applications.

Chapter 6: Dextran-coated gold nanoprobcs for the concentration and detection of protein biomarkers

6.1 Motivation and background

Gold nanoparticles have been used in a wide range of biomedical applications, such as detection assays for biomolecules [64, 65, 188, 189] and drug delivery vehicles for cancer treatment [190-192]. They are particularly useful as colorimetric indicators since their optical properties can be adjusted by fine-tuning the physical and chemical properties of the nanoparticles. Bioconjugation of antibodies, polymeric linkers, or other biomolecules is also achieved relatively simply through the formation of dative bonds with the nanoparticle surface [193]. Overall, gold nanoparticles provide a low-cost, increasingly versatile platform for engineering biomedical technologies.

The citrate reduction method is commonly used to synthesize citrate-capped gold nanoparticles that are stabilized through electrostatic repulsions [194]. However, this stabilization can be compromised in the presence of other ions that can screen the surface charges and/or molecules that can bind nonspecifically to the nanoparticles. Therefore, gold nanoparticles are often coated with sterically stabilizing molecules, such as polyethylene glycol (PEG) [191, 194]. In recent years, the polysaccharide dextran has also been explored as an alternative coating material. Dextran can act as both a reducing agent and a sterically stabilizing molecule [192, 195], thus simplifying the process of forming stable gold nanoparticles.

In this study, the properties of dextran were utilized to develop a dextran-coated gold nanoprobe (DGNP), which serves as the centerpiece of an effective diagnostic assay for protein

biomarkers. The DGNP consists of a dextran-coated gold nanoparticle decorated with antibodies specific to the protein of interest. The diagnostic assay combines a detection step that utilizes the lateral-flow immunoassay (LFA) and a pre-concentration step that utilizes aqueous two-phase systems (ATPSs). Due to its low cost, rapid detection, and ease of use, LFA is commonly used in point-of-care and home-use devices for detecting pregnancy and substance abuse [196]. One drawback to LFA, however, is that its sensitivity is lower than that of other laboratory-based assays, which are not appropriate for point-of-care tests in resource-poor settings due to equipment and power requirements.

To improve the sensitivity of LFA, we utilized a polymer-salt ATPS, specifically one comprised of PEG and potassium phosphate (salt), to first concentrate the protein biomarkers prior to the detection step. Since an ATPS is used in a liquid-liquid extraction procedure, it can be scaled down to accompany portable assays like LFA. While proteins tend to partition evenly between the two phases of an ATPS [170, 197-200], we found that DGNPs partition extremely into the PEG-poor, salt-rich phase due to their larger size and dextran's hydrophilicity. We therefore used DGNPs to first capture the proteins in the ATPS and then partition preferentially into the PEG-poor phase. This can effectively “fish” the proteins into the same phase as the DGNPs and concentrate the proteins into a smaller volume. These protein-DGNP complexes can then be extracted and used directly in the subsequent LFA detection step.

In our previous proof-of-concept studies, we were able to concentrate gold nanoparticles in a micellar-based ATPS and improve LFA performance in detecting a model virus [201] and a model protein [202] by 10-fold. However, the micellar-based ATPS phase separates on the order of hours, and the operating temperature must be controlled more tightly. In this study, our PEG-

salt ATPS was able to phase separate at room temperature and also enabled gold nanoparticle extraction from the ATPS within 30 minutes. However, the higher salt concentration in our ATPS compared to the micellar ATPS prohibits the use of the gold nanoparticles from our previous studies. Therefore, we coated the gold nanoparticles with dextran in order to achieve both stability in the salt-rich environment of the PEG-poor phase and the desired partitioning behavior in our PEG-salt ATPS. While we recognized that coating the gold nanoparticles with PEG was also an option, we discovered that PEG-coated nanoparticles did not partition extremely into one phase in our ATPS. Therefore, our novel combination of DGNPs and a PEG-salt ATPS essentially displays four advantageous features (Fig. 6.1): the dextran coating can provide steric stability; the decorated antibodies can capture proteins in solution; the protein-DGNP complex can partition extremely into one phase in the PEG-salt ATPS; and the gold nanoparticles can be directly used as the colorimetric indicator for LFA. To our knowledge, although dextran-coated gold nanoparticles have been used in other applications [192, 195, 203-205], this study is the first to investigate the use of dextran-coated gold nanoparticles in LFA.

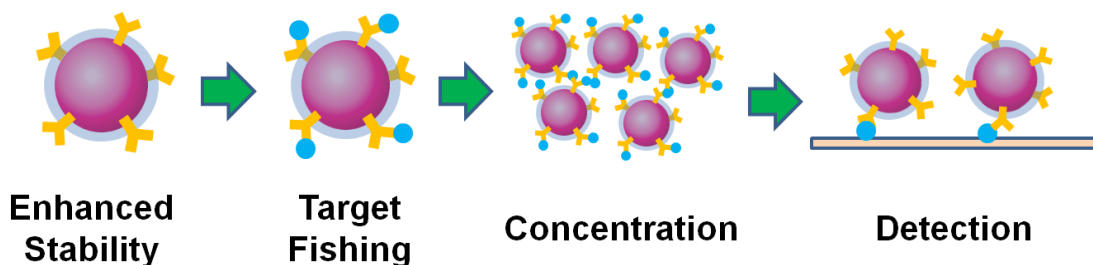


Figure 6.1. Schematic of dextran-coated gold nanoprobe and their roles in our approach to improve the detection limit of LFA using ATPS.

In this study, the stability of dextran-coated gold nanoparticles was compared to the traditional citrate-capped gold nanoparticles and the commonly used PEG-coated gold

nanoparticles. The phase separation behavior of our PEG-salt ATPS was optimized to enable rapid extraction of the DGNPs at room temperature. The partitioning behavior of the DGNPs was subsequently investigated in the PEG-salt ATPS. Transferrin (Tf), which is a common serum protein for iron transport, was chosen as our model protein biomarker due to our experience in working with Tf and its antibody [202]. The detection limit of LFA for Tf was then determined with and without the pre-concentration ATPS step using DGNPs. Qualitative results of LFA were interpreted visually, and computer image analysis was also performed for further quantitative verification of the LFA results.

6.2 Materials and Methods

6.2.1 Preparing Citrate-Capped Gold Nanoparticles

All reagents and materials were purchased from Sigma-Aldrich (St. Louis, MO) unless noted otherwise. Traditional citrate-capped, or naked, gold nanoparticles were prepared according to Frens [181]. Briefly, 10 mL of ddH₂O was heated to 100°C while stirring. As the heated solution started to boil, 100 µL of a 1% w/v gold(III) chloride solution was added. The solution was stirred and boiled for 1 min, after which 25 µL of a 6% w/v sodium citrate solution was added. The solution quickly changed from a dark-purple to a clear, dark cherry color, after which it was cooled to room temperature and stored at 4°C.

6.2.2 Preparing Polyethylene Glycol-Coated Gold Nanoparticles

Before preparing PEG-coated (PEGylated) gold nanoparticles, the concentration of the previously prepared naked gold nanoparticle solution was determined. This concentration, which is used to determine the amount of PEG required for any given PEG:gold nanoparticle molar ratio, was calculated using Beer's Law, with a path length of 1 cm:

$$C = \frac{A}{\epsilon l} \quad (6.1)$$

where C is the concentration of the gold nanoparticles in molarity units, A is the peak absorbance value of the gold nanoparticle, ϵ is the molar extinction coefficient in $M^{-1}cm^{-1}$, and l is the path length in cm. To determine the ϵ value, the diameter of the nanoparticles was first quantified by dynamic light scattering (DLS) using a Zetasizer Nano ZS particle analyzer (Malvern Instruments Inc, Westborough, Massachusetts). The molar extinction coefficient was then read from a data sheet provided by BBInternational Life Sciences (Madison, WI), which correlated the ϵ value with the diameter of the gold nanoparticle. The peak absorbance value of the gold nanoparticles was then quantified using a UV-visible spectrophotometer (Thermo Fisher Scientific, Madison, Wisconsin), and the concentration was determined with Eq. (6.1).

Methoxy-polyethylene glycol (PEG)-thiol (MW 5000, Nanocs Inc., New York, NY) was used to decorate the gold nanoparticle surface with a layer of PEG. Briefly, 5 mL of the naked gold nanoparticle solution was first adjusted to pH 9.0 using a 1 N NaOH solution. The methoxy-PEG-thiol was added to the particle solution at a 50,000:1 PEG:nanoparticle molar ratio to ensure that the gold nanoparticle surface would be thoroughly coated. The mixture was then allowed to react for 30 min at room temperature to allow the thiol groups on the PEG to

form dative bonds with the gold nanoparticles. Free PEG was removed by centrifugation at 9000 g for 30 min. The resulting PEGylated gold nanoparticles were resuspended in 500 μ L of ddH₂O.

6.2.3 Preparing Dextran-Coated Gold Nanoparticles

Dextran-coated gold nanoparticles were prepared according to Min and coworkers with slight modifications [192]. In this protocol, 12 g of dextran (MW 15,000 – 25,000) were dissolved in 160 mL of UltraPure sterile water (Rockland Immunochemicals Inc., Gilbertsville, PA), and the solution was heated to 100°C while stirring. As the heated solution started to boil, 2.16 mL of a 1% w/v gold(III) chloride solution was added. The solution was stirred and boiled for 20 min until the color of the solution turned violet. The solution was then cooled to room temperature and stored at 4°C. Excess dextran was subsequently removed by centrifugation at 9000 g for 30 min.

6.2.4 Determining the Critical Coagulation Concentration of Gold Nanoparticles

The naked (*i.e.*, citrate-capped), PEGylated, and dextran-coated gold nanoparticle solutions were mixed separately with various concentrations of a stock potassium phosphate solution. The mixed solutions were incubated at room temperature for 30 min. The absorbance spectrum of each sample was determined using a UV-visible spectrophotometer. As established by other researchers, the critical coagulation concentration (CCC) was identified as the salt concentration at which the absorbance spectrum of the GNP solution near the peak absorbance wavelength decreases significantly in intensity [194].

6.2.5 Preparing Polyethylene Glycol-Potassium Phosphate Aqueous Two-Phase Systems

A stock potassium phosphate solution (5:1 dibasic:monobasic) was prepared in Dulbecco's phosphate-buffered saline (PBS) (Invitrogen, pH 7.4, containing 1.47 mM KH_2PO_4 , 8.10 mM Na_2HPO_4 , 138 mM NaCl, 2.67 mM KCl and 0.495 mM MgCl_2). Subsequently, a stock polyethylene glycol (MW 8000, VWR, Brisbane, CA) solution was prepared in PBS. Using the stock solutions, a 2 mL PEG-salt ATPS solution in PBS was prepared at specific concentrations of PEG and salt that yielded a PEG-rich (salt-poor):PEG-poor (salt-rich) volume ratio of 9:1. This volume ratio was measured after incubating the ATPS solutions at room temperature for a minimum of 12 h.

6.2.6 Radiolabeling Anti-Tf Antibody

Iodine-125 (^{125}I) was used to radiolabel the tyrosine residues of the goat anti-Tf antibody (Bethyl Laboratories, Montgomery, TX). Briefly, Na^{125}I (MP Biomedicals, Irvine, CA) was activated by IODO-BEADS (Pierce Biotechnology, Rockford, IL). Subsequently, the activated ^{125}I was reacted with goat anti-Tf antibody for 15 min. The radiolabeled antibodies were purified from free ^{125}I using a Sephadex G15 size-exclusion column. The specific activity and concentration of the radiolabeled antibodies was determined by a phosphotungstic acid assay.

6.2.7 Preparation of Dextran-Coated Gold Nanoprob

To prepare the dextran-coated gold nanoprob (DGNPs), 10 mL of the previously prepared dextran-coated gold nanoparticle solution was first adjusted to pH 9.0 using 1 N NaOH. Subsequently, 80 μg of goat anti-Tf antibody was added to the dextran-coated gold nanoparticle solution. The mixture was then allowed to react for 30 min at room temperature to allow the

antibodies to form dative bonds with the particles. Free unbound antibodies were removed by centrifugation at 9000 g for 30 min. The recovered DGNPs were further washed with a 1% bovine serum albumin (BSA) solution so that the BSA could cover any free surfaces on the DGNPs to prevent nonspecific binding. Excess BSA and additional unbound antibodies were removed by centrifugation at 9000 g for 30 min. The recovered DGNPs were resuspended in 1 mL of a 0.1 M sodium borate buffer (pH 9.0).

6.2.8 Partitioning Dextran-Coated Gold Nanoprobes

To study the partitioning behavior of the DGNPs in the PEG-salt ATPS, the concentration of DGNPs in each phase of the ATPS solution was quantified. Radiolabeled DGNPs were prepared by conjugating radiolabeled goat anti-Tf antibodies onto the dextran-coated gold nanoparticles using the same procedure as described in the previous section. For each partitioning experiment, 200 μ L of the radiolabeled DGNP solution was added to three identical PEG-salt ATPS solutions in PBS, each with a final volume of 2 mL. The mixtures were incubated for 30 min, 2 h, 4 h, and 12 h at 25°C. The PEG-rich, salt-poor top phases and the PEG-poor, salt-rich bottom phases were carefully extracted, and the volumes of each phase were measured. The amounts of radiolabeled DGNPs in each phase were quantified by measuring the radioactivity of the radiolabeled antibodies conjugated to the DGNPs using a Cobra Series Auto-Gamma Counter.

6.2.9 Preparing LFA Test Strips

A competition LFA was utilized in this study. First, the Tf proteins were immobilized on a nitrocellulose membrane to form the test line. Secondary anti-IgG antibodies, which can bind to the primary antibodies on the DGNPs, were also immobilized downstream of the immobilized Tf proteins to form the control line. If Tf proteins were not present in the sample solution, then the DGNPs would bind to the Tf printed on the strip, forming a visible band at the test line. On the other hand, if Tf proteins were present in the sample, then they would first bind to their specific antibodies on the surfaces of the DGNPs. If the DGNPs were saturated with Tf proteins, then the DGNPs would bypass the Tf printed on the strip, resulting in the absence of a visible band at the test line. Excess DGNPs would still bind to the control line, indicating that the fluid indeed flowed through the strip and that the result is valid. In summary, a negative test was indicated by two visible bands, with one at the test line and one at the control line, while a positive test was indicated by only one visible band at the control line.

6.2.10 Detecting Tf Using LFA

LFA without the PEG-salt ATPS pre-concentration step was performed before combining with the ATPS. In this study, PBS solutions containing varying concentrations of Tf were prepared, and each Tf concentration was tested in triplicate. For each LFA strip, 10 μ L of the corresponding Tf solution was mixed with 10 μ L of the DGNP solution and 30 μ L of the test buffer (0.2% BSA, 0.3% Tween20, 0.2% sodium azide, 0.1% polyethylene glycol, 0.1M Trizma base, pH 8), which was used to assist the flow of the samples through the test strips. LFA test strips were dipped vertically into each mixture so that the sample pads came in contact with the

mixtures. The strips were taken out of the mixtures after 10 min, and the results were read visually and quantified using MATLAB.

6.2.11 Combining Dextran-Coated Gold Nanoprobles, ATPS, and LFA to Detect Tf

LFA with the PEG-salt ATPS pre-concentration step was subsequently performed. In these experiments, ATPS solutions containing varying Tf concentrations were first prepared, and each Tf concentration was tested in triplicate. Since the volume of the bottom phase was approximately 200 μL , 100 μL of the DGNP solution was added to the Tf/ATPS solution with a final volume of 2 mL to achieve a similar DGNP concentration as the LFA tests performed without the ATPS step. The ATPS solutions were well mixed and incubated for 30 min at 25°C. For each mixture, 20 μL of the PEG-poor bottom phase was extracted and mixed with 30 μL of test buffer to match the volumes used in the study without the ATPS step. LFA test strips were dipped vertically so that the sample pads came in contact with the mixtures. The strips were taken out of the mixtures after 10 min, and the results were read visually and quantified using MATLAB.

6.2.12 LFA Quantification

A custom MATLAB script with an approach similar to Yager and coworkers [206] was written to quantitatively analyze the resulting images. Immediately after the LFA tests were completed, images of the test strips were taken using a Canon EOS 1000D camera (Canon U.S.A., Inc., Lake Success, NY). To ensure consistency among the images, the lighting was

controlled and each strip was oriented in the same way. These images were cropped and converted to an 8-bit grayscale matrix. The intensity was averaged along the axis perpendicular to the flow and parallel to the test and control lines, and a one-dimensional intensity map was generated. The two maxima were identified as the control and test lines, and the distance between these two lines was calibrated using the negative controls (which have strong test and control lines).

To obtain the test line intensity from the set of sample data, the location of the control line was identified, and the test line location was determined using the previously calibrated distance. The test line region was set as a 15 pixel-wide region centered at this test line location. The baseline for this measurement was then determined by averaging the signal from two 25 pixel-wide regions located on both sides of the test line. The first baseline region began 25 pixels upstream of the test line location and continued 25 pixels upstream, while the other began 25 pixels downstream of the test line location and continued 25 pixels downstream. The test line intensity was then calculated as the area under the curve of the test line region to capture the effects of all DGNPs that were bound to the test line.

6.3 Results

6.3.1 Determining the Critical Coagulation Concentration of Gold Nanoparticles

The CCC values of the naked, PEGylated, and dextran-coated gold nanoparticle samples were measured to determine whether the dextran coating provides the necessary steric stability for the gold nanoparticles in our PEG-salt ATPS solutions. We discovered that the peak absorbance wavelength for the absorbance spectrum of the gold nanoparticles was approximately

535 nm. Therefore, the absorbance spectrum near 535 nm for each type of gold nanoparticle was observed across a range of potassium phosphate concentrations, since potassium phosphate is the salt component of our PEG-salt ATPS. The results are shown in Fig 6.2. For each plot, the peak absorbance value was assigned a value of 1.0 (or 100% normalized absorbance), and the remaining absorbance values of that plot were adjusted accordingly. From these plots, it was determined that the CCC of the naked gold nanoparticle was between 0.3 and 0.4% w/w potassium phosphate; the CCC of the PEGylated gold nanoparticle was between 7.5 and 10% w/w potassium phosphate; and the CCC of the dextran-coated gold nanoparticle was greater than 30% w/w potassium phosphate. These results indicated that the dextran-coated gold nanoparticles were more stable than even the PEGylated gold nanoparticles in potassium phosphate salt solutions. Moreover, since 30% w/w potassium phosphate is greater than the bottom phase potassium phosphate concentration (~10% w/w), the dextran-coated gold nanoparticles were expected to remain stable and functional in our PEG-salt ATPS solution. This was confirmed with their successful use in the studies described below.

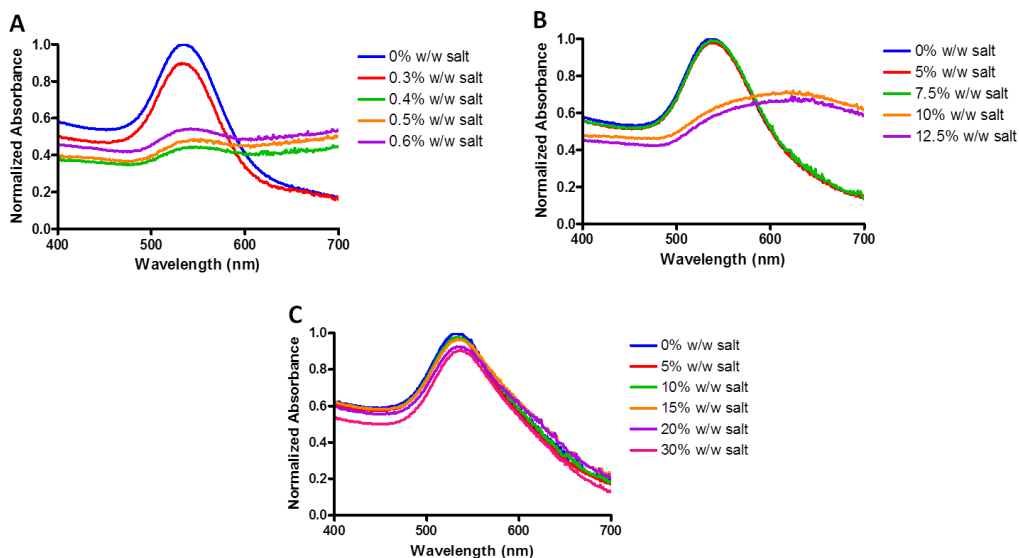


Fig. 6.2. Normalized visible light range absorbance spectra (400 to 700 nm) of (A) citrate-capped or naked gold nanoparticles, (B) PEGylated gold nanoparticles, and (C) dextran-coated gold nanoparticles at varying % w/w potassium phosphate solutions

6.3.2 Partitioning Behavior of Dextran-Coated Nanoprobos

The partitioning behavior of the radiolabeled DGNPs was first observed visually in the PEG-salt APTS solution with a 9:1 PEG-rich:PEG-poor volume ratio. Initially, the PEG-salt APTS solution containing DGNPs appeared opaque and light purple (Fig. 6.3a). A bottom phase that was a dark purple color then appeared, indicating that the DGNPs partitioned extremely into the PEG-poor bottom phase (Fig. 6.3b). Over time, the bottom phase grew in volume as the DGNP-rich, PEG-poor domains moved to the bottom of the APTS solution. In contrast, it was found that the DGNPs displayed minimal partitioning into the top, PEG-rich phase as the top phase had very little purple color. After a 12 h equilibrium time, the volumes of the top and bottom phases no longer changed and the top phase appeared clear, suggesting that all of the DGNP-rich, PEG-poor domains reached the bottom of the APTS solution (Fig. 6.3c). It should be noted that, after approximately 30 min, the color intensity of the bottom phase did not change over time, suggesting that the DGNP concentration in the bottom phase remained relatively constant from 30 min to 12 h.

The partitioning behavior of the radiolabeled DGNPs between the two phases was then quantified by the partition coefficient (K_{DGNP}) defined below:

$$K_{DGNP} \equiv \frac{C_{DGNP,top}}{C_{DGNP,bottom}} \quad (6.2)$$

where $C_{DGNP,top}$ and $C_{DGNP,bottom}$ are the concentrations of DGNPs in the top and bottom phase, respectively. The K_{DGNP} value was measured to be 0.00605 ± 0.00010 , which was consistent

with the idea that the relatively large DGNPs should partition extremely into the PEG-poor bottom phase.

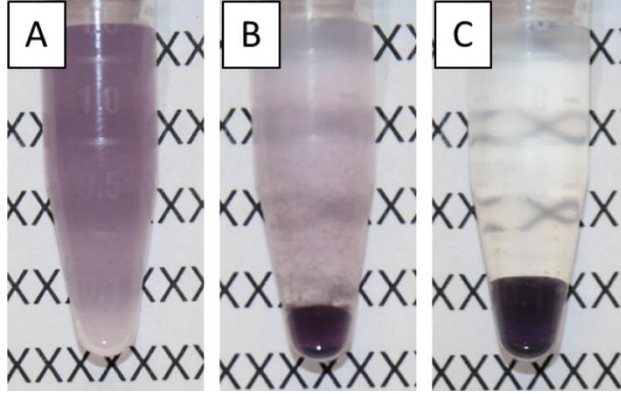


Fig. 6.3. Partitioning behavior of DGNPs in our PEG-salt APTS at (A) 0 min, (B) 30 min, and (C) 12 h

6.3.3 Pre-Equilibrium Extraction of Dextran-Coated Nanoprobes

To demonstrate that the DGNPs could be concentrated in our PEG-salt APTS in a predictive manner, we measured the concentration factor, or the concentration-fold improvement of the DGNPs, in the 9:1 PEG-salt APTS solution. The concentration factor is defined as the concentration of DGNP in the bottom phase, $C_{DGNP,bottom}$, divided by the initial DGNP concentration, $C_{DGNP,initial}$.

$$\text{Concentration Factor} \equiv \frac{C_{DGNP,bottom}}{C_{DGNP,initial}} \quad (6.3)$$

An expression for the concentration factor can be derived by beginning with the mole balance equation for the DGNPs in the APTS solution:

$$C_{DGNP,initial}V_{total} = C_{DGNP,top}V_{top} + C_{DGNP,bottom}V_{bottom} \quad (6.4)$$

where V_{top} and V_{bottom} are the volumes of the top and bottom phases, respectively. Combining Eqs. (6.2) and (6.3), and rearranging Eq. (6.4) yields:

$$\text{Concentration Factor} = \frac{1 + \frac{V_{bottom}}{V_{top}}}{K_{DGNP} + \frac{V_{bottom}}{V_{top}}} \quad (6.5)$$

Since the partition coefficient of the DGNPs is much less than V_{bottom}/V_{top} , the concentration factor can be further simplified to:

$$\text{Concentration Factor} \approx 1 + \frac{V_{top}}{V_{bottom}} \quad (6.6)$$

which signifies that the concentration factor is only a function of the volume ratio for extreme K_{DGNP} values. Hence, with a volume ratio of 9:1, or a bottom phase volume that is 1/10 the volume of the total solution, we expect a concentration factor of 10. This prediction was confirmed by the partitioning experiment for the DGNPs, in which $C_{DGNP,bottom}$ was measured after a 12 h incubation. However, since it is not desirable in a point-of-care application to wait 12 h for the ATPS to achieve macroscopic phase separation equilibrium, we took advantage of the observation that the DGNP concentration in the bottom phase was independent of time after 30 min and therefore measured the concentration factor at earlier time points. Fig. 6.4 shows that the concentration factor in the ATPS solution remained relatively constant from 30 min to 12 h. A detailed explanation of this kinetic phase separation phenomenon can be found in the *Discussion* section. As result, the bottom phase was extracted at 30 min for the LFA applications.

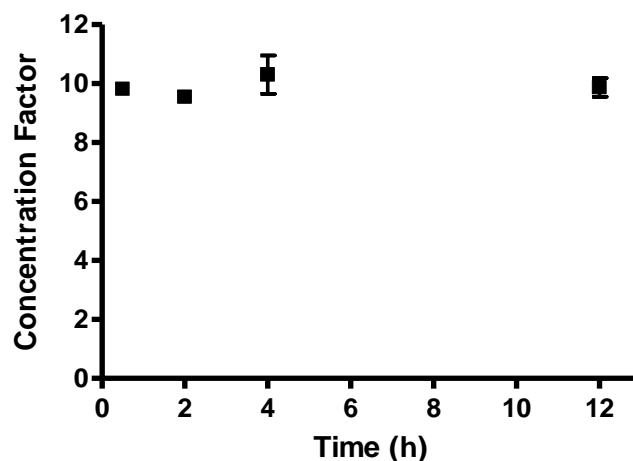


Fig. 6.4. Experimentally measured Tf concentration factors at various time points within a 12-hour period. Error bars represent standard deviations from triplicate measurements

6.3.4 Detecting Tf with LFA

To demonstrate that the DGNPs can be used as a colorimetric indicator for LFA, we first performed LFA for the detection of Tf without the pre-concentration ATPS step. The results of this study are shown in Fig. 6.5a. Since bands were observed on the LFA strips, we concluded that the DGNPs were functional as colorimetric indicators. Each test showed the presence of the control line, which indicated that the fluid flowed completely through the strip and confirmed the validity of the test. For the negative control in which no Tf was present, the appearance of the test line indicated a true negative result. When high Tf concentrations were used (3.16 ng/ μ L and 1.0 ng/ μ L), the test lines were absent, indicating true positive results. However, at lower concentrations such as a 0.316 ng/ μ L, a visible test line appeared, thus indicating a false negative result. This suggested that the detection limit of LFA for Tf without the pre-concentration step was 1 ng/ μ L.

6.3.5 Combining Dextran-Coated Gold Nanoprobes, ATPS, and LFA to Detect Tf

A 9:1 PEG-salt volume ratio solution was utilized to demonstrate that the detection limit of LFA could be improved 10-fold by concentrating the DGNPs saturated with Tf. The results of this study are shown in Fig. 6.5b. As mentioned in the *Materials and Methods* section, after incubating the ATPS solutions for 30 min at room temperature, the concentrated DGNPs in the PEG-poor bottom phases were extracted and applied to LFA. Similar to the previous experiment, both the control line and test line appeared in the absence of Tf, indicating a valid negative result. No test lines appeared at higher Tf concentrations (0.316 ng/ μ L and 0.1 ng/ μ L), while a visible test line first appeared at 0.0316 ng/ μ L, indicating that the detection limit of LFA for Tf with the pre-concentration step was 0.1 ng/ μ L. This corresponded to a 10-fold improvement in the detection limit of LFA when the DGNPs and PEG-salt ATPS were used.

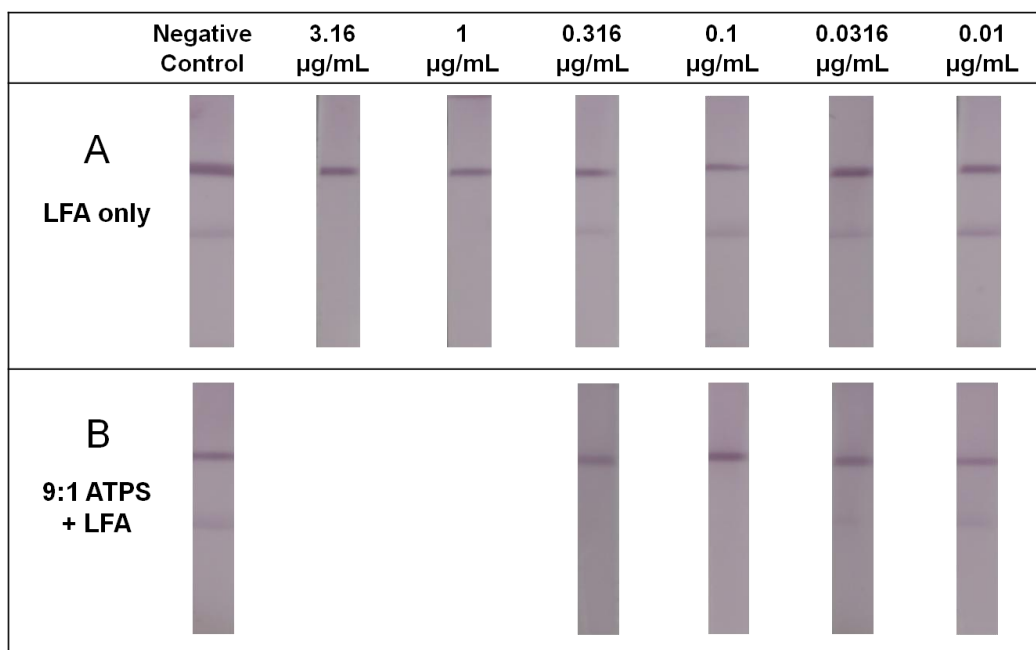


Fig. 6.5. Images of LFA strips used to detect Tf (A) without and (B) with a prior ATPS concentration step

6.3.6 Quantifying LFA Test Line Intensities

To further verify our visual interpretation of the LFA results, images of the test strips were taken, and the intensities of the test lines were quantified. When the pre-concentration step was used, the test line signal for each LFA was weaker when testing the same Tf concentration, indicating that Tf was being concentrated and was saturating the DGNPs. Recall that saturated DGNPs cannot bind to the test line, indicating a positive result. On the other hand, both the control line and test line signal intensities were similar in the negative controls with or without the combination with ATPS. This indicated that the amount of DGNPs traveling up the LFA strips in both experiments were similar. MATLAB analysis of the LFA panels also demonstrated an improvement in the detection limit (Fig. 6.6). Specifically, the two curves in Fig. 6.6 are separated by a 10-fold difference in initial Tf concentration for approximately the same test line signal.

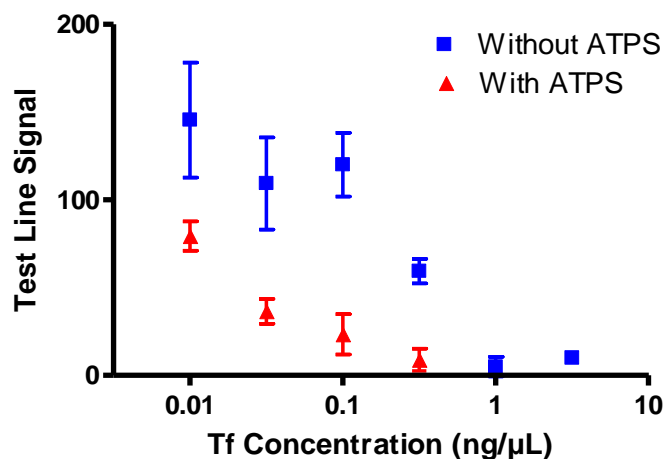


Fig. 6.6. Results of LFA quantification using MATLAB.

6.4 Discussion

Many applications involving gold nanoparticles require that the nanoparticles be stable in complex biological environments such as serum. The traditional citrate-capped, or naked, gold nanoparticles typically do not aggregate in an aqueous solution due to the electrostatic repulsive interactions resulting from the negative charges of the surface citrate ions. However, they will aggregate in solutions of higher ionic strength, where van der Waals attractive interactions become greater than the electrostatic repulsive interactions. This phenomenon can be explained by the Derjaguin and Landau, Verwey and Overbeek (DLVO) theory, which predicts particle interaction energy as a function of the particle charge, particle Hamaker constant, distance between two particles, and ionic strength of the solution. As the ionic strength of the solution increases, the additional ions will screen the electrostatic repulsive interactions, causing van der Waals attractive interactions to dominate and the particles to aggregate. It is therefore necessary to decorate gold nanoparticles with molecules such as polyethylene glycol or dextran to provide additional steric stability.

Dextran-coated gold nanoparticles were successfully made by using dextran instead of citrate as both the reducing and stabilizing agent. To ensure that the nanoparticles remain stable in the bottom, PEG-poor phase, which is estimated to be around 10-12% w/w potassium phosphate, the nanoparticles were added to separate solutions ranging from 5% w/w to 30% w/w potassium phosphate. The critical coagulation concentration (CCC) of the dextran-coated gold nanoparticle was compared to that of the naked gold nanoparticle and PEGylated gold nanoparticle, the latter of which was examined due to its widespread use in the literature [190, 191, 194]. The dextran-coated gold nanoparticle displayed superior colloidal stability with a CCC higher than 30% w/w potassium phosphate, outperforming both the naked gold

nanoparticle and the PEGylated gold nanoparticle. These results therefore demonstrated that dextran could indeed be used to stabilize the gold nanoparticles in our ATPS.

The PEGylated gold nanoparticles were also found to be relatively stable with a CCC between 7.5 and 10% w/w potassium phosphate, which was significantly higher than that of the naked gold nanoparticles. This suggests there is potential for using PEGylated gold nanoparticles in our specific PEG-salt ATPS of interest after additional optimization of the PEG coating, since the potassium phosphate concentration in the bottom phase is approximately 10% w/w. However, the conjugated PEG on the gold nanoparticles interacts favorably with the PEG-rich phase, and as a result, the PEGylated gold nanoparticles partition somewhat preferentially into the PEG-rich phase. Although it is possible to concentrate the PEGylated gold nanoparticles into the PEG-rich phase and then extract the nanoparticles from this phase, we also observed that some of the PEGylated gold nanoparticles concentrate at the interface and in the bottom, PEG-poor phase (data not shown). This was not surprising, since the PEGylated gold nanoparticles are relatively large and experience steric, repulsive excluded-volume interactions with the PEG molecules in the PEG-rich phase, and these interactions compete against the PEG-PEG attractive interactions. Therefore, due to these competing effects, the PEGylated gold nanoparticles do not partition extremely into the PEG-rich phase and exhibit a less than ideal partition coefficient. On the other hand, dextran does not interact favorably with PEG molecules due to being more hydrophilic, and the relatively large dextran-coated gold nanoparticles also experience steric, repulsive excluded-volume interactions with the PEG molecules in the PEG-rich phase. These features taken together lead to the extreme partitioning of dextran-coated gold nanoparticles into the PEG-poor phase.

For the studies combining our PEG-salt ATPS with LFA, the DGNP-rich (PEG-poor) bottom phases were extracted at 30 min, which was well before the system reached macroscopic phase separation equilibrium. This can be explained by examining the kinetic process involved in phase separation. Initially, DGNPs and Tf molecules are dispersed throughout the entire volume of the PEG-salt ATPS, and the anti-Tf antibodies on the DGNPs bind to Tf. At the onset of phase separation, PEG-rich domains, which account for 9/10 of the total volume, and PEG-poor domains, which account for the remaining 1/10 of the total volume, begin to form. Because DGNPs are relatively large and hydrophilic, they partition more extremely into the PEG-poor domains and are concentrated by approximately 10-fold into these smaller volumes. Like-domains then begin to coalesce. As these domains grow larger, the higher density of the PEG-poor domains causes the PEG-rich domains to travel up and the PEG-poor domains to move to the bottom. Over time, a macroscopic PEG-rich phase containing very little DGNPs begins to form on the top of the solution, and a macroscopic PEG-poor phase containing most of the DGNPs begins to form on the bottom. In this process, domains of one phase can become kinetically trapped, or entrained, in the other macroscopic phase. The domains of the smaller volume phase (the PEG-poor, DGNP-rich phase) have a greater tendency to become entrained because they have a harder time finding other PEG-poor domains and coalescing. PEG-poor domains also have to move a greater distance through the larger, more viscous phase (the PEG-rich, DGNP-poor phase) to reach their corresponding macroscopic phase. On the other hand, the domains of the larger volume phase (the PEG-rich phase) are not significantly entrained because they have an easier time finding other PEG-rich domains and coalescing, and because they have a smaller, less viscous volume phase (the PEG-poor phase) to move through to get to their corresponding macroscopic phase. Since the entrainment of the PEG-rich domains in the

macroscopic PEG-poor phase is quite negligible, the concentration of DGNPs that is measured in the bottom, macroscopic PEG-poor bottom phase is expected to stay relatively constant over time. If entrainment had been significant, the entrained domains would act to decrease the measured DGNP concentration as the entrained PEG-rich domains have a much lower concentration of DGNPs than the macroscopic PEG-poor phase. In such a scenario, the measured concentration of DGNPs would increase with time, which was not the case in our system. Since we only require 20 μL of sample for LFA, we only need to extract a small amount of the bottom phase, and we can extract such a small sample volume even in 30 min and still obtain the equilibrium predicted 10-fold concentration of the DGNPs.

As mentioned in the *Results* section, the detection limit of LFA for Tf without the pre-concentration step was 1 $\text{ng}/\mu\text{L}$. This indicates that Tf was successfully detected at 1 $\text{ng}/\mu\text{L}$, and the anti-Tf antibodies conjugated to the DGNPs were saturated with Tf. In the case of a Tf concentration of 0.1 $\text{ng}/\mu\text{L}$, which is 10 times more dilute, to ensure that there are enough Tf molecules to saturate the anti-Tf antibodies conjugated to the DGNPs, 10 times the volume of the 0.1 $\text{ng}/\mu\text{L}$ Tf solution could be added to the same amount of DGNPs. However, only a limited volume can be applied to the LFA test strip before the strip is saturated with liquid, and only a small portion of the saturated DGNPs would actually pass through the LFA test strip. In this scenario, not enough DGNPs would flow through the strip, and a control line would not form, indicating an invalid test. Therefore, it is necessary to concentrate the DGNPs by 10-fold, which would counteract the 10-fold dilution associated with the addition of DGNPs to the ATPS solution. By combining the DGNPs with our ATPS, not only do we retain the original DGNP concentration, but we more importantly expose the DGNPs to 10 times the amount of Tf in the process, which is critical to achieve saturation of the anti-Tf antibodies at the lower

concentration. We were thus able to use our PEG-salt ATPS with a PEG-rich:PEG-poor volume ratio of 9:1 to improve the detection limit of LFA for Tf by 10-fold.

6.5 Conclusions

In this study, we introduced a novel combination of dextran-coated gold nanoprobe, the PEG-salt ATPS, and LFA for protein diagnostics. First, we showed that the dextran coating on the gold nanoparticles provided excellent colloidal stability even in solutions of high ionic strength. This ensured that the DGNPs do not aggregate in the PEG-salt ATPS. We confirmed our expectation that the DGNPs partition extremely into the salt-rich, PEG-poor bottom phase of the PEG-salt ATPS. This was due to dextran being more hydrophilic than PEG and the steric, repulsive excluded-volume interactions that operate between the DGNPs and the PEG molecules of the PEG-rich phase. When an ATPS solution with a PEG-rich phase:PEG-poor phase volume ratio of 9:1 was used, given the extreme partition coefficient of the DGNPs, the concentration factor of the DGNPs was predicted to be approximately 10. This was confirmed in our partitioning experiments using radiolabeled DGNPs. Furthermore, we showed that the DGNPs can be extracted from the PEG-salt ATPS at approximately 30 min, since the concentration of the DGNPs in the PEG-poor phase quickly attains a constant value, even though domains of the PEG-poor phase are kinetically trapped in the macroscopic PEG-rich phase. Finally, by using the PEG-salt ATPS and the DGNPs as a pre-concentration step, we demonstrated a 10-fold improvement in the detection limit of Tf using LFA. The results were validated both qualitatively using images of the LFA strips and quantitatively using a custom MATLAB script.

The proof-of-concept studies reported in this chapter demonstrated the important role of DGNPs in our attempt to develop an effective protein detection assay. Although dextran-coated

nanoparticles have been used in other applications, this represents their first use as colorimetric indicators for LFA. Our use of DGNPs also suggests that the surface coating of gold nanoparticles can be manipulated to change their partitioning behavior in our ATPS. In the future, we can adjust the amount or the length of the coating polymer on the gold nanoparticle surface to increase or decrease the partitioning of the nanoparticle in our system. The operating conditions and the composition of the PEG-salt ATPS solution can be further adjusted to obtain even greater concentration-fold improvements by achieving more extreme volume ratios. The overall success of our results suggests the potential for the continual investigation of our simple and inexpensive system in a variety of point-of-care settings.

Chapter 7: A rapid and sensitive paper-based immunoassay for protein detection using interface extraction of an aqueous two-phase system

7.1 Motivation and background

Developing a detection assay for proteins that is rapid, portable, and also sensitive has been challenging in the field of diagnostics [85, 127, 207]. Lab-based immunoassays, such as the enzyme-linked immunosorbent assay (ELISA), display good sensitivity and are the gold standard for detecting protein targets. However, lab-based assays are not practical for use in resource-poor settings that lack power, equipment, and trained personnel. On the other hand, the paper-based lateral-flow immunoassay (LFA) is inexpensive, rapid, portable, and easy to use. However, the sensitivity of LFA is significantly lower than that of lab-based assays, and LFA cannot therefore be used to detect target proteins that are present at low concentrations [140, 142]. Hence, while LFA is very popular and effective in detecting the glycoprotein human chorionic gonadotropin (hCG), a biomarker for pregnancy which exists abundantly in urine from a pregnant woman [208], LFA is not widely used in areas where the target proteins in sample solutions are not as abundant, such as in the detection of infectious and biowarfare agents [160, 209, 210].

The detection limit of LFA is typically 1-2 orders of magnitude higher than ELISA [85]. While concentrating targets in a sample prior to detection can improve the detection limit, concentrating proteins generally requires lab-based equipment and therefore typically cannot be combined with point-of-care assays. Our laboratory however has been focusing on concentrating the target analytes into one of the bulk phases (top or bottom) of aqueous two-phase systems (ATPSs). The ATPS is suitable for LFA since it is also portable, easy to use, and does not require laboratory equipment. Some ATPSs like the polyethylene glycol (PEG)-salt system

exhibit a homogeneous, isotropic phase at low temperatures. Upon increasing the temperature, macroscopic phase separation is induced. If biomolecules are present in an ATPS solution, they will distribute, or partition, between the two bulk phases based on their physical and chemical properties, such as size and hydrophobicity. By adjusting the operating conditions of the ATPS, we established a volume ratio, which is the ratio of the volume of the top phase to that of the bottom phase, that was much greater or much less than 1. This minimized the volume of the phase where the target molecules partitioned, effectively concentrating the target molecules in a small volume phase that was then extracted and applied for the subsequent detection assay. Specifically, we successfully used a micellar ATPS to concentrate a model virus by 10-fold and subsequently improved the detection limit of LFA by 10-fold [211]. For protein biomarkers which are smaller than viruses and thus harder to concentrate, we utilized a novel approach of capturing the protein of interest in the sample using gold nanoproboscopes (GNPs), which are gold nanoparticles decorated with specific antibodies, and then using the large size of the GNPs to concentrate the model protein by 10-fold, which then improved the detection limit of LFA by 10-fold [212].

While we have demonstrated the combination of ATPS with LFA, the improvement of LFA depends on the fold-concentration that can be achieved in the ATPS, and this depends entirely on how small of a volume can be achieved for the target-rich phase. A more extreme volume ratio therefore will yield a more concentrated target biomolecule. However, more extreme volume ratios result in longer phase separation times since it takes longer for the microscopic domains that form the smaller phase to find each other, coalesce, and travel to the respective top or bottom phase [133]. In this study, we optimized the concentration of biomolecules using a single ATPS step by driving the target biomolecules towards the interface

between the two bulk phases. Since the interfacial region represents a very small volume region that can form irrespective of the volume ratio, this novel approach allows us to concentrate the targets without depending on extreme volume ratios (volume ratios much greater or much less than 1), which have long phase separation times. Instead, the volume ratio that can reach equilibrium the fastest was chosen, and this reduced the extraction time to within 10 minutes, a significant improvement over our previous approach. We also view this approach as moving towards the maximum fold-concentration that can be achieved in a single ATPS step since the volume of the interface is much smaller than the two macroscopic bulk phases, and therefore, the biomolecules can be concentrated much more extremely. Last but not least, increasing the sample volume desirably increases the total number of target biomolecules that can be concentrated at the interface and then be detected with LFA. While this is also true for concentrating target molecules in a bulk phase using extreme volume ratios, increasing sample volume also increases phase separation times. In the proposed interfacial extraction approach, an extreme volume ratio is no longer necessary. Figure 7.1 pictorially compares interface extraction with extraction of one of the two bulk phases.

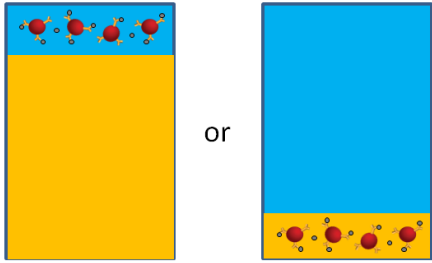
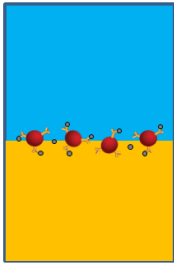
Extraction type	Bulk phase extraction	Interface extraction
Schematic		
Phase separation time	> 6 h	10 min
Extraction time	> 30 min	10 min
Volume ratio	1:9 or 9:1	1:1
Concentration factor	~10	10 - 100

Figure 7.1. Summary of the technical innovation and improvements relative to our previous proof-of-concept studies.

In order to drive the target biomolecules towards the interface, we utilized a capture mechanism involving GNPs. With the specific antibodies decorated on the particle surface, the GNPs first captured the target proteins in the sample. The surface chemistry of the GNPs was optimized so that the particles would partition to the interface upon phase separation. Proteins that were captured by GNPs were then extracted at the interface. Since the volume of the interface was very small, the proteins were highly concentrated and subsequently applied to an LFA detection strip. This chapter summarizes our work where we first prepared GNPs that were capable of partitioning to the interface of our PEG/salt ATPS. We then investigated the volume ratio that phase separated the fastest and also allowed for the greatest recovery of GNPs. Lastly, using a model protein transferrin (Tf), we demonstrated the 100-fold improvement of LFA for Tf in combination with the ATPS interface extraction step.

To our knowledge, this is the first ever study to utilize nanoprobe to drive target biomolecules towards the liquid-liquid interface of an ATPS to improve concentration. The technical innovation described in this chapter provides an effective yet rapid method to improve the detection limit of LFA by 100-fold, closing the gap in sensitivity between lab-based and paper-based immunoassays. An improved LFA with enhanced sensitivity would have a significant impact in the field of diagnostics, providing a point-of-care solution that is currently not available. On the other hand, while we demonstrated that this approach could improve the performance of LFA detection, this pre-concentration procedure can also be applied to other detection methods.

7.2 Materials and Methods

7.2.1 Radiolabeling the anti-Tf antibody

All reagents and materials were purchased from Sigma-Aldrich (St. Louis, MO) unless noted otherwise. ^{125}I was used to radiolabel the tyrosine residues of goat anti-human Tf antibody (Bethyl Laboratories, Montgomery, TX). Briefly, Na^{125}I (MP Biomedicals, Irvine, CA) were activated by IODO-BEADS (Pierce Biotechnology, Rockford, IL). Subsequently, the activated ^{125}I was reacted with goat anti-Tf antibodies for 15 min. The radiolabeled proteins were purified, and free ^{125}I was removed using a Sephadex G10 size-exclusion column. The phosphotungstic acid assay was used to quantify the radioactivity and concentration of the radiolabeled proteins.

7.2.2 Preparing GNPs

The naked gold nanoparticles were prepared using a protocol described by Frens [68], resulting in a clear, cherry-colored solution with particle sizes around 25-30 nm in diameter. To prepare the GNPs, 320 mg of goat anti-Tf antibody was incubated with 20 mL of a colloidal gold solution for 30 min, followed by the addition of thiolated-PEG₅₀₀₀ using a molar ratio of 3000:1 for PEG:GNP and an additional incubation of 30 min. To prevent nonspecific binding of other proteins to the surfaces of the colloidal gold, 2 mL of a 10% bovine serum albumin (BSA) solution was added to the mixture and mixed for an additional 15 min. The resulting solution was gently mixed on a shaker during the incubation period. To remove free, unbound antibodies, PEG, and BSA, the mixture was subsequently centrifuged for 30 min at 4°C and 9,000 g. The pellet of GNPs was washed with a 1% BSA solution, and this washing step was repeated twice. Finally, the recovered GNPs were resuspended in 3 mL of a 0.1 M sodium borate buffer at pH 9.0.

7.2.3 Partitioning GNPs

The GNPs decorated with radiolabeled anti-Tf antibodies were partitioned in the ATPS at different conditions to determine the volume ratio that could yield the fastest and highest GNP recovery. For each partitioning experiment, 3 identical PEG-salt solutions in Dulbecco's phosphate-buffered saline (PBS; Invitrogen, pH 7.4, containing 1.47 mM KH₂PO₄, 8.10 mM Na₂HPO₄, 138 mM NaCl, 2.67 mM KCl and 0.495 mM MgCl₂) were prepared to a total volume of 500 µL. PEG-salt ATPS solutions with three different volume ratios (1:1, 6:1 and 1:6) were prepared using specific concentrations of PEG and potassium phosphate. Subsequently, 10 µL of

GNP decorated with radiolabeled anti-Tf antibodies were added to each APTS solution. The solutions were equilibrated at 4°C to ensure that the solutions were homogeneous. Once equilibrium at 4°C was attained, the solutions were incubated in a water bath at 37°C to induce phase separation, and the GNPs were found to partition between the two coexisting phases. The GNPs at the interface were withdrawn carefully using pipettes, and 30 µL of the interface solution was withdrawn to ensure most, if not all, of the GNPs at the interface were collected. The two coexisting phases were also withdrawn separately using pipettes. The amount of GNPs at the interface and in the two coexisting phases were quantified by measuring the amount of radioactivity in each region using the Cobra Series Auto-Gamma Counter since the GNPs were bound to radiolabeled anti-Tf antibodies. The quantified amount of GNPs in each of the three regions was used to calculate the recovery percentage of the GNPs at the interface using a mass balance.

To demonstrate that the GNPs can also be recovered in solution with a larger sample volume, the experiment described above was repeated by increasing the sample volume by 10-fold. Therefore, 5000 µL instead of 500 µL of the PEG-salt APTS solutions were used. Identical amounts of the GNPs decorated with radiolabeled antibody (Ab, 10 µL) were added to each of these 5000 µL solutions.

7.2.4 Preparing the LFA test strip

The LFA test utilizing the competition mechanism was implemented in this study (Figure 7.2). In the competition assay, the target of interest is immobilized on a nitrocellulose membrane to form the test line. Immobilized secondary antibodies against the primary antibodies on the

GNPs make up the control line. In LFA, when the sample first comes in contact with the GNPs, if the target molecules are present in the sample, they will bind to their specific antibodies decorated on the GNPs. If the target molecules present in the sample saturate the antibodies on GNP, then these GNPs can no longer bind to the immobilized target molecules on the test strip. As a result, the GNPs do not form a visual band at the test line, and this indicates a positive result. On the other hand, if the sample does not contain the target molecules at a concentration that can saturate the antibodies on the GNPs, these antibodies on the GNPs can bind to the immobilized target molecules on the test strip and form a visual band at the test line. This indicates a negative result. Furthermore, regardless of the presence of the target molecule in the sample, the antibodies on the GNPs will bind to the immobilized secondary antibodies on the control line, indicating that sufficient sample has wicked through the test line and reached the control line. The presence of the visible control line indicates a valid test.

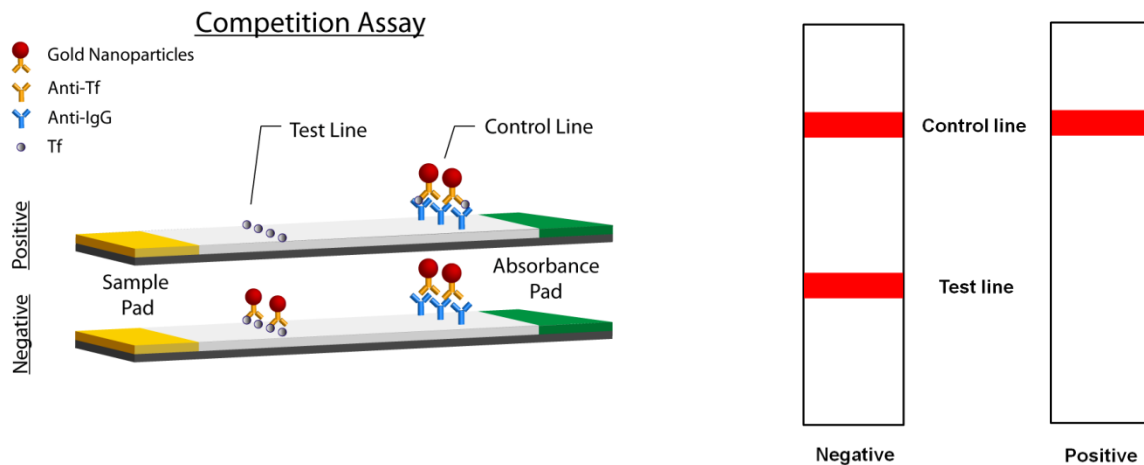


Figure 7.2. Schematic representation of LFA using the competition mechanism and the interpretations of the positive and negative results.

7.2.5 Performing LFA with Tf but without pre-concentration

Tf stock solutions containing varying concentrations of Tf were prepared in PBS. Subsequently, 20 μL of each Tf stock solution was added to 10 μL of the GNP solution and 20 μL of test buffer (0.2% BSA, 0.3% Tween20, 0.2% sodium azide, 0.1% polyethylene glycol, 0.1 M Trizma base, pH 8), which was used to aid the flow of the samples through the test strips. A total of 5 sample solutions (50 μL each) with various concentrations of Tf were prepared (0 (negative control), 0.01, 0.1, 1, and 10 $\text{ng}/\mu\text{L}$). A test strip was dipped vertically into each sample solution, where the sample pad would come in contact with the solution. After 10 min, the test strips were taken out, and an image of each strip was immediately taken by a Canon EOS 1000D camera.

7.2.6 Combining the ATPS interface extraction with LFA for Tf

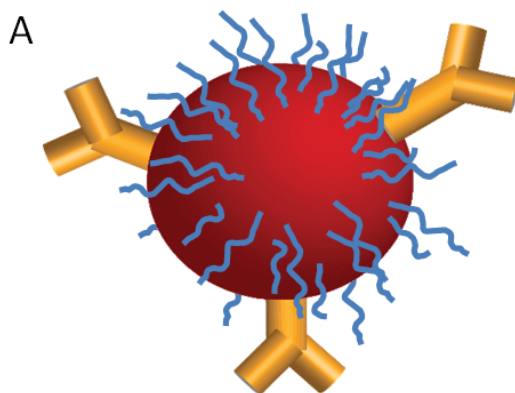
A volume ratio of 1:1 was used for this study based on the findings from the *Partitioning of GNPs* experiment. By utilizing anti-Tf antibodies, the GNPs can capture Tf in the sample followed by the concentration of the Tf-GNP complex at the interface. A similar protocol to that described in the *Partitioning of GNPs* section was used except that various concentrations of Tf were also spiked into the ATPS solutions. Briefly, 10 μL of the GNP solution was added to either 490 μL or 4990 μL of the Tf-spiked ATPS solution that yielded a 1:1 volume ratio and that contained various Tf concentrations (0 (negative control), 0.01, 0.1, and 1 $\text{ng}/\mu\text{L}$). The solutions were equilibrated at 4 $^{\circ}\text{C}$ to ensure that the solutions were homogeneous. Once equilibrium was attained, the solutions were placed in a water bath at 37 $^{\circ}\text{C}$ to trigger phase separation. After 10 min, 30 μL of the interface solution, which contained the concentrated




GNPs and Tf, were withdrawn. This interface solution was mixed with 20 μL of test buffer to form the 50 μL sample solution. An LFA test strip was dipped vertically into each sample solution, where the sample pad would come in contact with the solution. After 10 min, the test strips were taken out, and an image of each strip was immediately taken by a Canon EOS 1000D camera (Canon U.S.A., Inc., Lake Success, NY).

7.3 Results and discussions

In order to combine the ATPS interface extraction with the paper-based LFA detection assay, the GNPs developed in this study possessed three functions. First, the decorated specific antibodies on the surfaces of the GNPs captured the target proteins present in the sample. Second, the optimized formulation of PEG and proteins on the surfaces of the GNPs caused the GNPs to partition to the interface and not the bulk phases. Lastly, the GNPs acted directly as the colorimetric indicator for LFA, and hence allowed the subsequent detection assay to be performed immediately without extra washing or other preparation steps. A schematic of the GNP is shown in Figure 7.3A. The GNP has 3 main components: the PEG polymers, the gold nanoparticle, and the anti-Tf antibodies. Each component by itself would drive the nanoparticle into one of the two bulk phases. First, decorated PEG increases the hydrophobicity of the GNP and drives the nanoparticle into the top PEG-rich phase due to the favorable PEG-PEG interactions between the polymer on the particle surface and the polymer in the top phase (Figure 7.3B). The large size of the gold nanoparticle, on the other hand, causes the nanoparticle to partition into the bottom PEG-poor phase where it would experience fewer repulsive, excluded-volume interactions with the PEG polymers. The hydrophilic proteins (anti-Tf Ab and BSA) on

the GNP increase the hydrophilicity of the GNP, and also cause it to partition into the bottom PEG-poor phase. However, since the bottom PEG-poor phase is also salt-rich, the nanoparticles aggregate when there is not enough PEG on the surfaces of the nanoparticles to provide sufficient steric stability (Figure 7.3C). In combination, the 3 components of the GNP can be varied and delicately balanced to ultimately drive the GNP to the interface in our ATPS (Figure 7.3D).



 PEG	 Gold nanoparticle	 Anti-Tf
<ul style="list-style-type: none"> ▪ Prevents aggregation of GNPs in the high salt environment of the PEG-poor phase. ▪ Increases the hydrophobicity of the nanoparticles by increasing PEG-PEG interactions to drive the nanoparticle into the PEG-rich phase. 	<ul style="list-style-type: none"> ▪ Greater excluded-volume interactions with PEG in the PEG-rich phase drive the nanoparticles into the PEG-poor phase. 	<ul style="list-style-type: none"> ▪ Increases the hydrophilicity of the nanoparticles to drive the nanoparticles into the PEG-poor phase.

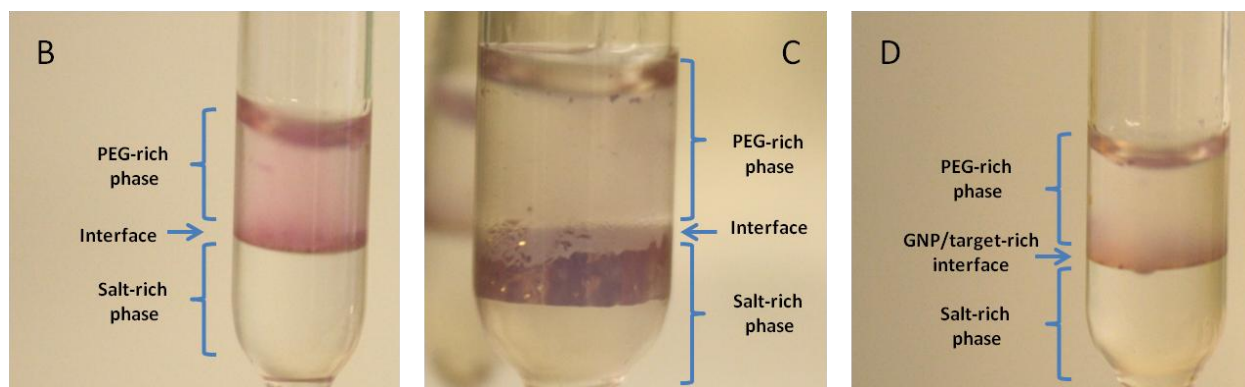


Figure 7.3. (A) Schematic of GNP and the functionality of each component. To demonstrate that the partitioning behavior of GNPs in our PEG-salt ATPS can be customized, various amounts of PEG were conjugated to the GNPs to manipulate their partitioning behavior: (B) Using a molar ratio of 5000:1 PEG:GNP during conjugation, the resulting GNPs partitioned preferentially into the PEG-rich top phase. (C) Using a molar ratio of 1000:1 PEG:GNP during conjugation, the GNPs partitioned into the PEG-poor bottom phase but aggregated since that phase has a high salt concentration. These aggregated GNPs could not be used in the subsequent detection assay. (D) Using a molar ratio of 3000:1 PEG:GNP during conjugation, the resulting GNPs partitioned extremely to the interface. For (B), (C), and (D), the red observed at the very top of the liquid-air interface was due to a reflection and not due to the presence of nanoprobables.

In the competition LFA, the successful detection of the target protein in the sample relies on the antibodies on the GNPs being saturated by the target. If the antibodies are not saturated, then the GNPs can bind to the immobilized targets on LFA to form a test line, indicating a false negative result. One way to detect a sample that has a low concentration of the target is to increase the sample volume. That would increase the total number of target molecules, which in turn, would potentially lead to saturation of the antibodies for a given fixed amount of GNPs. However, only a small volume can flow through the LFA test strip, and since the GNPs are diluted in this approach, if not enough GNPs flow through the test strip, then the control line would not be visible, indicating an invalid result. Since the use of the ATPS interface extraction offers a rapid and effective means to gather the GNPs that are saturated with target proteins in a

small volume, this approach can lead to the detection of low concentrations of target proteins by allowing a much larger sample volume to be analyzed.

Three volume ratios were tested to determine the optimal volume ratio that could recover most GNPs within the shortest period of incubation. The results are shown in Table 7.1. It is not surprising to observe that the 1:1 volume ratio phase separated the fastest and allowed for the greatest recovery of the GNPs. When phase separation is triggered by increasing the temperature, microscopic PEG-rich and PEG-poor domains are formed, and similar domains will find each other and coalesce. As the domains coalesce, they travel and eventually form the macroscopic PEG-rich phase on top and the macroscopic PEG-poor, salt-rich phase on the bottom due to the interfacial tension and the density difference between the two phases. A 1:1 volume ratio will phase separate faster than the 6:1 or 1:6 volume ratios since the domains have an easier time finding each other and coalescing when there is a significant amount of each phase. For more uneven volume ratios, domains of the smaller volume phase can be entrained in the larger continuous phase due to the domains experiencing difficulty coalescing. Moreover, the 6:1 volume ratio is also expected to phase separate more slowly than the 1:6 volume ratio since the PEG-rich phase is the continuous phase for the 6:1 volume ratio, and the PEG-poor domains will experience more difficulty finding each other and moving to their respective macroscopic phase in the more viscous PEG-rich continuous phase.

Table 7.1. Recovery of the GNPs for different volume ratios.

Volume ratio (top phase: bottom phase)	Phase separation time	GNP recovery (500 μ L)	GNP recovery (5000 μ L)
1:1	10 min	89.3 \pm 1.4%	84.1 \pm 1.8%
6:1	60 min	76.5 \pm 8.8%	64.8 \pm 1.8%
1:6	30 min	75.5 \pm 6.0%	70.9 \pm 6.6%

Since the GNPs do not partition into either domain, they remain between the domains as the domains coalesce. Eventually, the GNPs appear as a thin red film at the interface when phase separation is completed. The recovery of GNPs is more efficient when using the 1:1 volume ratio as entrainment is minimized at this volume ratio and less of the GNPs would therefore be lost to the interfaces that are present between the entrained domains and the continuous phase. Since the 1:1 volume ratio phase separated the fastest while yielding the highest GNP recovery, it was used in the subsequent experiments.

To demonstrate the enhancement of LFA by incorporating the APTS interface extraction step, we utilized the model protein transferrin (Tf). Tf is a serum protein for iron transportation, and in addition to both Tf and its antibody being commercially available and inexpensive, we have experience radiolabeling the Tf antibody, which was important in determining GNP recovery. To establish the detection limit of Tf in LFA, we performed a series of LFA tests with various Tf concentrations without any prior concentration step. If a sample contained enough Tf molecules to saturate the anti-Tf antibodies decorated on GNP, then these anti-Tf antibodies did not bind to the immobilized Tf on the nitrocellulose membrane at the test line and therefore did not form a visual band at the test line. This indicated a positive result, which was observed when testing the samples with a Tf concentration of 1 ng/ μ L (Figure 7.4, top panel). On the other hand, if insufficient or no Tf was present in the sample to saturate the anti-Tf antibodies, then these anti-Tf antibodies did successfully bind to the immobilized Tf on the nitrocellulose membrane and therefore formed a visual band at the test line. This indicated a negative result, which was observed when testing samples with Tf concentrations less than 1 ng/ μ L. Since 1 ng/ μ L is the lowest Tf concentration that showed a true positive result, this indicated a detection limit of approximately 1 ng/ μ L for Tf when performing LFA without the prior concentration step.

To determine if the ATPS interface extraction step could improve the detection limit of Tf by 10-fold using LFA, we applied the same amount of the GNPs to the ATPS solutions with Tf concentrations that were 10 times lower than the detection limit of LFA (0.1 ng/ μ L). Since we had an idea of the number of Tf molecules required to saturate the antibodies, we increased the sample volume 10-fold from 50 μ L to 500 μ L to keep the total number of Tf molecules the same. Since only a limited amount of sample (50 μ L) could be applied to an LFA test strip, the diluted GNPs in this larger sample solution needed to be concentrated and applied to LFA to obtain a valid result. To recover these GNPs that were saturated with the target proteins, we placed the solution in a water bath at 37°C to collect the GNPs at the interface within 10 min. The GNPs were then extracted and applied directly to the LFA test strip. The results of this study are shown in the middle panel of Figure 7.4. We were able to obtain a true positive result at 0.1 ng/ μ L, which showed a 10-fold improvement in the detection limit. The test line intensities of LFA using this approach were lighter than those without the prior concentration step when comparing samples with the same Tf concentration, indicating that more Tf was captured to prevent the GNPs from binding to the test lines. The test line intensities also increased as the Tf concentration decreased, which was expected as the amount of Tf available to saturate the antibodies decreased. To further demonstrate the advantage of using the ATPS interface extraction, we repeated our previous experiments with the ATPS solutions but with Tf concentrations 100 times below the detection limit of LFA and sample volumes that were 100 fold greater (5000 μ L). As indicated Table 7.1, we were still able to recover 84.1% of the GNPs even at the larger 5000 μ L volume. Moreover, Figure 7.4, shows that the detection limit of LFA was further reduced to 0.01 ng/ μ L, indicating a 100-fold improvement in detection limit compared to LFA without any prior concentration step.

	Negative (0 ng/ μ L)	1 ng/ μ L	0.1 ng/ μ L	0.01 ng/ μ L	0.001 ng/ μ L
LFA only (50 μ L)					
ATPS Interface extraction + LFA (500 μ L)					
ATPS Interface extraction + LFA (5000 μ L)					

Figure 7.4. Results of LFA for detecting Tf without (top panel) and with (500 μ L, middle panel; 5000 μ L, bottom panel) the prior concentration step using the ATPS interface extraction.

7.4 Conclusions

In this study, a novel approach to improve the performance of the LFA paper-based immunoassay was investigated. Specifically, a multi-functional nanoprobe, or the GNP, was

developed and utilized to first capture target protein molecules in a sample, then concentrate preferentially to the interface of the ATPS, and finally serve as the colorimetric indicator for LFA. Different volume ratios of the PEG-salt ATPS were investigated to achieve the fastest and greatest recovery of the GNPs at the interface. A 1:1 volume ratio was found to be optimal since over 80% of the GNPs could be recovered at the interface within only 10 min. Using this volume ratio, we subsequently demonstrated the improved performance of detecting a model protein with LFA by combining LFA with the ATPS interface extraction. This effectively decreased the detection limit of LFA by 100-fold. We believe that the innovation described in this chapter will have great impact on the emerging field of paper-based assays since we provide a rapid, inexpensive, and highly effective solution for concentrating proteins with minimal power and no need for laboratory equipment.

Chapter 8: Simultaneous concentration and detection of biomarkers on paper

8.1 Motivation and background

Over 95% of deaths due to major infectious diseases (HIV, malaria, acute respiratory infections, and tuberculosis) occur in resource-poor countries [159]. There is a critical need for earlier detection of these diseases as it can lead to better patient management, faster administration of treatments, and improved outbreak prevention [213]. However, the current diagnostic technologies capable of providing rapid and accurate detection are not readily available in developing nations due to limited access to electricity, laboratory equipment, and trained personnel [214]. To overcome these challenges, resource-poor countries need an equipment-free diagnostic assay that is rapid, simple to use, low-cost, easy to interpret, and applicable at the point-of-care (POC) [215]. A paper-based analytical device has the potential to satisfy the aforementioned criteria since paper is readily available, affordable, and possesses an intrinsic wicking mechanism that can quickly transport fluids without the aid of an active pumping system. One common paper-based diagnostic device is the lateral-flow immunoassay (LFA), a rapid antibody-based test that has been used successfully in off-the-counter pregnancy tests and urine drug test kits. Despite its strengths as a POC device, the detection limit of LFA is still inferior in comparison to that of gold-standard diagnostic laboratory assays such as the enzyme-linked immunosorbent assay (ELISA) and polymerase chain reaction (PCR) [159].

The Whiteside and Yager groups have developed novel methodologies to improve detection in paper-based devices. Specifically [182, 216], the Whitesides group developed a low-cost paper-based ELISA with multiple wash and reagent steps that bring its detection limit close to that of traditional ELISA [217]. Meanwhile, the Yager group developed a two-dimensional

paper network format featuring easily performed multi-step signal amplification assays that yield a 4-fold improvement in the detection limit. Concurrently, our group was the first to demonstrate that an aqueous two-phase system (ATPS) can be used to concentrate a target biomarker into a smaller volume before addition to LFA. Using this method, a 10-fold improvement in the overall detection limit of LFA was achieved for a model virus bacteriophage M13 and a model protein transferrin (Tf) [167, 168]. However, this approach was also limited by its time-to-result and ease-of-use, as the user had to wait for the two phases of the ATPS to macroscopically separate before extracting the target phase containing the concentrated biomarker and applying to LFA.

Here we improve sensitivity, speed, and ease-of-use with a next-generation, all-in-one device possessing both ATPS phase separation and downstream detection capabilities. Instead of applying the concentrated sample after phase separation of ATPS, this device revolves around a new phenomenon we discovered, which enables the direct addition of a mixed ATPS to the paper-based device. The solution separates into its two phases as it flows towards the detection zone, allowing for the concentration and detection steps to occur simultaneously and further reducing the overall time-to-result. Although the precise mechanism is still under investigation, our studies on this newly discovered concentrating phenomenon suggest that the paper membrane speeds up the macroscopic phase separation of the ATPS. To further capitalize on this phenomenon, we expanded the paper device vertically, thereby increasing the cross-sectional area of flow and exploiting the effects of gravity on macroscopic separation. In addition to accelerating phase separation, this 3-D component also has the ability to process larger, more dilute volumes of sample, leading to greater concentration-fold improvements. This is the first time that phase separation in paper has been investigated, and the novel integration of ATPS and LFA within a 3-D paper architecture successfully yielded a 10-fold improvement in the detection

limit of our model protein Tf, while reducing the overall time-to-result and maintaining ease-of-use. Our device provides a significant improvement over traditional LFA tests and can be modified for the detection of a variety of diseases with low characteristic biomarker levels. This new platform technology is highly sensitive, low-cost, rapid, equipment-free, and therefore has the potential to revolutionize the current state of diagnostic healthcare within resource-poor regions.

8.2 Materials and Methods

8.2.1 Determining the Polymer-Salt ATPS Solution Volume Ratios

All materials, chemicals, and reagents were purchased from Sigma-Aldrich (St. Louis, MO) unless otherwise noted. Polyethylene glycol 8000 (PEG, VWR, Brisbane, CA) and potassium phosphate salt (5:1 dibasic to monobasic ratio) were dissolved in Dulbecco's phosphate-buffered saline (PBS; Invitrogen, Grand Island, NY, pH 7.4, containing 1.47 mM KH_2PO_4 , 8.1 mM Na_2HPO_4 , 137.92 mM NaCl, 2.67 mM KCl, and 0.49 mM MgCl_2). The equilibrium volume ratios (volume of the top phase divided by the volume of the bottom phase) were obtained by varying the w/w compositions of PEG and salt along the same tie line. The 1:1 and 9:1 volume ratio ATPSs were found and used for further experiments.

8.2.2 Preparation of antibody-decorated dextran-coated gold nanoparticles (DGNPs)

Dextran-coated gold nanoparticles were synthesized according to Min and coworkers with slight modifications [218]. Briefly, 6 g of dextran (Mw. 15,000 – 25,000) from *Leuconostoc* spp. were dissolved in 80 mL of filtered UltraPure sterile water (Rockland Immunochemicals

Inc., Gilbertsville, PA). The solution was stirred and heated to a boil, after which 1080 μL 1% w/v gold (III) chloride hydrate solution was added. The color of the reaction mixture turned reddish-violet and was stirred and boiled for about 20 min. The newly formed dextran-coated gold nanoparticles were centrifuged to remove free dextran and resuspended in 70 mL of water. To form functionalized DGNPs, the pH of the dextran-coated gold nanoparticle solution was adjusted to 9.0 using 1.5 M NaOH. For every 1 mL of dextran-coated gold nanoparticle solution, 8 μg of anti-Tf antibodies (Bethyl Laboratories, Montgomery, TX) were added. The reaction mixture was placed on a shaker for 30 min to facilitate the formation of dative bonds between the antibodies and the dextran-coated gold nanoparticles. Free antibodies were removed by centrifugation. The pellet was resuspended in 100 μL of 0.1 M sodium borate buffer at pH 9.0.

8.2.3 Visualization of ATPS

In order to visualize the two phases of the ATPS, dextran-coated gold nanoparticles, which are purple due to surface plasmon resonance [219, 220], and Brilliant Blue FCF dye (The Kroger Co., Cincinnati, OH) were added to the 1:1 and 9:1 volume ratio PEG-salt ATPSs to form final solutions of 3 g. These solutions were well-mixed through vortexing and incubated at 25 °C. Pictures of the solutions were taken when the ATPS reached equilibrium. All images were captured using a Canon EOS 1000D camera (Canon U.S.A., Inc., Lake Success, NY).

The two phases of the ATPS were then visualized as they flowed along a paper membrane. Two 8 x 30 mm strips of fiberglass paper were laser cut with a VersaLASER 3.50 (Universal Laser Systems, Scottsdale, AZ). Subsequently, 50 mg of the mixed ATPS (corresponding to the 1:1 or 9:1 equilibrium volume ratio) containing Brilliant Blue FCF dye and dextran-coated gold nanoparticles were added to one end of the strips. Images of the resulting

flow were captured at 0, 30, 105, and 300 sec. Video was also taken with a 8-megapixel camera from a commercial smart phone (Apple Inc., Cupertino, CA).

To visualize the phase separation of the ATPS within the 3-D paper well, 140 mg of a mixed ATPS containing Brilliant Blue FCF dye and dextran-coated gold nanoparticles were added to the paper well. The 3-D paper well was formed by stacking nine 8 x 10 mm laser-cut strips of fiberglass paper on one edge of an 8 x 60 mm laser-cut strip of fiberglass. After the mixed ATPS was applied to the 3-D paper well, 50 μ L of running buffer (0.2% bovine serum albumin (BSA), 0.3% Tween20, 0.1 M Trizma base, pH 8) were added to the 3-D paper well. As with LFA in general, a running buffer was added to assist the flow of the sample from the paper well to the rest of the device. Video was taken and images were captured at 0 and 30 sec, at the addition of running buffer, and after completion of flow.

8.2.5 Detection of Tf

8.2.5.1 LFA tests for detection of Tf

LFA test strips utilizing the competition assay format were assembled similar to our previous studies [168]. Briefly, DGNPs decorated with anti-Tf antibodies were first added to the sample solution, and allowed to bind any Tf present in the sample to form DGNP/Tf complexes. To verify the detection limit of Tf with LFA, 30 μ L of running buffer, 15 μ L of a known amount of Tf in PBS, and 5 μ L of the DGNPs were mixed in a test tube. The LFA test strip was inserted vertically into the tube with the sample pad submerged in the sample, and the fluid wicked through the strip towards the absorbance pad. If Tf is present, the DGNP/Tf complexes moving through the LFA strip cannot bind to the Tf immobilized on the test line, indicating a positive

result with the presence of a single band at the control line. Alternatively, if Tf is not present, antibodies on DGNPs can bind to Tf on the test line. Since these probes exhibit a purplish red color, a visual band forms as the DGNPs accumulate at the test line, indicating a negative result. Regardless of the presence of Tf, the antibodies on DGNP will always bind to the secondary antibodies immobilized on the control line. A band at the control line signifies that the sample flowed completely through the strip, indicating a valid test. Therefore, a negative result is indicated by two bands: one at the test line and one at the control line. In contrast, a positive result is indicated by a single band at the control line. The LFA strips were imaged by a Canon EOS 1000D camera in a controlled lighting environment after 10 min.

8.2.5.2 Detection of Tf with the 3-D paper well

The LFA component of the paper-based device was slightly modified from the aforementioned setup. Specifically, the cellulose sample pad was replaced with a 5 x 20 mm fiberglass paper, which connected a nitrocellulose membrane containing the test and control lines. At the beginning of the sample pad, a 3-D paper well composed of multiple strips of fiberglass paper were used. For experiments using the 1:1 volume ratio ATPS, the well was composed of only five (four 5 x 7 mm strips plus the bottom sample pad) layers of fiberglass paper. To start the test, 40 μL of the mixed 1:1 volume ratio ATPS containing a known concentration of Tf were added to the paper well, followed by the addition of 50 μL of running buffer. Images were captured after 10 min. For experiments using the 9:1 volume ratio ATPS, 20 layers of paper (nineteen 5 x 7 mm strips plus the bottom sample pad) were used to form the paper well. 200 μL of the mixed 9:1 volume ratio ATPS containing a known concentration of Tf were added to the paper well, and allowed to incubate for 10 min, followed by the addition of

100 μ L of running buffer. After another 10 min, images were captured by a Canon EOS 1000D camera in a controlled lighting environment.

8.3 Results and Discussion

8.3.1 Visualization of ATPS

We hypothesized that the integration of ATPS with LFA could significantly improve the detection limit of a traditional LFA test without sacrificing its advantages. To achieve this, it was first necessary to identify an ATPS whose phases could be visualized as it flowed through the paper membrane. Specifically, we used a PEG-salt ATPS, which forms a more hydrophobic, PEG-rich phase on top and a more dense and hydrophilic, PEG-poor phase on bottom. Biomolecule partitioning in the ATPS is primarily dictated by relative hydrophilicity (since biomolecules tend to prefer the phase in which they experience the greatest attractive interactions) and size (since large biomolecules typically do not remain in the PEG-rich phase due to experiencing greater steric excluded-volume repulsive interactions with the greater number of PEG molecules in the PEG-rich phase). Brilliant Blue FCF dye was added to the mixed ATPS, and because it is small and hydrophobic, the dye partitioned extremely into the PEG-rich phase. Purple dextran-coated gold nanoparticles were also added to the mixed ATPS, and partitioned extremely into the PEG-poor phase because they are large (~50 nm diameter as measured by dynamic light scattering) and hydrophilic. Images of a 1:1 volume ratio ATPS and of a 9:1 volume ratio ATPS were taken before and after phase separation (Fig. 8.1). The amounts of Brilliant Blue FCF and dextran-coated gold nanoparticles were held constant between the 1:1 and the 9:1 volume ratio ATPSs. As a result, after phase separation, the top phase of the 9:1 volume ratio ATPS was greater in volume and therefore less concentrated with blue dye

compared to the top phase of the 1:1 volume ratio ATPS. Additionally, the bottom phase of the 9:1 volume ratio ATPS was much smaller in volume and displayed a darker shade of purple than that of the 1:1 volume ratio ATPS, demonstrating that shrinking the bottom phase can effectively concentrate the dextran-coated gold nanoparticles within the ATPS. As shown previously, we expected the 9:1 volume ratio ATPS sample to concentrate the nanoparticles by 10-fold since the volume of the bottom phase becomes 1/10 the volume of the total sample solution. Note that, as the volume ratios become more extreme, greater concentration-fold improvements are attainable but the system also requires more time to separate.

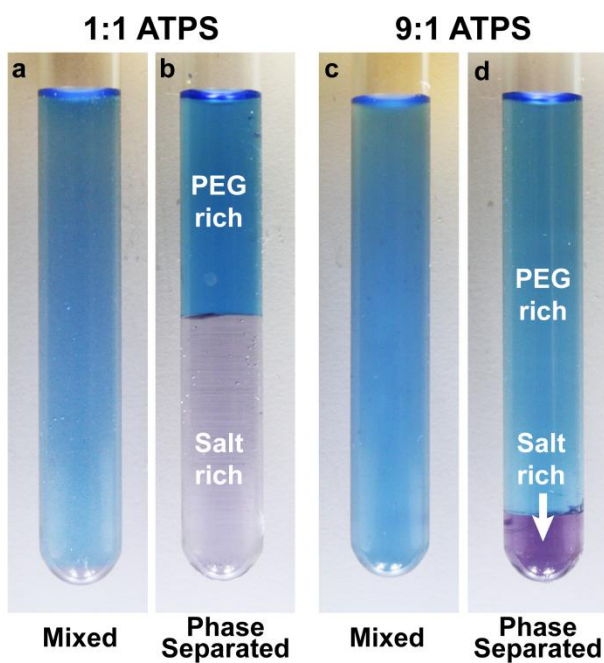


Figure 8.1. Brilliant Blue FCF dye and dextran-coated gold nanoparticles partition extremely to the upper PEG-rich and lower PEG-poor phases, respectively. (a) At 25 °C, a mixed 1:1 volume ratio ATPS phase separated to form (b) two equal volume phases. (c) At 25 °C, a mixed 9:1 volume ratio ATPS phase separated into (d) a larger PEG-rich phase and a smaller PEG-poor phase. The same amounts of Brilliant Blue FCF and dextran-coated gold nanoparticles were added to both ATPSs. The darker purple color of the 9:1 volume ratio ATPS indicates the increased gold nanoparticle concentration in the bottom PEG-poor phase.

8.3.2 Visualization of ATPS in Paper

After adding a mixed ATPS onto the paper membrane, the PEG-poor phase containing the purple dextran-coated gold nanoparticles was observed to flow quickly through the paper. Meanwhile, the PEG-rich phase containing the blue dye was retained at the beginning of the paper membrane (Fig. 8.2). This result was similar to the case in which both phases of the ATPS were allowed to fully separate inside a glass well before flow through the paper was triggered. The enhanced phase separation occurring within the paper membrane was apparent when using the 1:1 volume ratio ATPS (Fig. 8.2a), and the 1:1 volume ratio ATPS phase separated almost immediately. One possible explanation of this behavior is that the PEG-rich domains experience more interactions with the paper, making them less mobile. Furthermore, the PEG-rich domains are also more viscous and thus may experience greater difficulty traveling through the tortuous paper network. In contrast, the PEG-poor domains interact less with the paper and are less viscous, allowing them to travel quickly through the paper network and coalesce at the leading front. For the 9:1 volume ratio ATPS, the PEG-poor domains comprised only one-tenth of the total volume, making it more difficult for them to coalesce and flow ahead of the PEG-rich domains. Specifically, the time required for macroscopic phase separation to occur in paper was longer than the time it took for the fluid to wick the paper, and a good separation was not observed (Fig. 8.2b).

When using both the 1:1 and 9:1 volume ratio ATPSs, it was also observed that some PEG-poor domains did not make it to the leading front of flow. This indicated that not all of the PEG-poor domains were able to escape from the PEG-rich domains and explained why the equilibrium volume ratio measured in the test tube did not match the wicking distance ratio on the paper membrane. In order to improve LFA, most of the PEG-poor domains needed to reach

the macroscopic PEG-poor phase and separate from the macroscopic PEG-rich phase before reaching the detection zone. Therefore, an additional component was required to further improve the phase separation phenomenon.

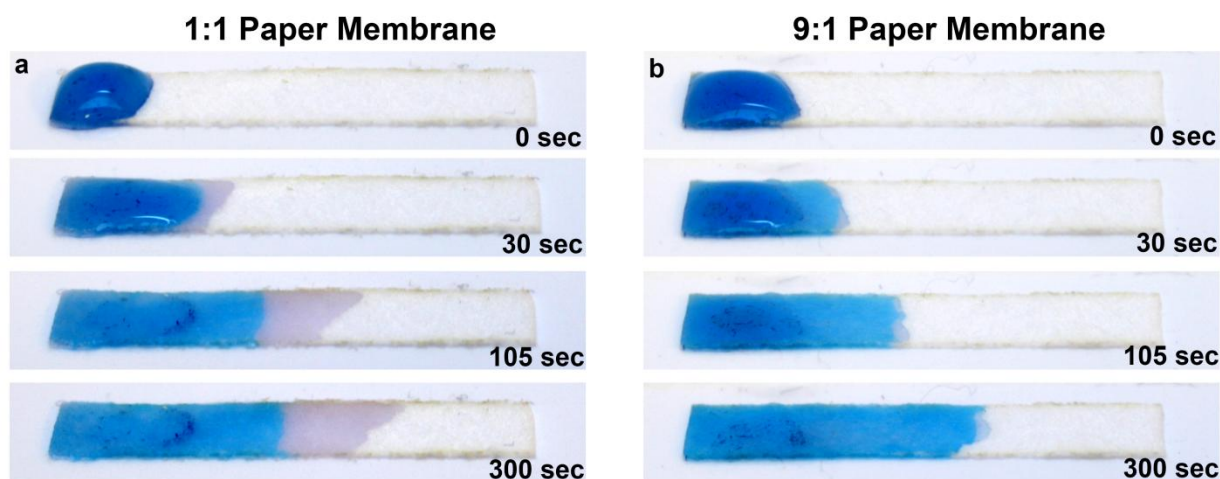


Figure 8.2. The paper membrane allows for ATPS phase separation to occur as it flows. The PEG-rich domains were retained near the beginning of the paper membrane while the PEG-poor domains moved quickly to the leading front. (a) The 1:1 volume ratio ATPS phase separated and flowed through the paper membrane within 5 min. (b) The 9:1 volume ratio ATPS also separated and flowed through the membrane within 5 min, but the phase separation was less efficient as the leading front is less distinct at 300 sec.

8.3.3 Visualization of ATPS in the 3-D Paper Well Device

A paper well that takes advantage of 3-D paper architectures was designed to further enhance the phase separation behavior. Using a 3-D paper well allows gravitational forces, which normally drive phase separation in test tubes, to also aid in ATPS phase separation within the paper. The 3-D paper architecture also increases the cross-sectional area normal to the direction of flow. More volume can therefore wick through the paper at the same time, allowing more PEG-rich domains to be held back by their interactions with the paper and the PEG-poor domains to coalesce more easily. We show in Fig. 8.3 that the 3-D paper well contributed to greater phase separation efficiency over the 2-D paper membrane shown previously. The PEG-

rich domains were retained in the top layers of the paper well while the PEG-poor domains containing the concentrated dextran-coated gold nanoparticles flowed towards the bottom layers of the paper well. Additionally, the PEG-poor domains were the first to leave the paper well and were effectively separated from the PEG-rich domains. A running buffer was also added to further drive fluid flow and to help flush any remaining PEG-poor domains through the paper well, and we envision that this addition can be automated in the future. Note that flow was slower when using the 9:1 volume ratio ATPS (the solution does not reach the end of the strip after 390 sec) since there was a greater volume of the more viscous PEG-rich phase.

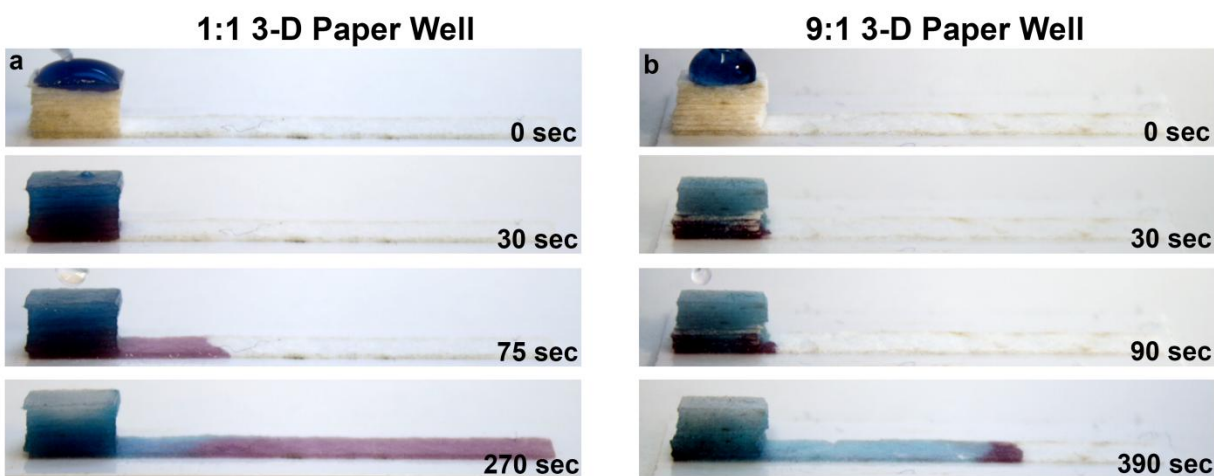


Figure 8.3. The 3-D paper well allows for further enhanced ATPS phase separation. Following the addition of a mixed ATPS with dyes, the PEG-rich domains were retained in the upper layers of the well while the PEG-poor domains containing the concentrated gold nanoparticles flowed quickly to the bottom layers. (a) The 1:1 volume ratio ATPS showed enhanced phase separation in the 3-D paper well and the PEG-poor phase flowed through the membrane within 5 min. (b) The 9:1 volume ratio ATPS also has improved phase separation and the PEG-poor phase was clearly visible. In contrast to Fig. 9.2, the leading front is well defined and has a dark purple color, signifying concentration of the dextran-coated gold nanoparticles.

8.3.4 Detection of Tf using the 3-D Paper Well Device

After visualizing the improved ATPS phase separation and flow behavior within the 3-D

paper well device, we integrated this technology with LFA to create an all-in-one device with improved sensitivity over traditional LFA. The Brilliant Blue FCF dye was no longer used, and functionalized anti-Tf DGNPs were used in place of the dextran-coated gold nanoparticles. The DGNPs partition similarly to the dextran-coated gold nanoparticles in the ATPS, but can also capture target biomarkers in the sample and act as the colorimetric indicator for LFA. Since the DGNPs partition extremely into the bottom, PEG-poor phase, a 1:1 volume ratio should yield a 2-fold concentration of the DGNPs as they collect in one-half of the original volume. To determine if this was indeed the case, we decided to apply the same amount of DGNPs to the ATPS solutions with Tf concentrations that were 2 times lower than the LFA only case. Since we had an idea of the number of Tf molecules required to saturate the antibodies, we increased the sample volume 2-fold to keep the total number of Tf molecules the same. Because only a limited volume can pass through the detection zone before LFA is saturated with liquid, only a small portion of the target captured DGNPs would pass through the LFA detection zone. Therefore, it was necessary to concentrate the DGNPs to the leading front of flow before the LFA strip became fully saturated. Since only the bottom phase of the 1:1 volume ratio ATPS containing the DGNPs should pass through the detection zone, the device's volume processing capacity was fine-tuned by varying the number of layers comprising the 3-D paper well. To accommodate this increase in sample volume, the 3-D paper well used for the detection of Tf within a 1:1 volume ratio ATPS solution was composed of 5 layers of paper. To demonstrate 10-fold concentration, the sample volume was analogously increased 10-fold and a 9:1 volume ratio ATPS solution was used. The well used for the 9:1 volume ratio ATPS solution was increased to 20 layers of paper (Fig. 8.4) to accommodate the increased volume. Despite the significant increase in the number of layers, the 3-D paper well for the 9:1 volume ratio ATPS still remained relatively small in

comparison to a dime.

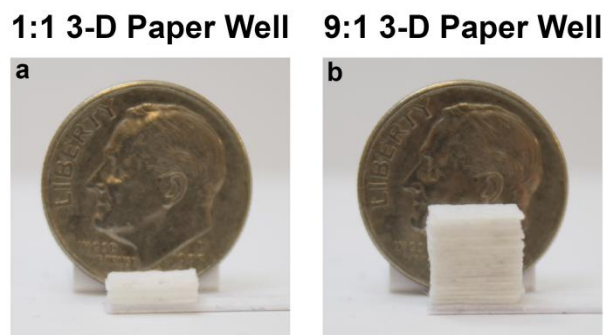


Figure 8.4. Different sizes of 3-D paper wells allow for the processing of varied sample volumes. (a) The paper well for the 1:1 volume ratio ATPS was composed of 5 fiberglass membranes. (b) The paper well for the 9:1 volume ratio ATPS was composed of 20 fiberglass membranes.

When the ATPS solution containing DGNPs was added to the paper well, the DGNPs concentrated rapidly to the leading front of the solution as they wicked through our device. The DGNPs reached the detection region of the device before the remainder of the solution that was retained in the paper well. For the competition assay, the presence of the test line indicates a negative result, whereas the absence of the test line indicates a positive result. When using the negative control which does not contain the model protein Tf, in less than 25 min, both setups using the 1:1 and 9:1 volume ratio ATPSs rendered a visible band at both the test and control lines, respectively, indicating the absence of Tf and a valid test (Fig. 8.5).

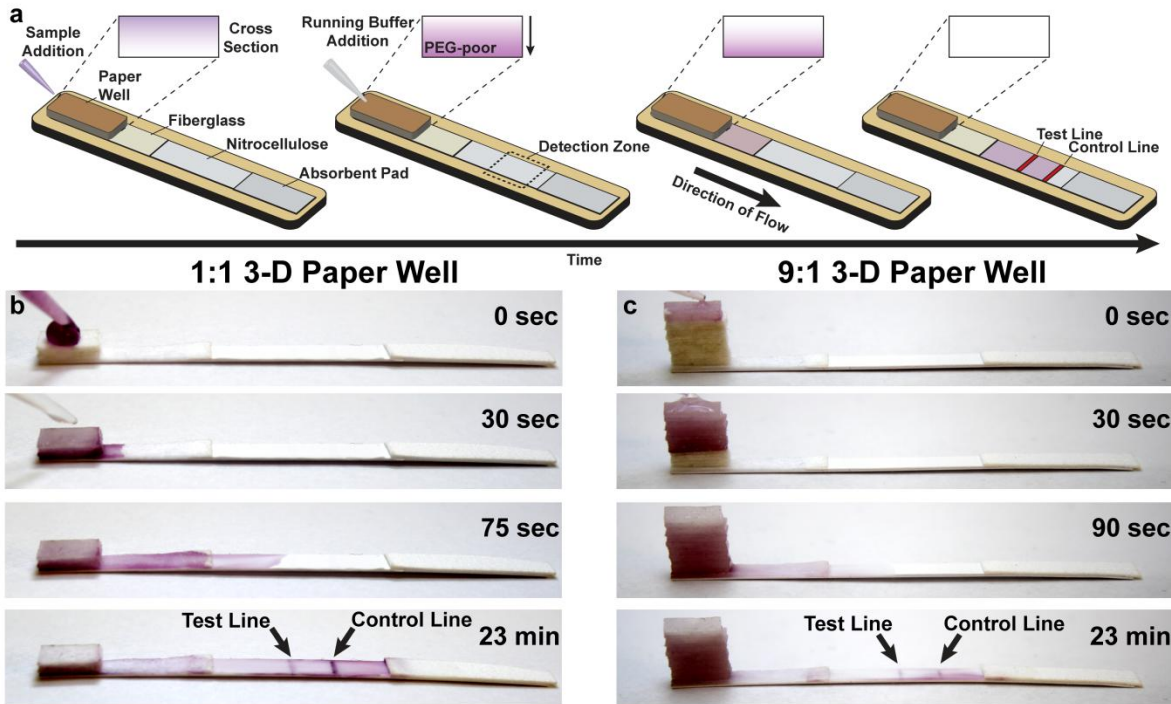


Figure 8.5. The 3-D paper well was combined with ATPS and LFA for Tf detection. (a) The paper well device was combined with the Tf competition assay on nitrocellulose paper. Samples containing no Tf were correctly diagnosed when using the 1:1 (b) or 9:1 (c) volume ratio ATPS solutions with visible test and control lines.

After verifying that the 3-D paper well can be combined with LFA to accurately assess the absence of Tf in negative control ATPS samples, the Tf concentrations were varied to find the detection limits when using the 1:1 and 9:1 volume ratio ATPS solutions. As predicted, these experiments demonstrated 2-fold and 10-fold improvements in the detection limit of Tf over conventional LFA, respectively (Fig. 8.6). For the 9:1 volume ratio ATPS experiments with the 3-D paper well, the sample was allowed to incubate within the device for an additional 10 min to allow ample time for the DGNPs to capture the target protein and phase separate macroscopically before addition of the running buffer. Note that this incubation period was not required for the 1:1 volume ratio ATPS because the DGNPs were more concentrated in the mixed ATPS, making it easier to sample the entire solution. The results of these experiments

showed that, while conventional LFA detected Tf at concentrations of 1 ng/uL (concentration at which no test line appears), our 3-D paper-based diagnostic device was capable of detecting Tf at 0.5 ng/uL (2-fold improvement in the detection limit) when the 1:1 volume ratio ATPS was used. Similarly, the 3-D paper-based diagnostic device was capable of detecting Tf at 0.1 ng/uL (10-fold improvement in the detection limit) when the 9:1 volume ratio ATPS was used. These results suggest that an ATPS solution with the desired volume ratio can be combined with an appropriately sized 3-D paper well to significantly and predictably improve the biomarker detection using LFA.

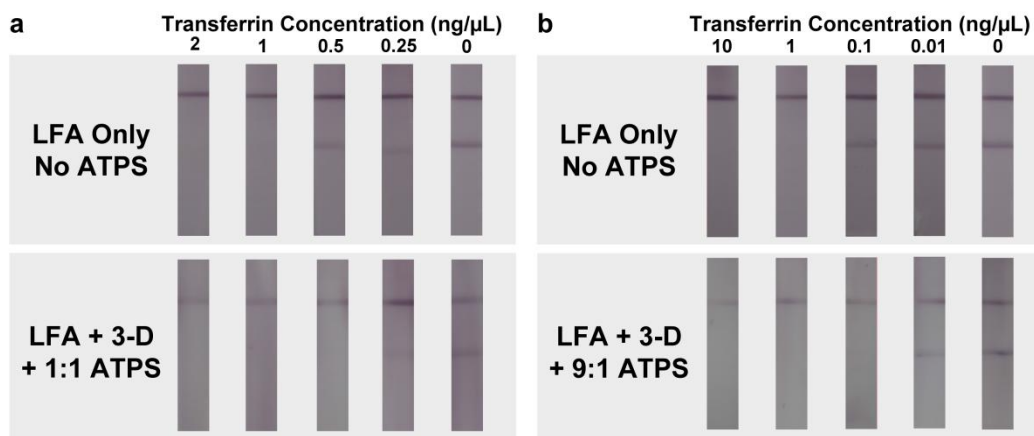


Figure 8.6. The 1:1 volume ratio ATPS with the 3-D paper well allows for a 2-fold improvement in the detection limit of Tf while the 9:1 volume ratio ATPS allows for a 10-fold improvement. (a) Conventional LFA detected Tf at 1 ng/μL but could not detect at 0.5 ng/μL, resulting in a false negative. A 1:1 volume ratio ATPS with the 3-D paper well successfully detected Tf at 0.5 ng/μL. (b) Conventional LFA detected Tf at 1 ng/μL but could not detect at 0.1 ng/μL, resulting in a false negative. A 9:1 volume ratio ATPS with the 3-D paper well successfully detected Tf at 0.1 ng/μL.

8.4 Conclusion

In the current study, we have demonstrated that our 3-D paper-based diagnostic device allows for the direct addition of an ATPS and results in a 10-fold improvement in the detection limit of a model protein Tf. A mixed ATPS applied directly to the paper membrane rapidly phase

separates as it flows through the device, simultaneously allowing biomarker concentration and downstream detection with a reduced time-to-result. Although the precise mechanism for enhanced ATPS phase separation in paper still requires further investigation, we have shown that the paper speeds up the ATPS phase separation behavior and that 3-D paper architectures can further enhance this phenomenon in ways that a simple 2-D structure cannot accomplish. Expanding into the vertical dimension with the paper well enables processing of larger sample volumes and allows gravitational forces to aid in the phase separation, while the multiple layers of fiberglass membrane provide a greater cross-sectional area through which the domains of the ATPS can interact. In the future, we are interested in studying this phase separation in paper phenomenon by determining the fundamental principles of the paper that drive this action.

Our 3-D paper diagnostic is the first to demonstrate ATPS phase separation in paper, allowing for concentration of the target analyte as the sample flows through the paper to the downstream detection zone. This implementation improves the sensitivity of conventional LFA devices while maintaining ease-of-use and time-to-result. With 10-fold improvements in detection limit, our device has the potential to rapidly identify pathogens at lower concentrations that were previously undetectable with conventional LFA. This robust and portable device requires no electricity or sophisticated laboratory equipment and is ideal for POC applications in resource-poor settings. The 3-D paper architecture can also easily be applied to existing commercial LFA products, transforming them to next-generation rapid diagnostics without inheriting the poor sensitivity characteristic of conventional LFA. Once fully developed, this platform technology has the potential to revolutionize the state of health care in resource-poor settings by providing rapid, accurate, and inexpensive diagnostics, leading to improved patient management, treatment, and outbreak prevention.

Chapter 9: Other approaches to integrating the aqueous two-phase concentration system with the lateral-flow detection assay

9.1 Overview

Two additional approaches were investigated for integrating the aqueous two-phase system (ATPS) with the lateral-flow immunoassay (LFA) for improving the sensitivity of LFA. The first approach utilized magnets to collect magnetic nanoprobess that could capture target proteins from ATPS solutions. The second approach utilized a newly discovered phenomenon in which the surface chemistry of nanoprobess were manipulated so that they could partition to the solid-liquid interface between the ATPS and a polypropylene surface, allowing for rapid and easy collection without using syringes or magnets.

9.2 Motivation and background

9.2.1 Magnetic nanoparticles with ATPS and LFA

Antibody-decorated magnetic particles have long been utilized to capture and concentrate target biomolecules. These approaches were effective, since once the target biomolecules were captured by the magnetic particles, they could be collected rapidly and easily using a magnet or an external magnetic field. Mirkin's group has utilized a nanoparticle-based bar-code system to capture and detect prostate-specific antigen at attomolar concentrations [221]. While this system enabled the detection of a target protein with high sensitivity, lab-based equipment was required, specifically a bulky magnetic separator and a polymerase chain reaction machine. Alternatively, Knopp's group developed an LFA system using gold-coated magnetic particles for the detection

of aflatoxin, although no magnet or magnetic force was utilized in that study to further concentrate the target [222]. While no reasons were provided by the authors to avoid the obvious use of a magnet to further enhance the assay, it was speculated that in order to recover the magnetic nanoparticles efficiently, the size of the magnetic nanoparticles needed to be large enough to be responsive to the magnetic field. However, if the size of the particle is too large, the particles may experience difficulties traveling through the LFA test strip, as suggested by the inconsistent flows shown in their LFA images.

To address this problem, we utilized ATPSs in conjunction with gold-coated magnetic nanoprobe (GMPs) to first capture target biomolecules in a sample solution. To avoid using an expensive and bulky magnet to collect the particles in the solution or large nanoprobe that could respond to a weaker magnetic field, the ATPS was used to first passively concentrate GMPs into a small volume in one of the two bulk phases of ATPS. Subsequently, an inexpensive and portable magnet was used to rapidly recover the GMPs and the captured biomolecules. Since the gold coating on the GMPs also acts as a colorimetric indicator for LFA, the GMPs were directly applied to the LFA strips.

In addition to using an ATPS to improve the magnetic extraction of the GMPs, it was found that the phase separation of the ATPS benefited from the use of GMPs and magnetic forces. Specifically, the PEG-salt ATPS used in our previous studies phase separated completely in the order of hours. Although we showed that the extraction of the concentrated sample can occur before the system reaches equilibrium since the concentration of the nanoprobe in the bottom, PEG-poor phase remains constant as a result of minimal entrainment of the PEG-rich domains in the macroscopic PEG-poor phase, 30 min were still required to achieve a sufficient

volume of the bottom phase to be extracted for the subsequent LFA. Alternatively, GMPs in the ATPS partitioned extremely and almost instantly to the PEG-poor domains as phase separation was triggered. The PEG-poor domains containing GMPs could find each other and coalesce more easily with the presence of magnetic forces, possibly due to the GMPs dragging the PEG-poor domains with them as they responded to the magnetic field. This force, along with the gravitational force, further facilitated the coalescing of PEG-poor domains, thus leading to an accelerated phase separation and yielding a sufficient volume of the bottom phase for extraction within only 10 min.

In this study, we first prepared GMPs that were small enough to travel through the LFA test strips without flow problems. These GMPs were then used to capture a model protein, transferrin (Tf), in a PEG-salt ATPS solution that yielded a 9:1 (top phase : bottom phase) volume ratio. A small magnet (1/8" diameter x 1/32" thick) was placed into the solution to accelerate phase separation. The GMPs and the captured proteins were recovered after 10 min, the small magnet was removed, and the GMP-Tf complexes were applied directly to LFA for detection.

9.2.2 Solid-Liquid Interface Extraction

While the aforementioned approach effectively concentrated and detected Tf using the ATPS with magnetic nanoprobe, a small magnet was still required. The following approach explored the possibility of extracting the target-nanoprobe complexes without using an external magnetic field, but instead by taking advantage of a new phenomenon we discovered. Specifically, the surface chemistry of PEGylated gold nanoprobe (PGNPs) could be

manipulated to partition extremely to a solid-liquid interface between the ATPS and a polypropylene (PP) surface. This unique phenomenon was found to be ATPS-specific, as the PGNPs did not partition to the solid-liquid interface when aqueous solutions comprised of only polymer or salt were used. Moreover, this phenomenon was also found to be material-specific, as the PGNPs would partition extremely to a polypropylene (PP) surface in our ATPS, but not to a glass surface.

To facilitate the collection of the target-PGNP complexes at the PP-ATPS solid-liquid interface, PGNPs decorated with anti-Tf antibodies were added to an ATPS solution containing Tf, followed by submerging a commercially available PP straw into the ATPS. The PGNPs first captured the target proteins in the ATPS and then preferentially partitioned to the PP surface. After 10 min, the PP straw was removed from the ATPS with a significant amount of protein-GNP complexes still adsorbed to the surface. This effectively eliminated the need to manually extract the concentrated Tf-PGNPs using syringes.

In this study, we first prepared PGNPs that could partition to the PP-liquid interface in an ATPS. These PGNPs were then used to capture Tf in a PEG-salt ATPS solution that yielded a 1:1 volume ratio. A PP straw was submerged into the ATPS solution, and the PGNPs and the captured proteins were recovered after 10 min by pulling the straw from the solution. The PGNP-Tf complexes on the straw were washed with a running buffer and applied directly to LFA for detection. Due to the minimal volume associated with the PP-ATPS interface and the small volume required to wash the PGNPs off the straw, the PGNPs were concentrated extremely, and we were able to improve the detection limit of Tf in LFA by 50-fold.

9.3 Materials and Methods

9.3.1 Preparing LFA test strips

The LFA test utilizing the competition mechanism was implemented. In the competition assay, the target of interest is immobilized on a nitrocellulose membrane to form the test line. Immobilized secondary antibodies against the primary antibodies on the nanoprobe (GMPs or PGNPs) make up the control line. In LFA, when the sample first comes in contact with the nanoprobe, if the target molecules are present in the sample, they will bind to their specific antibodies decorated on the nanoprobe. If the target molecules present in the sample saturate the antibodies on the nanoprobe, these nanoprobe can no longer bind to the immobilized target molecules on the test strip. As a result, the nanoprobe do not form a visual band at the test line, and this indicates a positive result. On the other hand, if the sample does not contain the target molecules at a concentration that can saturate the antibodies on the nanoprobe, these antibodies on the nanoprobe can bind to the immobilized target molecules on the test strip and form a visual band at the test line. This indicates a negative result. Furthermore, regardless of the presence of the target molecule in the sample, the antibodies on the nanoprobe will bind to the immobilized secondary antibodies on the control line, indicating that sufficient sample has wicked through the test line and reached the control line. The presence of the visible control line indicates a valid test.

9.3.2 Preparing GMPs

Iron oxide magnet nanoparticles with a diameter of 50 nm were purchased from Chemicell (Berlin, Germany). These particles were coated with gold using a protocol modified

from Sim and coworkers [223]. Briefly, iron oxide particles were diluted in 0.01 M sodium citrate and stirred for 10 min. Subsequently, 4 additions of 1% w/v gold chloride solution were applied to the iron oxide nanoparticle solution with stirring in 10 min intervals. The solution changed from black to maroon after the additions of gold chloride. The gold-coated magnetic nanoparticles were then recovered using a magnet. Anti-Tf gold-coated magnetic nanoprobe (GMPs) were prepared with the same conjugation procedures as those described in the previous chapters.

9.3.3 Developing the magnetic collection device

The collection device was constructed by placing a small Neodymium magnet (1/8" diameter x 1/32" thick, KJ Magnetics, Philadelphia, PA) at the tip of a drinking straw. The magnet was wrapped by Parafilm to prevent direct contact with GMPs in solution.

9.3.4 Partitioning GMPs in ATPS

To see if the GMPs would partition extremely into the bottom, PEG-poor phase of the PEG-salt ATPS, 30 μ L of the GMPs were added to a 2 mL ATPS solution that yielded a 9:1 volume ratio. To see if the presence of the magnet would accelerate phase separation, the partitioning experiments were performed with or without the magnetic collection device. The volume of the bottom phase was measured for each experiment at 10 min and 30 min.

9.3.5 Combining the GMPs, magnetic collection device, ATPS, and LFA

We then investigated if the GMPs could be incorporated with ATPS and LFA. First, 2 mL of 9:1 ATPS solutions spiked with various concentrations of Tf were prepared. 30 μ L of GMPs were applied to each solution, followed by the addition of the magnetic collection device. The solutions were placed in a 25°C water bath and incubated for 10 min. After the incubation period, the collection device was removed from the solution and transferred to a tube that contained 50 μ L of running buffer. The small magnet was removed from the straw and the GMPs collected on the straw were washed off by shaking the straw in the running buffer for a few seconds. The straw was then removed and an LFA test strip was dipped into the running buffer containing the collected GMPs. After 10 min, the test strip was removed from the tube and an image of the test strip was taken using a Canon EOS 1000D camera (Canon U.S.A., Inc., Lake Success, NY).

9.3.6 Preparing PGNPs

The naked gold nanoparticles were prepared using a protocol described by Frens [68], resulting in a clear, cherry-colored solution with particle sizes around 25-30 nm in diameter. To prepare the PGNPs, 320 mg of goat anti-Tf antibody was incubated with 20 mL of a colloidal gold solution for 30 min, followed by the addition of thiolated-PEG₂₀₀₀ using a molar ratio of 5000:1 for PEG:NP and an additional incubation of 30 min. To prevent nonspecific binding of other proteins to the surfaces of the colloidal gold, 2 mL of a 10% bovine serum albumin (BSA) solution was added to the mixture and mixed for an additional 15 min. The resulting solution was gently mixed on a shaker during the incubation period. To remove free unbound antibodies, PEG,

and BSA, the mixture was subsequently centrifuged for 30 min at 4°C and 9,000 g. The pellet of PGNPs was washed with a 1% BSA solution, and this washing step was repeated twice. Finally, the recovered PGNPs were resuspended in 3 mL of a 0.1 M sodium borate buffer at pH 9.0.

9.3.7 Combining the PGNPs, PP straw, ATPS, and LFA

PEG-salt ATPS solutions that yielded a 1:1 volume ratio and contained varying Tf concentrations were first prepared in glass tubes. 5 μL of the GNP solution were added to the Tf-ATPS solution with a final volume of 1 mL. The ATPS solutions were well mixed, and a PP straw was inserted into each ATPS solution. The solutions were then incubated for 15 min at 25°C. For each mixture, the PP straw was removed carefully from the ATPS solution. Assuming that the total volume of the PP-ATPS interface was approximately 1 μL , 49 μL of test buffer was used to wash adsorbed Tf-GNP complexes from the portion of the straw that was immersed in the ATPS solution to achieve a total volume of 50 μL . Both the inner and outer surfaces of the straw were washed for a total of 10 seconds. LFA test strips were then dipped vertically so that the sample pads came in contact with the mixtures. The strips were taken out of the mixtures after 10 minutes, and images of the test strips were taken immediately using a Canon EOS 1000D camera (Canon, U.S.A., Inc., Lake Success, NY).

9.4 Results and Discussion

We proposed two approaches in this chapter that allowed us to expand the capabilities of combining the ATPS with LFA: concentrating the nanoparticles with a magnetic field and with a solid-liquid interface.

9.4.1 Magnetic nanoparticles with ATPS and LFA

In the first approach, a rapid, portable diagnostic system was developed utilizing gold-coated magnetic nanoprobcs. While magnetic particles have been used in many applications to concentrate and detect biomolecules, we are the first one to develop a diagnostic system that does not require any lab-based equipment to collect the particles and interpret signals generated by these particles. The GMPs developed in this study achieved the following four functions: (1) capture the target protein in the sample; (2) partition extremely into one of the bulk phases of an ATPS; (3) be collected by an inexpensive, portable magnet; and (4) serve directly as the colorimetric indicator for LFA after being extracted and applied to the LFA paper strip. Functions (2) and (3) were demonstrated by placing the GMPs in our PEG-salt ATPS solution. As shown in Figure 9.1A, it was observed that the GMPs partitioned extremely into the bottom, PEG-poor phase due to the repulsive, steric, excluded-volume interactions that operate between the GMPs and the greater number of PEG molecules in the PEG-rich phase. This allowed the GMPs to concentrate into a small volume, which enabled their collection with a much smaller and lighter magnet (Fig. 9.1B) Moreover, since these GMPs were highly responsive when they were in close proximity to the magnet, the particles could be rapidly recovered and transferred for subsequent detection (Fig. 9.1C). Last but not least, by using this approach, the GMPs could be collected into a very small volume, which enabled the extreme concentration of the target protein.

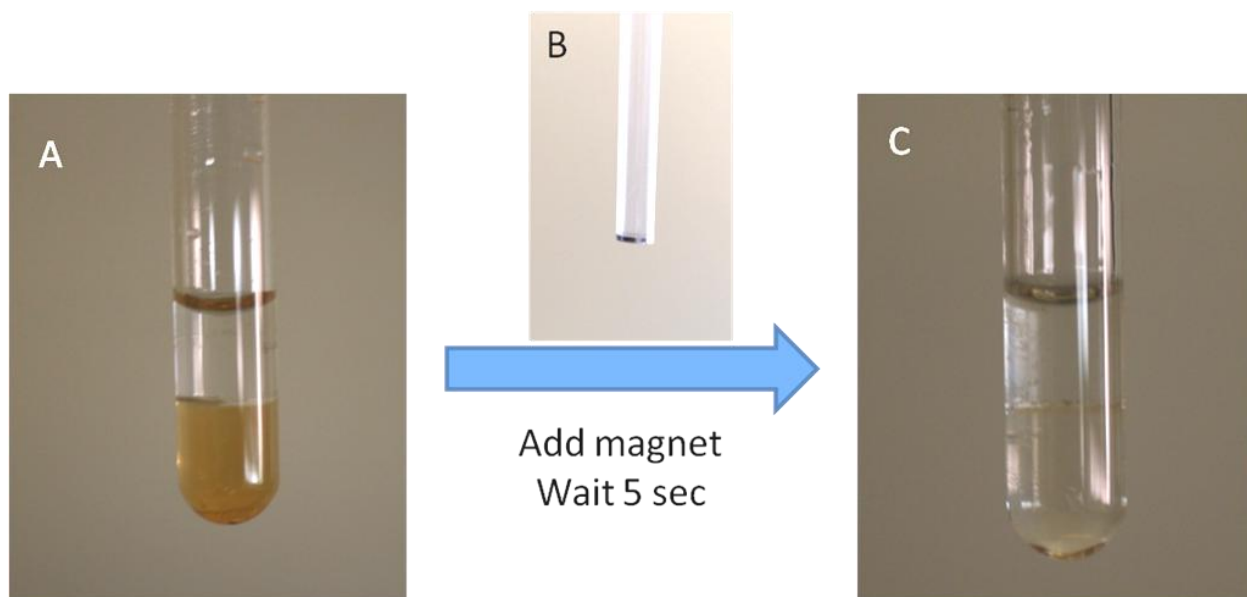


Figure 9.1. (A) GMPs were found to partition extremely into the bottom, PEG-poor phase. This allowed the use of a small magnet (B) to rapidly recover most GMPs from the ATPS solution (C).

To collect these GMPs more effectively, a simple collection device was made by placing a small magnet at the tip of a plastic straw. Parafilm was wrapped around the tip so the collected GMPs would not make direct contact with the magnet. This collection device was then submerged into a 9:1 PEG-salt ATPS solution, which contained the GMPs. It was found that most of the GMPs were collected by the magnet within 10 min, indicated by a clear solution with most of the GMPs gathering around the magnet. It was also interesting to see that the presence of the magnet accelerated phase separation. From our previous studies, it would take at least 30 min for a sufficient amount of the bottom phase to form for extraction. With the presence of a magnet, a similar volume of the bottom phase was observed in only 10 min. We believe this accelerated phase separation is due to the additional magnetic field improving the coalescence of the PEG-poor domains. After phase separation was initiated, the GMPs partitioned extremely and rapidly into the PEG-poor domains. These domains coalesced and eventually descended due to the interfacial tension and density difference between the two phases. However, due to the smaller

volume associated with the PEG-poor domains in a 9:1 volume ratio ATPS, it was more difficult for these domains to coalesce. They also had to travel a farther distance through a more viscous PEG-rich macroscopic phase to reach the macroscopic bottom phase. With the presence of a magnet, the PEG-poor domains moved towards the magnet in addition to descending due to gravity. This additional force helped the PEG-poor domains find each other and coalesce much more easily, leading to an accelerated phase separation.

To see if the GMPs could improve the sensitivity of LFA when used in conjunction with ATPS, preliminary LFA studies with or without the prior concentration step were performed (Fig. 9.2).

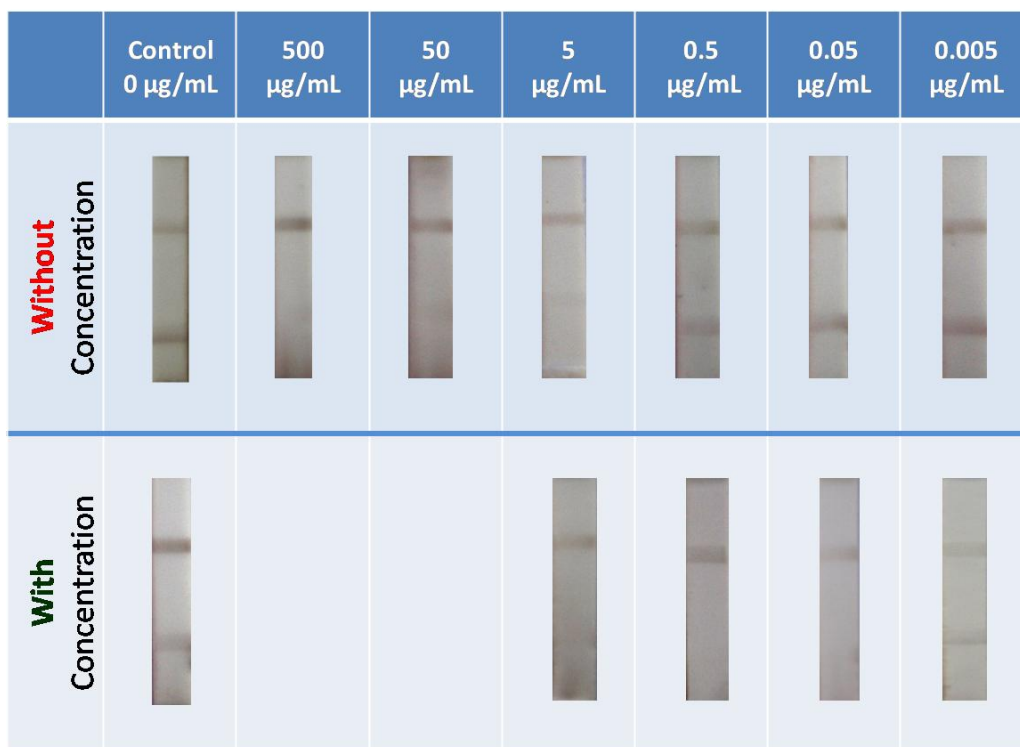


Figure 9.2. Images of LFA strips used to detect Tf (top) without and (bottom) with a prior ATPS concentration step.

9.4.2 Solid-Liquid Interface Extraction

The second approach to integrating ATPSs with LFA was to drive PEGylated gold nanoprobe (PGNPs) to the solid-liquid interface between the ATPS and a polypropylene (PP) solid. While similar to the first approach, this approach no longer required an external magnet. The exact mechanism is still under investigation, but we have discovered that an ATPS is required. As shown in Figures 9.3A and B, the PGNPs did not partition to the solid-liquid interface when a PEG-only or salt-only aqueous solution was used. Instead, the PGNPs appear to be dispersed evenly throughout each aqueous solution with no preference for the solid-liquid interface. Since the PGNPs were found to partition to the solid-liquid interface only in the presence of a phase-separated ATPS, an ATPS with a 1:1 volume ratio was used in this study since this ATPS phase separates the fastest when compared to ATPSs with other volume ratios. Figure 9.3C demonstrated the extreme partitioning behavior of the PGNPs on the PP straw after 10 min. The PP straw also allowed for the easy extraction of the concentrated target-PGNP complexes. After the straw was withdrawn, the collected PGNPs were easily washed off using a running buffer and applied directly to LFA (Fig. 9.3D).

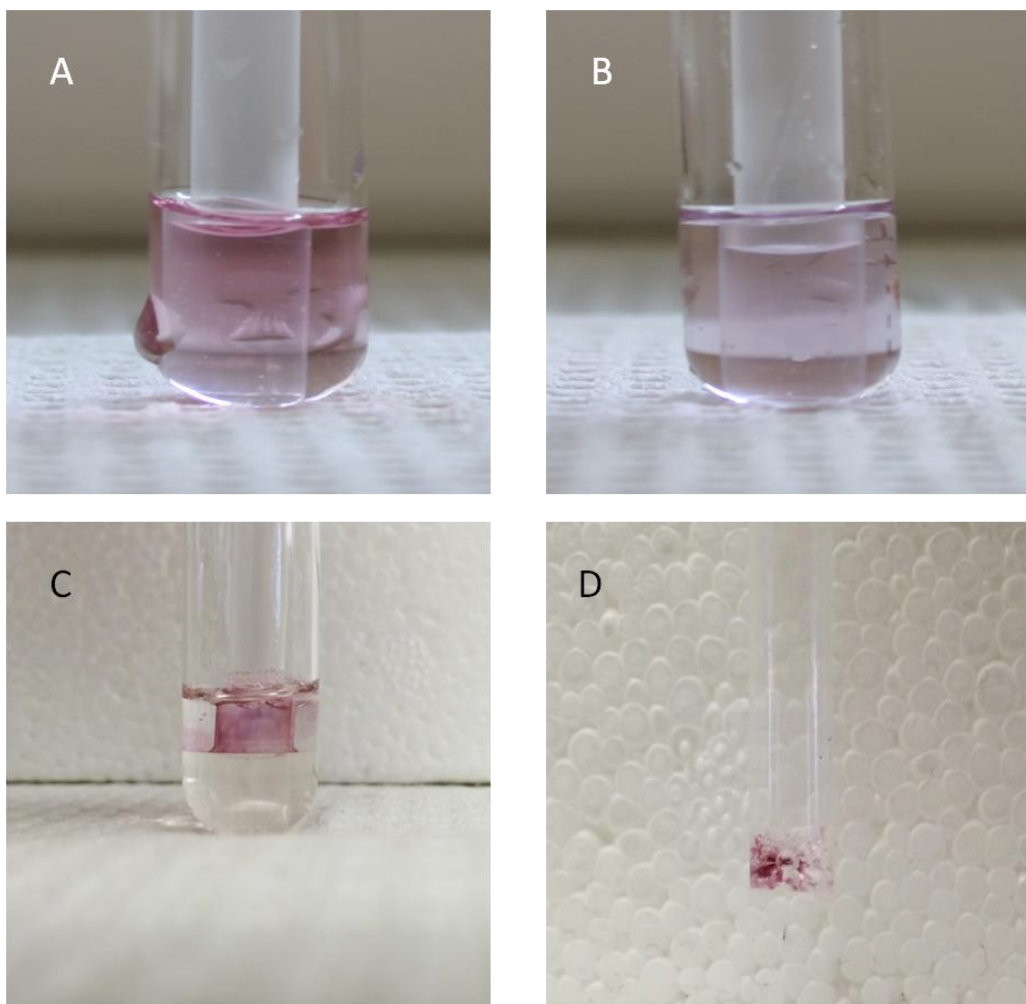


Figure 9.3. Images of PGNPs and the PP straw in a solution containing (A) PEG only, (B) salt only, or (C) a 1:1 ATPS. PGNPs only partitioned extremely to the PP straw in the presence of ATPS. (D) The PP straw was extracted from (C), and this figure shows that the straw can be withdrawn to easily collect the concentrated PGNPs for the subsequent detection assay.

The LFA results are shown in Figure 9.4. Each test showed the presence of a control line, which indicated that the fluid flowed completely through the strip and confirmed the validity of the test. For the negative control in which Tf was absent, a test line appeared and therefore indicated a true negative result. At a high Tf concentration (10 ng/ μ L), a test line did not appear and therefore indicated a true positive result. However, at lower Tf concentrations for the case without the prior concentration step, a visible test line appeared, suggesting that there was an

insufficient amount of Tf in the sample to saturate the antibodies decorated on PGNPs. Therefore, these tests indicated false negative results. The LFA results using this approach are shown in the upper panel (Fig. 9.4 top). Since false negative results appeared at 1 ng/ μ L in the LFA studies without prior concentration, this indicated that the detection limit of LFA for Tf was 10 ng/ μ L.

To improve the performance of LFA, the same amount of PGNPs that were used for a single LFA test were placed in an ATPS solution with a Tf concentration of 1 ng/ μ L. By increasing the volume of this ATPS solution by 50 times compared to the volume used in an LFA strip, the PGNPs could interact with 50 times more Tf and therefore could achieve a higher level of saturation. However, since the PGNPs were also diluted by 50 times, they needed to be concentrated and collected prior to detection. By placing a PP straw in the ATPS solution, the PGNPs partitioned extremely to the surface of the straw. After the ATPS solution was incubated at room temperature for 10 min, the PP straw was removed from the solution. Unlike other adsorption phenomena in which the substances on the solid surface are typically not recoverable, the PGNPs were retrieved easily by rinsing the straw with running buffer. This buffer containing the PGNPs was then applied to LFA directly. The LFA results using this approach are shown in the bottom panel (Fig. 9.4 bottom). Since 0.2 ng/ μ L is the lowest concentration that demonstrated a true positive result, the detection limit of LFA for Tf was improved from 10 ng/ μ L to 0.2 ng/ μ L, a 50-fold improvement.













	Negative Control	10 ng/ μ L	1 ng/ μ L	0.2 ng/ μ L	0.1 ng/ μ L	0.01 ng/ μ L
LFA only						
LFA + ATPS						

Figure 9.4. Images of LFA strips used to detect Tf (top) without and (bottom) with a prior ATPS concentration step.

9.5 Conclusions

This chapter describes two additional approaches that could be used to rapidly concentrate nanoprobe after they capture target biomolecules in an ATPS. These nanoprobe can subsequently be concentrated into a very small volume, either by using a portable magnet or by modifying the surface chemistry of the nanoprobe to enable solid-liquid interface extraction. The transfer of the concentrated nanoprobe to the subsequent LFA has also been improved by using a collection device, either a portable magnet or a PP straw. We are in the process of developing a portable device that utilizes these two approaches and enables a user to operate the assay with minimal steps (Fig. 9.5).

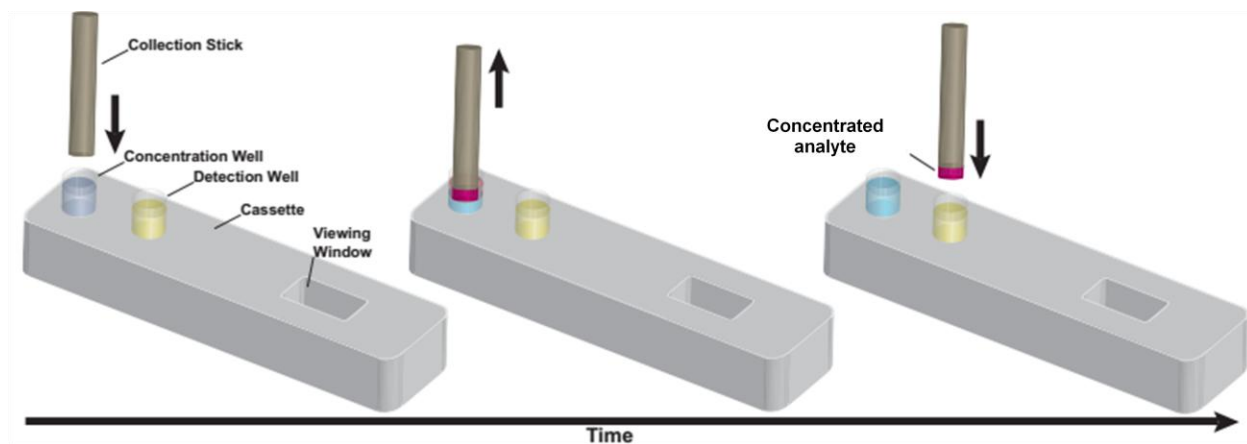


Figure 9.5. Schematic representation of the proposed portable device.

References

1. Zhang, L., et al., *Nanoparticles in medicine: therapeutic applications and developments*. Clinical pharmacology and therapeutics, 2008. **83**(5): p. 761-9.
2. Brannon-Peppas, L. and J.O. Blanchette, *Nanoparticle and targeted systems for cancer therapy*. Advanced drug delivery reviews, 2004. **56**(11): p. 1649-59.
3. Kawasaki, E.S. and A. Player, *Nanotechnology, nanomedicine, and the development of new, effective therapies for cancer*. Nanomedicine : nanotechnology, biology, and medicine, 2005. **1**(2): p. 101-9.
4. Farokhzad, O.C. and R. Langer, *Nanomedicine: developing smarter therapeutic and diagnostic modalities*. Advanced drug delivery reviews, 2006. **58**(14): p. 1456-9.
5. Ferrari, M., *Cancer nanotechnology: opportunities and challenges*. Nature reviews. Cancer, 2005. **5**(3): p. 161-71.
6. *Probability of Developing or Dying of Cancer Software, Version 6.3.0*. Statistical Research and Applications Branch, NCI, 2008.
7. *The state of cancer care in america, 2014: a report by the american society of clinical oncology*. Journal of oncology practice / American Society of Clinical Oncology, 2014. **10**(2): p. 119-42.
8. Kukowska-Latallo, J.F., et al., *Nanoparticle targeting of anticancer drug improves therapeutic response in animal model of human epithelial cancer*. Cancer research, 2005. **65**(12): p. 5317-24.
9. Malik, N., E.G. Evagorou, and R. Duncan, *Dendrimer-platinite: a novel approach to cancer chemotherapy*. Anti-cancer drugs, 1999. **10**(8): p. 767-76.
10. Swaminathan, S., et al., *Cyclodextrin-based nanosponges encapsulating camptothecin: physicochemical characterization, stability and cytotoxicity*. European journal of pharmaceutics and biopharmaceutics : official journal of Arbeitsgemeinschaft fur Pharmazeutische Verfahrenstechnik e.V, 2010. **74**(2): p. 193-201.
11. Hamaguchi, T., et al., *NK105, a paclitaxel-incorporating micellar nanoparticle formulation, can extend in vivo antitumour activity and reduce the neurotoxicity of paclitaxel*. British journal of cancer, 2005. **92**(7): p. 1240-6.
12. Markman, M., *Pegylated liposomal doxorubicin in the treatment of cancers of the breast and ovary*. Expert opinion on pharmacotherapy, 2006. **7**(11): p. 1469-74.
13. Rosenthal, E., et al., *Phase IV study of liposomal daunorubicin (DaunoXome) in AIDS-related Kaposi sarcoma*. American journal of clinical oncology, 2002. **25**(1): p. 57-9.
14. Rivera, E., *Current status of liposomal anthracycline therapy in metastatic breast cancer*. Clinical breast cancer, 2003. **4 Suppl 2**: p. S76-83.
15. Park, J.W., et al., *Anti-HER2 immunoliposomes: enhanced efficacy attributable to targeted delivery*. Clin Cancer Res, 2002. **8**(4): p. 1172-81.
16. Gibson, J.D., B.P. Khanal, and E.R. Zubarev, *Paclitaxel-functionalized gold nanoparticles*. Journal of the American Chemical Society, 2007. **129**(37): p. 11653-61.
17. Paciotti, G.F., et al., *Colloidal gold: a novel nanoparticle vector for tumor directed drug delivery*. Drug delivery, 2004. **11**(3): p. 169-83.
18. Maeda, H., et al., *Tumor vascular permeability and the EPR effect in macromolecular therapeutics: a review*. J Control Release, 2000. **65**(1-2): p. 271-84.
19. Maeda, H., *The enhanced permeability and retention (EPR) effect in tumor vasculature: the key role of tumor-selective macromolecular drug targeting*. Adv Enzyme Regul, 2001. **41**: p. 189-207.
20. Peer, D., et al., *Nanocarriers as an emerging platform for cancer therapy*. Nat Nanotechnol, 2007. **2**(12): p. 751-60.

21. Davis, M.E., Z.G. Chen, and D.M. Shin, *Nanoparticle therapeutics: an emerging treatment modality for cancer*. Nat Rev Drug Discov, 2008. **7**(9): p. 771-82.
22. Jain, S., et al., *A two-stage strategy for sterilization of poly(lactide-co-glycolide) particles by gamma-irradiation does not impair their potency for vaccine delivery*. Journal of pharmaceutical sciences, 2011. **100**(2): p. 646-54.
23. Jain, R.A., *The manufacturing techniques of various drug loaded biodegradable poly(lactide-co-glycolide) (PLGA) devices*. Biomaterials, 2000. **21**(23): p. 2475-90.
24. Makadia, H.K. and S.J. Siegel, *Poly Lactic-co-Glycolic Acid (PLGA) as Biodegradable Controlled Drug Delivery Carrier*. Polymers, 2011. **3**(3): p. 1377-1397.
25. Brittain, H.A., Dickason, D.A., Hotz, J., Lyons, S.L., Ramstack, M.J., Wright, S.G., *Polymorphic forms of naltrexone*. International Publication WO, 2004. **2004**(108084).
26. Dean, R.L., *The preclinical development of Medisorb Naltrexone, a once a month long acting injection, for the treatment of alcohol dependence*. Frontiers in bioscience : a journal and virtual library, 2005. **10**: p. 643-55.
27. Pagani, M.D., et al., *Efficacy of a new long-acting injectable form of bromocriptine in hyperprolactinaemic patients*. Clinical endocrinology, 1992. **36**(4): p. 369-74.
28. Gianola, D., et al., *A new oral slow release form of bromocriptine, Parlodel SRO, in the chronic treatment of 26 hyperprolactinemic patients*. Gynecological endocrinology : the official journal of the International Society of Gynecological Endocrinology, 1991. **5**(3): p. 213-6.
29. Mesens, J., Rickey, M.E., Atkins, T.J., *Microencapsulated 3-Piperidinyl-substituted 1,2-benzisooxazoles and 1,2-benzisothiazoles*. US Patent 6,544,559, 2003.
30. Lawter, J.R., Lanzilotti, M.G., *Phase separation-microencapsulated pharmaceuticals compositions useful for alleviating dental disease*. US Patent 5,500,228, 1996.
31. Lill, N., Sandow, J., *Langwirkende bioabbaubare Mikropartikel und ein Verfahren zur Herstellung*. European Patent EP 505 966, 1995.
32. Pellet, M., Roume, C, *Sustained-released composition and method for preparing the same*. US Patent 6,217,893, 2001.
33. Minkov, N.K., et al., *A phase II trial with new triptorelin sustained release formulations in prostatic carcinoma*. International urology and nephrology, 2001. **33**(2): p. 379-83.
34. Orsolini, P., *Method for preparing a pharmaceutical composition in the form of microparticles*. US Patent 5,134,122, 1992.
35. Klippel, K.F., et al., *[Effectiveness and tolerance of 1 dosage forms (subcutaneous and intramuscular) of decapeptyl depot in patients with advanced prostate carcinoma]*. Der Urologe. Aug. A, 1999. **38**(3): p. 270-5.
36. Nerlich, B., Mank, R., Gustafsson, J., Horig, J., Kochling, W., *Mikroverkapselung wasserloslicher Wirkstoffe*. European Patent EP 579,347, 1996.
37. Mank, R., Gustafsson, J., Horig, J., Kochling, W., Nerlich, B, *Microencapsulation of water-soluble medicaments*. US Patent 5,503,851, 1996.
38. Ogawa, Y., et al., *In vivo release profiles of leuprolide acetate from microcapsules prepared with polylactic acids or copoly(lactic/glycolic) acids and in vivo degradation of these polymers*. Chemical & pharmaceutical bulletin, 1988. **36**(7): p. 2576-81.
39. Okada, H., Ogawa, Y., Yashiki, T., *Prolonged release microcapsule and its production*. US Patent 4,652,441, 1987.
40. Bodmer, D., Fong, J.W., Kissel, T., Maulding, H.V., Negele, O., Pearson, J.E., *Octreotidepamoat und dessen Verwendung zur Herstellung von pharmazeutischen Formulierungen*. Swiss Patent CH 686 252, 1996.

41. Tracy, M.A., *Development and scale-up of a microsphere protein delivery system*. Biotechnology progress, 1998. **14**(1): p. 108-15.
42. Johnson, O.L., et al., *A month-long effect from a single injection of microencapsulated human growth hormone*. Nature medicine, 1996. **2**(7): p. 795-9.
43. Vorp, D.A., T. Maul, and A. Nieponice, *Molecular aspects of vascular tissue engineering*. Frontiers in bioscience : a journal and virtual library, 2005. **10**: p. 768-89.
44. Hollister, S.J., *Porous scaffold design for tissue engineering*. Nature materials, 2005. **4**(7): p. 518-24.
45. Goulet, R.W., et al., *The relationship between the structural and orthogonal compressive properties of trabecular bone*. Journal of biomechanics, 1994. **27**(4): p. 375-89.
46. Sherwood, J.K., et al., *A three-dimensional osteochondral composite scaffold for articular cartilage repair*. Biomaterials, 2002. **23**(24): p. 4739-51.
47. Astete, C.E. and C.M. Sabliov, *Synthesis and characterization of PLGA nanoparticles*. Journal of biomaterials science. Polymer edition, 2006. **17**(3): p. 247-89.
48. Mao, S., et al., *Effect of WOW process parameters on morphology and burst release of FITC-dextran loaded PLGA microspheres*. International journal of pharmaceutics, 2007. **334**(1-2): p. 137-48.
49. Mu, L. and S.S. Feng, *A novel controlled release formulation for the anticancer drug paclitaxel (Taxol): PLGA nanoparticles containing vitamin E TPGS*. Journal of controlled release : official journal of the Controlled Release Society, 2003. **86**(1): p. 33-48.
50. Therin, M., et al., *In vivo degradation of massive poly(alpha-hydroxy acids): validation of in vitro findings*. Biomaterials, 1992. **13**(9): p. 594-600.
51. Park, T.G., *Degradation of poly(lactic-co-glycolic acid) microspheres: effect of copolymer composition*. Biomaterials, 1995. **16**(15): p. 1123-30.
52. Fu, K., et al., *Visual evidence of acidic environment within degrading poly(lactic-co-glycolic acid) (PLGA) microspheres*. Pharmaceutical research, 2000. **17**(1): p. 100-6.
53. Crotts, G. and T.G. Park, *Protein delivery from poly(lactic-co-glycolic acid) biodegradable microspheres: release kinetics and stability issues*. Journal of microencapsulation, 1998. **15**(6): p. 699-713.
54. Lu, L., et al., *In vitro and in vivo degradation of porous poly(DL-lactic-co-glycolic acid) foams*. Biomaterials, 2000. **21**(18): p. 1837-45.
55. Lu, L., et al., *In vitro degradation of porous poly(L-lactic acid) foams*. Biomaterials, 2000. **21**(15): p. 1595-605.
56. Cai, Q., et al., *Enzymatic degradation behavior and mechanism of poly(lactide-co-glycolide) foams by trypsin*. Biomaterials, 2003. **24**(4): p. 629-38.
57. Zolnik, B.S. and D.J. Burgess, *Evaluation of in vivo-in vitro release of dexamethasone from PLGA microspheres*. Journal of controlled release : official journal of the Controlled Release Society, 2008. **127**(2): p. 137-45.
58. Ramchandani, M. and D. Robinson, *In vitro and in vivo release of ciprofloxacin from PLGA 50:50 implants*. Journal of controlled release : official journal of the Controlled Release Society, 1998. **54**(2): p. 167-75.
59. Faisant, N., J. Siepmann, and J.P. Benoit, *PLGA-based microparticles: elucidation of mechanisms and a new, simple mathematical model quantifying drug release*. European journal of pharmaceutical sciences : official journal of the European Federation for Pharmaceutical Sciences, 2002. **15**(4): p. 355-66.
60. Organ., W.H., *World health report 2005: making every mother and child count*. World Health Organ., 2005.

61. von Lode, P., *Point-of-care immunotesting: approaching the analytical performance of central laboratory methods*. *Clinical biochemistry*, 2005. **38**(7): p. 591-606.
62. Black, R.E., S.S. Morris, and J. Bryce, *Where and why are 10 million children dying every year?* *Lancet*, 2003. **361**(9376): p. 2226-34.
63. Mabey, D., et al., *Diagnostics for the developing world*. *Nature reviews. Microbiology*, 2004. **2**(3): p. 231-40.
64. Aslan, K., J.R. Lakowicz, and C.D. Geddes, *Nanogold-plasmon-resonance-based glucose sensing*. *Analytical biochemistry*, 2004. **330**(1): p. 145-155.
65. Elghanian, R., et al., *Selective colorimetric detection of polynucleotides based on the distance-dependent optical properties of gold nanoparticles*. *Science*, 1997. **277**(5329): p. 1078-1081.
66. El-Sayed, I.H., X. Huang, and M.A. El-Sayed, *Surface plasmon resonance scattering and absorption of anti-EGFR antibody conjugated gold nanoparticles in cancer diagnostics: applications in oral cancer*. *Nano letters*, 2005. **5**(5): p. 829-34.
67. Turkevitch, J., Stevenson, P.C., Hillier, J., *Nucleation and Growth Process in the Synthesis of Colloidal Gold*. *Discuss. Faraday Soc.*, 1951. **11**: p. 55-75.
68. Frens, G., *Particle size and sol stability in metal colloids*. *Colloid & Polymer Science*, 1972. **250**(7): p. 736-741.
69. Brust, M., Walker, M., Bethell, D., Schiffrin, D.J., Whyman, R.J., *Synthesis of Thiol-Derivatized Gold Nanoparticles in a Two-phase Liquid-Liquid System*. *J. Chem. Soc.*, 1994: p. 801-802.
70. Giersig, M., Mulvaney, P., *Preparation of ordered colloid monolayers by electrophoretic deposition*. *Langmuir* 1993. **9**: p. 3408-3413.
71. Templeton, A.C., M.P. Wueling, and R.W. Murray, *Monolayer protected cluster molecules*. *Accounts of Chemical Research*, 2000. **33**(1): p. 27-36.
72. Nakamura, K., T. Kawabata, and Y. Mori, *Size distribution analysis of colloidal gold by small angle X-ray scattering and light absorbance*. *Powder Technology*, 2003. **131**(2-3): p. 120-128.
73. Haiss, W., et al., *Determination of size and concentration of gold nanoparticles from UV-vis spectra*. *Analytical chemistry*, 2007. **79**(11): p. 4215-4221.
74. Jans, H., et al., *Dynamic light scattering as a powerful tool for gold nanoparticle bioconjugation and biomolecular binding studies*. *Analytical chemistry*, 2009. **81**(22): p. 9425-32.
75. Snoswell, D.R., et al., *Colloid stability of synthetic titania and the influence of surface roughness*. *Journal of colloid and interface science*, 2005. **286**(2): p. 526-35.
76. Kim, T., et al., *Control of gold nanoparticle aggregates by manipulation of interparticle interaction*. *Langmuir : the ACS journal of surfaces and colloids*, 2005. **21**(21): p. 9524-8.
77. Kim, T., et al., *Kinetics of gold nanoparticle aggregation: experiments and modeling*. *Journal of colloid and interface science*, 2008. **318**(2): p. 238-43.
78. Cosgrove, T., *Colloid Science: Principles, methods and applicaoins*. Blackwell Publishing, Oxford, UK, 2005.
79. Gast, A.P., *Interactions of sterically stabilized particles suspended in a polymer solution*. *Macromolecules*, 1986. **19**: p. 686-691.
80. Viota, J.L., et al., *Stabilization of magnetorheological suspensions by polyacrylic acid polymers*. *Journal of colloid and interface science*, 2005. **284**(2): p. 527-41.
81. Zhang, G., et al., *Influence of anchoring ligands and particle size on the colloidal stability and in vivo biodistribution of polyethylene glycol-coated gold nanoparticles in tumor-xenografted mice*. *Biomaterials*, 2009. **30**(10): p. 1928-36.
82. Kim, D., et al., *Antibiofouling polymer-coated gold nanoparticles as a contrast agent for in vivo X-ray computed tomography imaging*. *Journal of the American Chemical Society*, 2007. **129**(24): p. 7661-5.

83. Liu, Y., et al., *Synthesis, stability, and cellular internalization of gold nanoparticles containing mixed peptide-poly(ethylene glycol) monolayers*. Analytical chemistry, 2007. **79**(6): p. 2221-9.
84. Faulk, W.P. and G.M. Taylor, *An immunocolloid method for the electron microscope*. Immunochemistry, 1971. **8**(11): p. 1081-3.
85. Schubert-Ullrich, P., et al., *Commercialized rapid immunoanalytical tests for determination of allergenic food proteins: an overview*. Analytical and bioanalytical chemistry, 2009. **395**(1): p. 69-81.
86. Stone, J., *Over-the-counter OraQuick HIV test: What does this mean for you?* Molecules to Medicine, 2012.
87. Administration, U.F.a.D., *Final advisory committee briefing materials: OraQuick in-home HIV test*. 2012.
88. Horn, T., *Orasure in-home HIV test gets unanimous approval recommendation*. AIDS MED, 2012.
89. Davis, M.E., *The first targeted delivery of siRNA in humans via a self-assembling, cyclodextrin polymer-based nanoparticle: from concept to clinic*. Mol Pharm, 2009. **6**(3): p. 659-68.
90. Davis, M.E., et al., *Evidence of RNAi in humans from systemically administered siRNA via targeted nanoparticles*. Nature, 2010. **464**(7291): p. 1067-70.
91. Sankhala, K.K., Mita, A.C., Adinin, R., Wood, L., Beeram, M., Bullock, S., Yamagata, N., Matsuno, K., Fujisawa, T., Phan, A., *A phase I pharmacokinetic (PK) study of MBP-426, a novel liposome encapsulated oxaliplatin*. J. Clin. Oncol, 2009. **27**: p. 2535.
92. Matsumura, Y. and H. Maeda, *A new concept for macromolecular therapeutics in cancer chemotherapy: mechanism of tumorotropic accumulation of proteins and the antitumor agent smancs*. Cancer Res, 1986. **46**(12 Pt 1): p. 6387-92.
93. Maeda, H., et al., *Vascular permeability enhancement in solid tumor: various factors, mechanisms involved and its implications*. International immunopharmacology, 2003. **3**(3): p. 319-28.
94. Yazdi, P.T. and R.M. Murphy, *Quantitative analysis of protein synthesis inhibition by transferrin-toxin conjugates*. Cancer Res, 1994. **54**(24): p. 6387-94.
95. Sheftel, A.D., A.B. Mason, and P. Ponka, *The long history of iron in the Universe and in health and disease*. Biochimica et biophysica acta, 2012. **1820**(3): p. 161-87.
96. Halbrooks, P.J., et al., *The oxalate effect on release of iron from human serum transferrin explained*. Journal of molecular biology, 2004. **339**(1): p. 217-26.
97. Lao, B.J., et al., *Inhibition of transferrin iron release increases in vitro drug carrier efficacy*. J Control Release, 2007. **117**(3): p. 403-12.
98. Yoon, D.J., et al., *Genetically engineering transferrin to improve its in vitro ability to deliver cytotoxins*. J Control Release, 2009. **133**(3): p. 178-84.
99. Yoon, D.J., et al., *Intratumoral therapy of glioblastoma multiforme using genetically engineered transferrin for drug delivery*. Cancer research, 2010. **70**(11): p. 4520-7.
100. Lake-Bakaar, G., et al., *Metabolism of 125I-labelled trypsin in man: evidence of recirculation*. Gut, 1980. **21**(7): p. 580-6.
101. Mu, L. and S.S. Feng, *A novel controlled release formulation for the anticancer drug paclitaxel (Taxol): PLGA nanoparticles containing vitamin E TPGS*. J Control Release, 2003. **86**(1): p. 33-48.
102. Hong, S., et al., *The binding avidity of a nanoparticle-based multivalent targeted drug delivery platform*. Chemistry & biology, 2007. **14**(1): p. 107-15.
103. Soukka, T., et al., *Utilization of kinetically enhanced monovalent binding affinity by immunoassays based on multivalent nanoparticle-antibody bioconjugates*. Analytical chemistry, 2001. **73**(10): p. 2254-60.

104. Tassa, C., et al., *Binding Affinity and Kinetic Analysis of Targeted Small Molecule-Modified Nanoparticles*. Bioconjugate Chemistry, 2010. **21**(1): p. 14-19.
105. French, A.R. and D.A. Lauffenburger, *Intracellular receptor/ligand sorting based on endosomal retention components*. Biotechnology and bioengineering, 1996. **51**(3): p. 281-97.
106. Marsh, M., et al., *Three-dimensional structure of endosomes in BHK-21 cells*. Proceedings of the National Academy of Sciences of the United States of America, 1986. **83**(9): p. 2899-903.
107. Roberts, R.L., R.E. Fine, and A. Sandra, *Receptor-mediated endocytosis of transferrin at the blood-brain barrier*. Journal of cell science, 1993. **104 (Pt 2)**: p. 521-32.
108. Kilar, F. and I. Simon, *The effect of iron binding on the conformation of transferrin. A small angle x-ray scattering study*. Biophys J, 1985. **48**(5): p. 799-802.
109. Kilar, F. and S. Hjerten, *Separation of the human transferrin isoforms by carrier-free high-performance zone electrophoresis and isoelectric focusing*. J Chromatogr, 1989. **480**: p. 351-7.
110. Dautry-Varsat, A., A. Ciechanover, and H.F. Lodish, *pH and the recycling of transferrin during receptor-mediated endocytosis*. Proc Natl Acad Sci U S A, 1983. **80**(8): p. 2258-62.
111. Yoo, H.S., et al., *Biodegradable nanoparticles containing doxorubicin-PLGA conjugate for sustained release*. Pharm Res, 1999. **16**(7): p. 1114-8.
112. Yoo, H.S. and T.G. Park, *Biodegradable polymeric micelles composed of doxorubicin conjugated PLGA-PEG block copolymer*. J Control Release, 2001. **70**(1-2): p. 63-70.
113. Lin, R., L. Shi Ng, and C.H. Wang, *In vitro study of anticancer drug doxorubicin in PLGA-based microparticles*. Biomaterials, 2005. **26**(21): p. 4476-85.
114. Tewes, F., et al., *Comparative study of doxorubicin-loaded poly(lactide-co-glycolide) nanoparticles prepared by single and double emulsion methods*. Eur J Pharm Biopharm, 2007. **66**(3): p. 488-92.
115. Park, J., et al., *PEGylated PLGA nanoparticles for the improved delivery of doxorubicin*. Nanomedicine : nanotechnology, biology, and medicine, 2009. **5**(4): p. 410-8.
116. Chiu RYT, Tsuji T, Liu CT, Mason AB, Kamei DT, *Investigation of systemic drug delivery applications for a transferrin variant*, 2011 BMES Annual Meeting, Hartford, CT, October 12-15, 2011: Books of Abstracts.
117. Chiu RYT, Mayle KM, Tsuji T, Liu CT, Lamm RJ, Wang J, Mason AB, Kamei DT, *Enhancing the delivery efficacy of drug-encapsulated nanoparticles using a transferrin variant*, 243rd American Chemical Society National Meeting & Exposition, San Diego, CA, March 25-29, 2012: Books of Abstracts.
118. Chiu RYT, Tsuji T, Liu CT, Wang J, Mason AB, Kamei DT, *Engineered transferrin for the targeted delivery of drug-loaded nanoparticles*, 2012 BMES Annual Meeting, Atlanta, GA, Oct 24-27, 2012; Biomedical Engineering Society: Books of Abstracts.
119. Wu, L.C., et al., *Programmable cellular retention of nanoparticles by replacing the synergistic anion of transferrin*. ACS nano, 2013. **7**(1): p. 365-75.
120. Yazdi, P.T. and R.M. Murphy, *Quantitative analysis of protein synthesis inhibition by transferrin-toxin conjugates*. Cancer research, 1994. **54**(24): p. 6387-94.
121. Lebron, J.A., et al., *Crystal structure of the hemochromatosis protein HFE and characterization of its interaction with transferrin receptor*. Cell, 1998. **93**: p. 111-23.
122. Ciechanover, A., et al., *Kinetics of internalization and recycling of transferrin and the transferrin receptor in a human hepatoma cell line. Effect of lysosomotropic agents*. The Journal of biological chemistry, 1983. **258**(16): p. 9681-9.
123. French, A.R. and D.A. Lauffenburger, *Controlling receptor/ligand trafficking: effects of cellular and molecular properties on endosomal sorting*. Ann Biomed Eng, 1997. **25**(4): p. 690-707.

124. *Outbreak of Swine-Origin Influenza A (H1N1) Virus Infection -- Mexico, March-April 2009*. JAMA, 2009. **301**(22): p. 2321-2322.
125. *WHO Recommendations on the Use of Rapid Testing for Influenza Diagnosis*, 2005, World Health Organization.
126. Uyeki, T.M., et al., *Low sensitivity of rapid diagnostic test for influenza*. Clinical Infectious Diseases, 2009. **48**(9): p. e89-e92.
127. Posthuma-Trumpie, G.A., J. Korf, and A. van Amerongen, *Lateral flow (immuno) assay: its strengths, weaknesses, opportunities and threats. A literature survey*. Analytical and Bioanalytical Chemistry, 2009. **393**(2): p. 569-582.
128. Faix, D.J., S.S. Sherman, and S.H. Waterman, *Rapid-test sensitivity for novel swine-origin influenza A (H1N1) virus in humans*. New England Journal of Medicine, 2009. **361**(7): p. 728.
129. Cazacu, A.C., et al., *Comparison of a new lateral-flow chromatographic membrane immunoassay to viral culture for rapid detection and differentiation of influenza A and B viruses in respiratory specimens*. Journal of clinical microbiology, 2004. **42**(8): p. 3661.
130. Cazacu, A.C., et al., *Comparison of lateral-flow immunoassay and enzyme immunoassay with viral culture for rapid detection of influenza virus in nasal wash specimens from children*. Journal of Clinical Microbiology, 2003. **41**(5): p. 2132.
131. Gavin, P.J. and R.B. Thomson, *Review of Rapid Diagnostic Tests for Influenza*. Clinical and Applied Immunology Reviews, 2004. **4**(3): p. 151-172.
132. Ginocchio, C.C., et al., *Evaluation of multiple test methods for the detection of the novel 2009 influenza A (H1N1) during the New York City outbreak*. Journal of Clinical Virology, 2009. **45**(3): p. 191-195.
133. Albertsson, P.A., *Partition of Cell Particles and Macromolecules*. 3 ed1986, New York: John Wiley & Sons.
134. Quina, F.H. and W.L. Hinze, *Surfactant-Mediated Cloud Point Extractions: An Environmentally Benign Alternative Separation Approach*. Industrial & Engineering Chemistry Research, 1999. **38**(11): p. 4150 -4168.
135. Albertsson, P.A., *Separation of cells and cell organelles by partition in aqueous polymer two-phase systems*. Methods in Enzymology, 1989. **171**: p. 532-49.
136. Kamei, D.T., et al., *Separating lysozyme from bacteriophage P22 in two-phase aqueous micellar systems*. Biotechnology and Bioengineering, 2002. **80**(2): p. 233-6.
137. Liu, C.L., et al., *Separation of proteins and viruses using two-phase aqueous micellar systems*. J Chromatogr B Biomed Sci Appl, 1998. **711**(1-2): p. 127-38.
138. Ribeiro, S.C., et al., *Isolation of plasmid DNA from cell lysates by aqueous two-phase systems*. Biotechnology and Bioengineering, 2002. **78**(4): p. 376-84.
139. Mashayekhi, F., et al., *Concentration of mammalian genomic DNA using two-phase aqueous micellar systems*. Biotechnology and Bioengineering, 2009. **102**(6): p. 1613-23.
140. Champluvier, B. and M.R. Kula, *Sequential membrane-based purification of proteins, applying the concept of multidimensional liquid chromatography (MDLC)*. Bioseparation, 1992. **2**(6): p. 343-51.
141. Lindblom, H., *Rapid chromatographic method for the isolation of glucose-6-phosphate dehydrogenase from yeast enzyme concentrate*. J Chromatogr, 1983. **266**: p. 265-71.
142. Lindblom, H., et al., *Urinary protein isolation by high-performance ion-exchange chromatography*. J Chromatogr, 1983. **266**: p. 187-96.
143. Tanford, C., *The hydrophobic effect: Formation of micelles and biological membranes, p1-10*. 2 ed1978, New York: John Wiley & Sons.

144. Bordier, C., *Phase separation of integral membrane proteins in Triton X-114 solution*. Journal of Biological Chemistry, 1981. **256**(4): p. 1604-7.
145. Nikas, Y.J., et al., *Protein Partitioning in Two-Phase Aqueous Nonionic Micellar Solutions*. Macromolecules, 1992. **25**(18): p. 4797-4806.
146. Carlson, K., *Appendix: working with bacteriophages: common techniques and methodological approaches*, in *Bacteriophages: Biology and applications*, E. Kutter and A. Sulakvelidze, Editors. 2005, CRC Press Boca Raton, FL. p. 437-494.
147. Horisberger, M. and M.F. Clerc, *Labelling of colloidal gold with protein A. A quantitative study*. Histochemistry, 1985. **82**(3): p. 219-23.
148. Leuvering, J.H., et al., *Sol particle immunoassay (SPIA)*. J Immunoassay, 1980. **1**(1): p. 77-91.
149. Lazzara, M.J., D. Blankschtein, and W.M. Deen, *Effects of Multisolute Steric Interactions on Membrane Partition Coefficients*. J Colloid Interface Sci, 2000. **226**(1): p. 112-122.
150. Day, L.A., et al., *DNA packing in filamentous bacteriophages*. Annual review of biophysics and biophysical chemistry, 1988. **17**(1): p. 509-539.
151. Won, Y.Y., H.T. Davis, and F.S. Bates, *Giant wormlike rubber micelles*. Science, 1999. **283**(5404): p. 960-3.
152. Robson, R.J. and E.A. Dennis, *The Size, Shape, and Hydration of Nonionic Surfactant Micelles. Triton X-100*. The Journal of Physical Chemistry, 1977. **81**(11): p. 1075-1078.
153. Acharya, D.P. and H. Kunieda, *Formation of Viscoelastic Wormlike Micellar Solutions in Mixed Nonionic Surfactant Systems*. J Phys Chem B, 2003. **107**(37): p. 10168-10175.
154. Paradies, H.H., *Shape and Size of a Nonionic Surfactant Micelle. Triton X-100 in Aqueous Solution*. Journal of Physical Chemistry, 1980. **84**(6): p. 599-607.
155. Dalhaimer, P., F.S. Bates, and D.E. Discher, *Single Molecule Visualization of Stable, Stiffness-Tunable, Flow-Conforming Worm Micelles*. Macromolecules, 2003. **36**(18): p. 6873 - 6877.
156. Kamei, D.T., et al., *Understanding viral partitioning in two-phase aqueous nonionic micellar systems: 2. Effect of entrained micelle-poor domains*. Biotechnology and Bioengineering, 2002. **78**(2): p. 203-16.
157. Albertsson, P.A., *Partition of cell particles and macromolecules in polymer two-phase systems*. Adv Protein Chem, 1970. **24**: p. 309-341.
158. Gavin, P.J. and R.B. Thomson Jr., *Review of rapid diagnostic tests for influenza*. Clinical and Applied Immunology Reviews, 2004. **4**(3): p. 151-172.
159. Yager, P., G.J. Domingo, and J. Gerdes, *Point-of-care diagnostics for global health*. Annual review of biomedical engineering, 2008. **10**: p. 107-44.
160. Uyeki, T.M., et al., *Low sensitivity of rapid diagnostic test for influenza*. Clinical infectious diseases : an official publication of the Infectious Diseases Society of America, 2009. **48**(9): p. e89-92.
161. World Health Organization. *WHO recommendations on the use of rapid testing for influenza diagnosis*. 2005 [cited 2013 June 18]; Available from: http://www.who.int/influenza/resources/documents/rapid_testing/en/.
162. Lim, D.V., et al., *Current and developing technologies for monitoring agents of bioterrorism and biowarfare*. Clinical microbiology reviews, 2005. **18**(4): p. 583-607.
163. van Elden, L.J., et al., *Polymerase chain reaction is more sensitive than viral culture and antigen testing for the detection of respiratory viruses in adults with hematological cancer and pneumonia*. Clinical infectious diseases, 2002. **34**(2): p. 177-183.
164. Caram, L.B., et al., *Respiratory syncytial virus outbreak in a long-term care facility detected using reverse transcriptase polymerase chain reaction: an argument for real-time detection methods*. Journal of the American Geriatrics Society, 2009. **57**(3): p. 482-5.

165. Faix, D.J., S.S. Sherman, and S.H. Waterman, *Rapid-test sensitivity for novel swine-origin influenza A (H1N1) virus in humans*. The New England journal of medicine, 2009. **361**(7): p. 728-9.
166. Ginocchio, C.C., et al., *Evaluation of multiple test methods for the detection of the novel 2009 influenza A (H1N1) during the New York City outbreak*. Journal of clinical virology : the official publication of the Pan American Society for Clinical Virology, 2009. **45**(3): p. 191-5.
167. Mashayekhi, F., et al., *Enhancing the lateral-flow immunoassay for viral detection using an aqueous two-phase micellar system*. Analytical and bioanalytical chemistry, 2010. **398**(7-8): p. 2955-61.
168. Mashayekhi, F., et al., *Enhancing the lateral-flow immunoassay for detection of proteins using an aqueous two-phase micellar system*. Analytical and bioanalytical chemistry, 2012. **404**(6-7): p. 2057-66.
169. Albertsson, P.A.k., *Partition of cell particles and macromolecules*, 1960.
170. Liu, C.-l., et al., *Separation of proteins and viruses using two-phase aqueous micellar systems*. Journal of Chromatography B: Biomedical Sciences and Applications, 1998. **711**(1): p. 127-138.
171. Azevedo, A.M., et al., *Partitioning of human antibodies in polyethylene glycol–sodium citrate aqueous two-phase systems*. Separation and Purification Technology, 2009. **65**(1): p. 14-21.
172. Köhler, K., et al., *Engineering proteins to enhance their partition coefficients in aqueous two-phase systems*. Bio/technology, 1991. **9**(7): p. 642-6.
173. Eriksson, E., P.A. Albertsson, and G. Johansson, *Hydrophobic surface properties of erythrocytes studied by affinity partition in aqueous two-phase systems*. Molecular and cellular biochemistry, 1976. **10**(2): p. 123-8.
174. He, C., et al., *Extraction of testosterone and epitestosterone in human urine using aqueous two-phase systems of ionic liquid and salt*. Journal of chromatography. A, 2005. **1082**(2): p. 143-9.
175. Johansson, H.O., et al., *Driving forces for phase separation and partitioning in aqueous two-phase systems*. Journal of chromatography. B, Biomedical sciences and applications, 1998. **711**(1-2): p. 3-17.
176. Kamei, D.T., et al., *Understanding viral partitioning in two-phase aqueous nonionic micellar systems: 1. Role of attractive interactions between viruses and micelles*. Biotechnology and Bioengineering, 2002. **78**(2): p. 190-202.
177. Quina, F.H. and W.L. Hinze, *Surfactant-mediated cloud point extractions: an environmentally benign alternative separation approach*. Industrial & Engineering Chemistry Research, 1999. **38**(11): p. 4150-4168.
178. Xin, Q., et al., *Extraction of lignins from aqueous-ionic liquid mixtures by organic solvents*. Biotechnology and bioengineering, 2012. **109**(2): p. 346-52.
179. Selber, K., et al., *Large-scale separation and production of engineered proteins, designed for facilitated recovery in detergent-based aqueous two-phase extraction systems*. Process Biochemistry, 2004. **39**(7): p. 889-896.
180. Carlson, K., *Appendix: working with bacteriophages: common techniques and methodological approaches*. Bacteriophages: biology and applications, 2005: p. 437-494.
181. Frens, G., *Particle size and sol stability in metal colloids*. Kolloid-Zeitschrift und Zeitschrift für Polymere, 1972. **250**(7): p. 736-741.
182. Fu, E., et al., *Enhanced sensitivity of lateral flow tests using a two-dimensional paper network format*. Analytical chemistry, 2011. **83**(20): p. 7941-6.
183. Asenjo, J.A. and B.A. Andrews, *Aqueous two-phase systems for protein separation: phase separation and applications*. Journal of chromatography. A, 2012. **1238**: p. 1-10.

184. Huddleston, J., et al., *The molecular basis of partitioning in aqueous two-phase systems*. Trends in biotechnology, 1991. **9**(11): p. 381-8.
185. Rosa, P.A., A.M. Azevedo, and M.R. Aires-Barros, *Application of central composite design to the optimisation of aqueous two-phase extraction of human antibodies*. Journal of Chromatography A, 2007. **1141**(1): p. 50-60.
186. Day, L.A., et al., *DNA packing in filamentous bacteriophages*. Annual review of biophysics and biophysical chemistry, 1988. **17**: p. 509-39.
187. Williams, K.A., et al., *Packing of Coat Protein Amphipathic and Transmembrane Helices in Filamentous Bacteriophage M13: Role of Small Residues in Protein Oligomerization*. Journal of molecular biology, 1995. **252**(1): p. 6-14.
188. El-Sayed, I.H., X. Huang, and M.A. El-Sayed, *Surface plasmon resonance scattering and absorption of anti-EGFR antibody conjugated gold nanoparticles in cancer diagnostics: applications in oral cancer*. Nano letters, 2005. **5**(5): p. 829-834.
189. Lee, J.-S., et al., *A DNA-gold nanoparticle-based colorimetric competition assay for the detection of cysteine*. Nano letters, 2008. **8**(2): p. 529-533.
190. Paciotti, G.F., et al., *Colloidal gold: a novel nanoparticle vector for tumor directed drug delivery*. Drug delivery, 2004. **11**(3): p. 169-183.
191. Choi, C.H.J., et al., *Mechanism of active targeting in solid tumors with transferrin-containing gold nanoparticles*. Proceedings of the National Academy of Sciences, 2010. **107**(3): p. 1235-1240.
192. Jang, H., et al., *The effective nuclear delivery of doxorubicin from dextran-coated gold nanoparticles larger than nuclear pores*. Biomaterials, 2013.
193. Hermanson, G.T., *Bioconjugate Techniques* 2008, London: Academic Press.
194. Liu, Y., et al., *Synthesis, stability, and cellular internalization of gold nanoparticles containing mixed peptide-poly (ethylene glycol) monolayers*. Analytical chemistry, 2007. **79**(6): p. 2221-2229.
195. Nath, S., et al., *Dextran-coated gold nanoparticles for the assessment of antimicrobial susceptibility*. Analytical chemistry, 2008. **80**(4): p. 1033-1038.
196. Zuk, R., et al., *Enzyme immunochemistry--a quantitative immunoassay requiring no instrumentation*. Clinical Chemistry, 1985. **31**(7): p. 1144-1150.
197. Albertsson, P.-Å., et al., *Partition of proteins in aqueous polymer two-phase systems and the effect of molecular weight of the polymer*. Biochimica Et Biophysica Acta (BBA)-General Subjects, 1987. **926**(1): p. 87-93.
198. Kamei, D.T., et al., *Separating lysozyme from bacteriophage P22 in two-phase aqueous micellar systems*. Biotechnology and bioengineering, 2002. **80**(2): p. 233-236.
199. Kamei, D.T., D.I. Wang, and D. Blankschtein, *Fundamental investigation of protein partitioning in two-phase aqueous mixed (nonionic/ionic) micellar systems*. Langmuir, 2002. **18**(8): p. 3047-3057.
200. Nikas, Y., et al., *Protein partitioning in two-phase aqueous nonionic micellar solutions*. Macromolecules, 1992. **25**(18): p. 4797-4806.
201. Mashayekhi, F., et al., *Enhancing the lateral-flow immunoassay for viral detection using an aqueous two-phase micellar system*. Analytical and Bioanalytical Chemistry, 2010. **398**(7-8): p. 2955-2961.
202. Mashayekhi, F., et al., *Enhancing the lateral-flow immunoassay for detection of proteins using an aqueous two-phase micellar system*. Analytical and bioanalytical chemistry, 2012. **404**(6-7): p. 2057-2066.
203. Wang, Y., L. Zhan, and C.Z. Huang, *One-pot preparation of dextran-capped gold nanoparticles at room temperature and colorimetric detection of dihydralazine sulfate in uric samples*. Analytical Methods, 2010. **2**(12): p. 1982-1988.

204. Jang, H., et al., *Facile synthesis of robust and biocompatible gold nanoparticles*. Chem. Commun., 2010. **46**(4): p. 583-585.
205. Huang, C.-F., et al., *Graphene oxide and dextran capped gold nanoparticles based surface plasmon resonance sensor for sensitive detection of concanavalin a*. Biosensors and Bioelectronics, 2013. **50**: p. 305-310.
206. Fu, E., et al., *Enhanced sensitivity of lateral flow tests using a two-dimensional paper network format*. Analytical chemistry, 2011. **83**(20): p. 7941-7946.
207. Warsinke, A., *Point-of-care testing of proteins*. Anal Bioanal Chem, 2009. **393**(5): p. 1393-405.
208. Zuk, R.F., et al., *Enzyme immunochromatography--a quantitative immunoassay requiring no instrumentation*. Clinical chemistry, 1985. **31**(7): p. 1144-50.
209. Peruski, A.H. and L.F. Peruski, Jr., *Immunological methods for detection and identification of infectious disease and biological warfare agents*. Clin Diagn Lab Immunol, 2003. **10**(4): p. 506-13.
210. Posthuma-Trumpie, G.A., J. Korf, and A. van Amerongen, *Lateral flow (immuno)assay: its strengths, weaknesses, opportunities and threats. A literature survey*. Anal Bioanal Chem, 2009. **393**(2): p. 569-82.
211. Mashayekhi, F., et al., *Enhancing the lateral-flow immunoassay for viral detection using an aqueous two-phase micellar system*. Analytical and Bioanalytical Chemistry, 2010. **398**(7): p. 2955-2961.
212. Mashayekhi, F., et al., *Enhancing the lateral-flow immunoassay for detection of proteins using an aqueous two-phase micellar system*. Anal Bioanal Chem, 2012. **404**(6-7): p. 2057-66.
213. World Health Organization., *World malaria report*, World Health Organization: Geneva, Switzerland. p. v.
214. Petti, C.A., et al., *Laboratory medicine in Africa: a barrier to effective health care*. Clinical infectious diseases : an official publication of the Infectious Diseases Society of America, 2006. **42**(3): p. 377-82.
215. Yager, P., et al., *Microfluidic diagnostic technologies for global public health*. Nature, 2006. **442**(7101): p. 412-8.
216. Fu, E., et al., *Two-dimensional paper network format that enables simple multistep assays for use in low-resource settings in the context of malaria antigen detection*. Analytical chemistry, 2012. **84**(10): p. 4574-9.
217. Cheng, C.M., et al., *Paper-based ELISA*. Angewandte Chemie, 2010. **49**(28): p. 4771-4.
218. Jang, H., et al., *The effective nuclear delivery of doxorubicin from dextran-coated gold nanoparticles larger than nuclear pores*. Biomaterials, 2013. **34**(13): p. 3503-10.
219. Njoki, P.N., et al., *Size correlation of optical and spectroscopic properties for gold nanoparticles*. Journal of Physical Chemistry C, 2007. **111**(40): p. 14664-14669.
220. Daniel, M.C. and D. Astruc, *Gold nanoparticles: assembly, supramolecular chemistry, quantum-size-related properties, and applications toward biology, catalysis, and nanotechnology*. Chemical reviews, 2004. **104**(1): p. 293-346.
221. Nam, J.M., C.S. Thaxton, and C.A. Mirkin, *Nanoparticle-based bio-bar codes for the ultrasensitive detection of proteins*. Science, 2003. **301**(5641): p. 1884-6.
222. Tang, D., et al., *Magnetic bead-based fluorescence immunoassay for aflatoxin B1 in food using biofunctionalized rhodamine B-doped silica nanoparticles*. The Analyst, 2010. **135**(10): p. 2661-7.
223. Pham, T.T., Cao, C., Sim, S.J., *Application of citrate-stabilized gold-coated ferric oxide composite nanoparticles for biological separations*. Journal of magnetism and magnetic materials, 2008. **320**(15): p. 2049-2055.